

REPORT NO.
UCB/EERC-91/06
MAY 1991

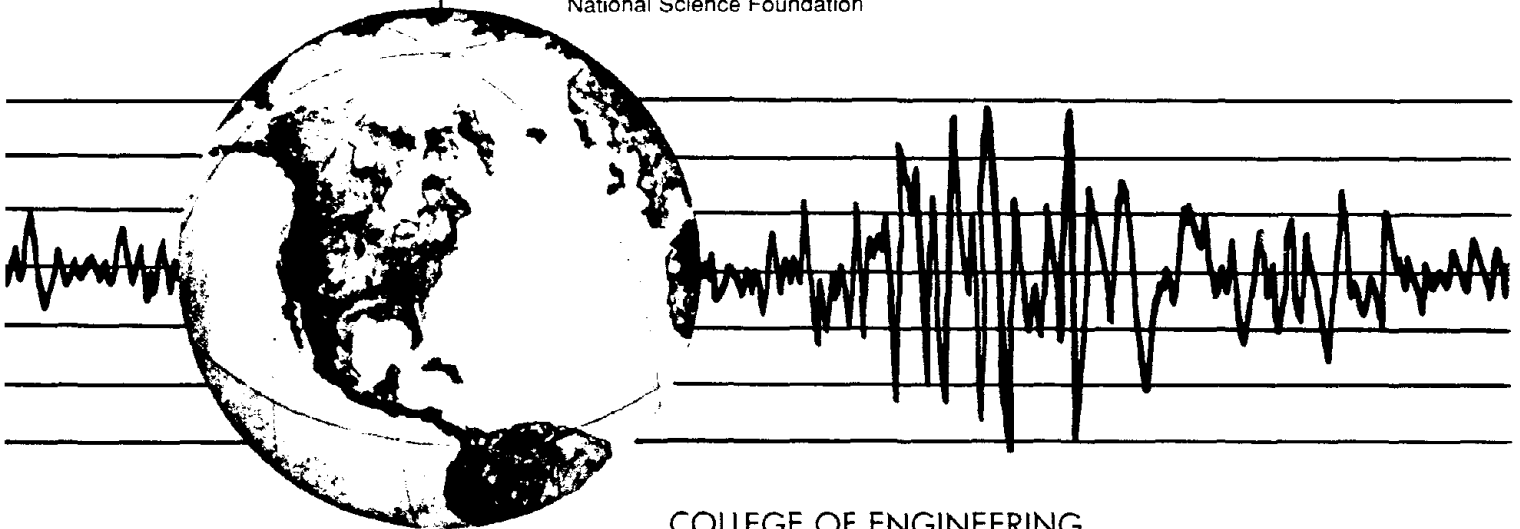
EARTHQUAKE ENGINEERING RESEARCH CENTER

**COMPUTATION OF
SPATIALLY VARYING GROUND MOTION AND
FOUNDATION-ROCK IMPEDANCE MATRICES
FOR SEISMIC ANALYSIS OF ARCH DAMS**

by

LIPING ZHANG
ANIL K. CHOPRA

A Report on Research conducted under
Grant No. CES-8719296 from the
National Science Foundation



COLLEGE OF ENGINEERING
UNIVERSITY OF CALIFORNIA AT BERKELEY

For sale by the National Technical Information Service, U.S. Department of Commerce, Springfield, Virginia 22161

See back of report for up to date listing of EERC reports.

DISCLAIMER

Any opinions, findings, and conclusions or recommendations expressed in this publication are those of the authors and do not necessarily reflect the views of the National Science Foundation or the Earthquake Engineering Research Center, University of California at Berkeley.

**COMPUTATION OF SPATIALLY VARYING GROUND MOTION
AND FOUNDATION-ROCK IMPEDANCE MATRICES
FOR SEISMIC ANALYSIS OF ARCH DAMS**

by

Liping Zhang
Anil K. Chopra

A Report on Research Conducted under
Grant CES-8719296 from
the National Science Foundation

Report No. UCB/EERC 91/06
Earthquake Engineering Research Center
University of California
Berkeley, California

May 1991



ABSTRACT

This work on the development of analytical procedures to solve two problems that are motivated by the earthquake analysis of arch dams is organized in two parts.

Presented in the first part is a direct boundary element method (BEM) to determine the three-dimensional seismic response of an infinitely-long canyon of arbitrary but uniform cross-section cut in a homogeneous viscoelastic half-space. The seismic excitation is represented by P, SV, SH or Rayleigh waves at arbitrary angles with respect to the axis of the canyon. The accuracy of the procedure and implementing computer program is demonstrated by comparison with previous solutions for the limiting case of two-dimensional response, recently obtained three-dimensional response results for infinitely-long canyons, and three-dimensional boundary element method solutions presented in this work for finite canyons. This procedure would enable analytical estimation of the spatial variation of ground motions around the canyon and hence the possibility of exploring the effects of such variation on earthquake response of arch dams.

In the second part, a direct boundary element procedure is presented to determine the foundation impedance matrix defined at the nodal points on the dam-foundation rock interface. The uniform cross-section of the infinitely-long canyon permits analytical integration along the canyon axis leading to a series of two-dimensional boundary problems involving Fourier transforms of the full-space Green's functions. Solution of these two-dimensional boundary problems leads to a dynamic flexibility influence matrix which is inverted to determine the impedance matrix. The accuracy of the procedure is demonstrated by comparison with previous solutions for a surface-supported, square foundation and results obtained by a three-dimensional BEM for a foundation of finite-width supported on an infinitely-long canyon. Compared with the three-dimensional BEM, the present method requires less computer storage and is more accurate and efficient. The foundation impedance matrix determined by this procedure can be incorporated in a substructure method for earthquake analysis of arch dams.

ACKNOWLEDGEMENTS

This research investigation was supported by the National Science Foundation under Grant CES-8719296. The authors are grateful for this support.

Parts of this work were accomplished during the 1990 Fall semester while Anil K. Chopra was on appointment as a Miller Research Professor in the Miller Institute of Basic Research in Science, University of California at Berkeley.

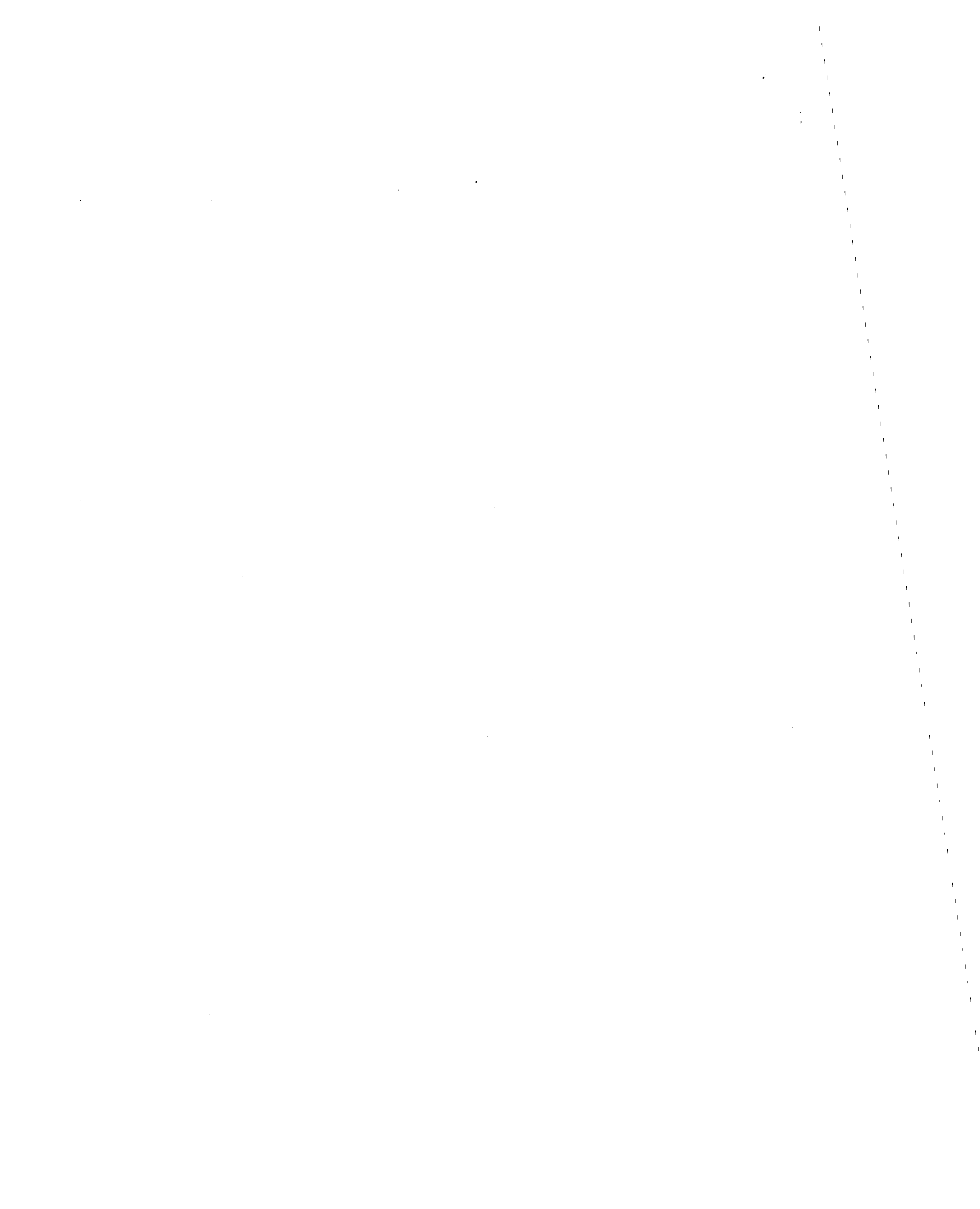
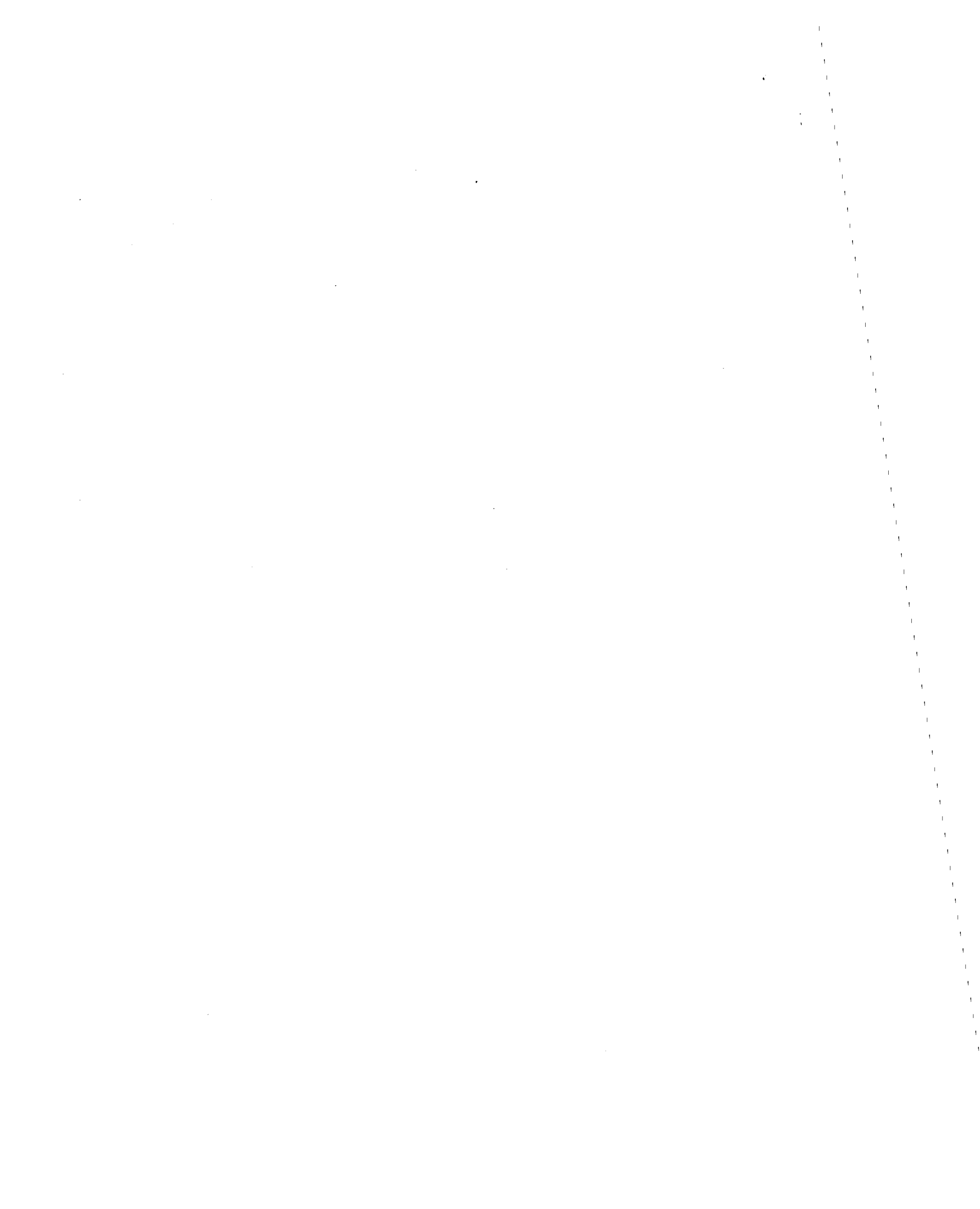


TABLE OF CONTENTS

ABSTRACT	i
ACKNOWLEDGEMENTS	ii
TABLE OF CONTENTS	iii
PART I: THREE-DIMENSIONAL ANALYSIS OF SPATIALLY VARY- ING GROUND MOTIONS AROUND A UNIFORM CANYON IN A HOMOGENEOUS HALF-SPACE	1
INTRODUCTION	3
SYSTEM CONSIDERED	6
FREE FIELD MOTION	8
BOUNDARY INTEGRAL FORMULATION	12
BOUNDARY ELEMENT FORMULATION	16
Discretization	16
Boundary Element Equations	18
Formation of System Matrices	19
Evaluation of Displacements	21
Summary	21
DISCRETIZATION ERRORS	23
VERIFICATION	33
CONCLUSIONS	41
REFERENCES	42
NOTATION	45
APPENDIX A: FREE-FIELD GROUND MOTIONS FOR SH, P, SV AND RAYLEIGH WAVES	50
APPENDIX B: FULL-SPACE GREEN'S FUNCTIONS	52
APPENDIX C: TRANSFORMED GREEN'S FUNCTIONS	53
Transformed Green's Displacement Functions	53
Transformed Green's Traction Functions	54
Expression for Matrix [C]	55



PART II: IMPEDANCE FUNCTIONS FOR THREE-DIMENSIONAL FOUNDATIONS SUPPORTED ON AN INFINITELY-LONG CANYON OF UNIFORM CROSS-SECTION IN A HOMOGENEOUS HALF-SPACE	57
INTRODUCTION	59
PROBLEM STATEMENT	60
FOURIER REPRESENTATION OF TRACTIONS AND DISPLACEMENTS	63
BOUNDARY INTEGRAL FORMULATION	65
BOUNDARY ELEMENT FORMULATION	68
Discretization	68
Boundary Element Equations	71
Formation of System Matrices	73
Evaluation of Displacements	75
IMPEDANCE MATRIX	75
SUMMARY OF PROCEDURE	78
NUMERICAL ASPECTS	80
Selection of Sampling Points in Wavenumber Domain	80
Truncation and Discretization Errors	85
VERIFICATION AND COMPUTATIONAL COSTS	96
CONCLUSIONS	103
REFERENCES	105
NOTATION	107
APPENDIX A: FOURIER TRANSFORM OF TWO-DIMENSIONAL SHAPE FUNCTIONS	112
APPENDIX B: RELATION BETWEEN $\{\bar{U}\}_k$ AND $\{\bar{U}\}_{-k}$	116
APPENDIX C: RESTRICTIONS ON MESH LAYOUT ON $\bar{\Gamma}_c$	119

PART I

**THREE-DIMENSIONAL ANALYSIS OF SPATIALLY VARY-
ING GROUND MOTIONS AROUND A UNIFORM CANYON
IN A HOMOGENEOUS HALF-SPACE**

INTRODUCTION

Spatial variations in earthquake motions around the canyon have rarely been considered in practical earthquake analyses of arch dams, primarily for paucity of recorded motions. Recent research studies have reported analyses of arch dam response to spatially varying ground motion determined from two-dimensional wave scattering analysis [1-3]. Three-dimensional analyses would obviously lead to more realistic prediction of how earthquake motions vary over the canyon. This report is therefore concerned with such analyses to determine the spatial variations in earthquake motions around canyons supporting arch dams.

The spatial variation of the ground motion resulting from the scattering and diffraction of waves by a canyon has been the subject of many studies. Most of these studies are concerned with the two-dimensional response of infinitely-long canyons of uniform cross-section. The anti-plane shear response of such geometrically two-dimensional canyons to SH waves, parallel to the longitudinal axis of the canyon, has been determined analytically for a semi-circular canyon [4], and a semi-elliptical canyon [5]; and numerically for arbitrary cross-sections [6-8]. The numerical approaches employed are based on the integral equation method [6], boundary method [7], and finite element method [8].

The plane-strain response of geometrically two-dimensional canyons to P, SV and Rayleigh waves normal to the canyon axis, which is much more complicated because of mode conversions and coupled boundary conditions, does not seem to be amenable to analytical solution. Consequently various numerical techniques have been developed. Wong used a series of Lamb's solutions as trial function to represent the scattered field and the complex amplitudes of the trial functions were determined through boundary conditions in a least square sense by a generalized inverse method [9]. Sánchez-Sesma et.al. applied Trefftz's wave function expansion method to construct the scattered field [10]. The complex coefficients of the wave functions were then determined by

enforcing boundary conditions at both the canyon and the half-plane surface in a least square sense. By expressing both the incident wave field and the scattered field in terms of wave functions, Lee and Cao solved the diffraction of P and SV waves at a two-dimensional circular canyon [11,12]. Their approach, however, results in a set of infinite number of equations which can only be solved approximately. Various boundary element methods (BEM), direct or indirect, have also been used to solve the problem. Beskos et.al. analyzed the diffraction of waves by a trench using the direct BEM with full-plane Green's functions [13]. An indirect BEM was applied by Vogt et.al. to study wave scattering by arbitrary canyons in a layered half-plane using half-space Green's function associated with distributed loads [14]. Nowak chose the direct BEM with half-plane Green's functions associated with point loads [1]. By combining the direct BEM with the discrete wavenumber Green's function, Kawase investigated the time-domain response of a semi-circular canyon in a half-plane [15]. Hirose and Kitahara developed a special BEM to study the scattering of elastic waves by inhomogeneous and anisotropic bodies in a half-space; the applicability of their method, however, is limited because of the use of the fundamental solution of elastostatics [16]. In addition to boundary methods mentioned above, various hybrid methods (e.g. Mossessian and Dravinski [17]) have been used to study diffraction of waves by surface irregularities.

Some of the numerical methods used for analysis of the plane-strain problem have also been extended to study the diffraction of waves by finite-size, three-dimensional surface irregularities including canyons and alluvial valleys. Wave function expansion methods were applied by Sánchez-Sesma et.al. [18,19], Eshraghi and Dravinski [20], and Mossessian and Dravinski [21] to analyze the diffraction of waves by various finite canyons and alluvial valleys. By expanding the incident and scattered fields in terms of spherical wave functions, Lee analyzed the scattering of elastic plane waves by a hemispherical canyon [22] and by a spherical cavity [23] in an elastic half-space. Using the direct BEM, Banerjee et.al. studied wave barriers in multi-layered soil media [24]

and Rizzo et.al. investigated the scattering of waves by cavities in full-space [25,26]. The work on wave scattering and related problems has been reviewed by Wong [27], Beskos [28] and Sánchez-Sesma [29].

Quasi two-dimensional formulations have been successful in analyzing three-dimensional responses for systems with cylindrical geometry [30-34]. Wong et. al. studied the three-dimensional dynamic response of infinitely-long pipelines by using a cylindrical eigenfunction expansion technique [30]. The ground motion due to a steady state dislocation propagating along a fault of finite-width and infinite-length were solved by Luco and Anderson for a homogeneous half-space [31] and by Mendez and Luco for a layered half-space [32] through integral representation theory. Liu et.al. investigated the three-dimensional scattering of seismic waves by a cylindrical alluvial valley embedded in a layered half-space by using a hybrid method where the boundary integral representation and FEM are combined in such a way that the problem associated with the singularity of Green's functions is eliminated [33].

The three-dimensional response of an infinitely-long, uniform canyon subjected to waves at an arbitrary angle with respect to the axis of the canyon has been analyzed recently by Luco, Wong and de Barros [34]. This problem was solved for a canyon cut in a layered viscoelastic half-space by the indirect boundary method utilizing the Green's functions associated with a concentrated load moving along the canyon axis. The number and cross-sectional location of these moving sources are determined by trial and error and their magnitudes are computed by imposing boundary conditions along the canyon surface in a least square sense.

In this report, we solve the same wave diffraction problem by a canyon, except that the half-space is homogeneous instead of layered and Rayleigh wave excitation is also considered, by the direct boundary element method in conjunction with full-space Green's function. The uniform cross-section of the infinitely-long canyon permits closed-form integration along the canyon axis leading to a "two-dimensional" boundary

element problem involving Fourier transforms of the Green's functions. The assumption of a homogeneous half-space seems to be appropriate for arch dam sites where similar rock usually extends to considerable depth.

While we were working on this problem, an early, unpublished version of a paper by Luco, Wong and de Barros [34] provided an independent set of results for evaluating the accuracy of our results. In order to facilitate comparison, we follow their notation and presentation in the next two sections and in the validation of numerical results.

SYSTEM CONSIDERED

The system considered consists of an infinitely long canyon of arbitrary but uniform cross-section cut in a homogeneous viscoelastic half-space (Figure 1). The seismic excitation is represented by P, SV, or SH waves incident on the canyon boundary with arbitrary angles with respect to the vertical axis and the horizontal axes of the canyon. Also considered are Rayleigh waves which approach the canyon horizontally at an arbitrary angle with respect to the axis of the canyon. While appropriate for exploratory purposes, free-field Rayleigh waves in a homogeneous half-space may not be realistic since they imply larger amplitudes of the vertical component of the wave than is supported by recorded data. Although the geometry of the canyon is two-dimensional in that it is uniform along its length, the earthquake motion at the canyon will vary along the axis of the canyon.

The viscoelastic half-space medium is characterized by the complex P and S wave velocities $c_p = \bar{c}_p(1 + i\eta_p)^{1/2}$ and $c_s = \bar{c}_s(1 + i\eta_s)^{1/2}$. The terms η_p and η_s represent the constant hysteretic damping factors for P and S waves respectively; and \bar{c}_p and \bar{c}_s denote the P and S wave velocities if the medium were undamped. Similarly, the Rayleigh wave velocity is given by $c_r = \bar{c}_r(1 + i\eta_r)^{1/2}$ where \bar{c}_r is the Rayleigh wave velocity without damping and η_r is the corresponding hysteretic damping factor. Both \bar{c}_r and η_r are related to $\bar{c}_p, \bar{c}_s, \eta_p$ and η_s .

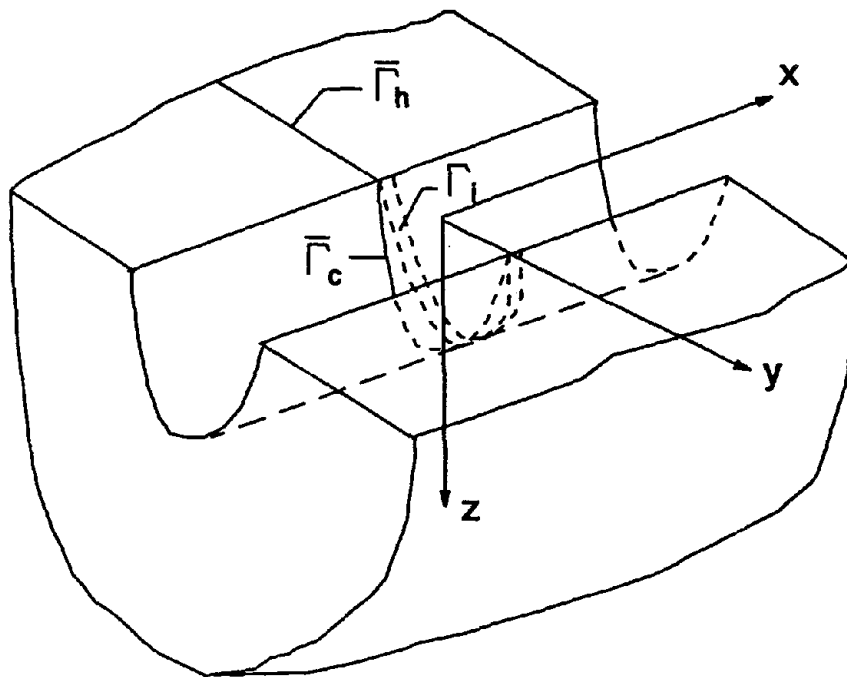


Fig.1 Infinitely-long canyon of arbitrary but uniform cross-section; $\bar{\Gamma}_c$ is the cross-section of the canyon at $x = 0$; Γ_i is the interface between the dam and foundation rock.

FREE FIELD MOTION

The first step is to determine the ground motion for free-field conditions, i.e. in the half-space without the canyon. Considered first are the body waves. The seismic excitation is represented by plane P, SV or SH waves in the underlying half-space approaching from any direction. The normal to the wave front forms an angle θ_v with the vertical axis and an angle θ_h with the axis of the canyon (Figure 2). The incident motion in the underlying half-space, at any point $\vec{x}' = (x', y', z')$, is described by the three components of displacements given by

$$\{u'(\vec{x}')\}_{inc} = A\{\bar{u}'\}e^{-ik'x' + i\nu'z' + i\omega t} \quad (1)$$

where A is the amplitude of the incident displacement, ω is the frequency of the wave, $k' = (\omega/c_p)\sin\theta_v$ and $\nu' = (\omega/c_p)\cos\theta_v$ for P-waves, and $k' = (\omega/c_s)\sin\theta_v$ and $\nu' = (\omega/c_s)\cos\theta_v$ for S-waves. In equation (1), $\{\bar{u}'\}$ is the vector

$$\{\bar{u}'\} = \begin{cases} (\sin\theta_v, 0, -\cos\theta_v)^T & \text{for P-waves} \\ (\cos\theta_v, 0, \sin\theta_v)^T & \text{for SV-waves} \\ (0, 1, 0)^T & \text{for SH-waves} \end{cases} \quad (2)$$

The incident motion associated with Rayleigh surface waves, which propagate horizontally, is given by

$$\{u'(\vec{x}')\}_{inc} = A\{\bar{u}'(z')\}e^{-ik'x' + i\omega t} \quad (3)$$

where A is a measure of the wave amplitude, $k' = (\omega/c_r)$, and $\{\bar{u}'(z')\}$ is the vector

$$\{\bar{u}'(z')\} = \left(e^{-b_L z'} - \frac{1}{2}\left(2 - \frac{c_r^2}{c_s^2}\right)e^{-b_T z'}, \quad 0, \quad ik' \left[-\frac{b_L}{k'^2} e^{-b_L z'} + \frac{1}{2b_T} \left(2 - \frac{c_r^2}{c_s^2}\right) e^{-b_T z'} \right] \right)^T \quad (4)$$

where $b_L = k'(1 - c_r^2/c_p^2)^{1/2}$ and $b_T = k'(1 - c_r^2/c_s^2)^{1/2}$.

The free-field ground motion is the total motion in the half-space resulting from the incident motion. The total motion due to surface waves is the same as the incident motion (equation 3). In the case of body waves, the total motion is the incident motion (equation 1) plus the reflected wave motion. The resulting total free-field

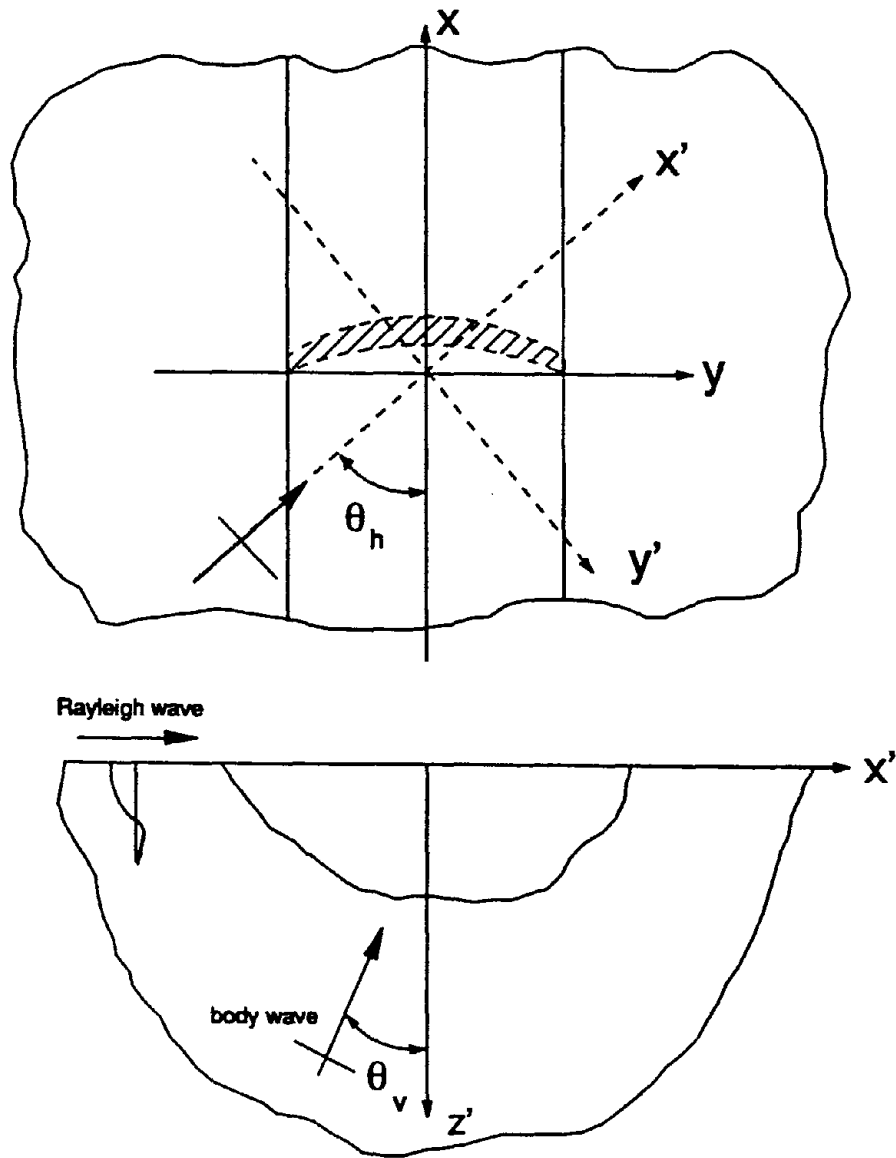


Fig.2 Canyon of uniform cross-section subjected to incident waves.

ground motion presented in Appendix A is well known for the homogeneous half-space [e.g. 35] but requires extensive calculation for a layered half-space [e.g. 36, 37]. In either case, the free-field displacement field in the $x'y'z'$ -coordinate system is denoted by

$$\{u'_{ff}(\vec{x}')\} = \{\bar{u}'_{ff}(z')\}e^{-ik'x'} \quad (5)$$

where $\{\bar{u}'_{ff}(z')\}$ are the displacement components at the plane $x' = 0$. In equation (5), and in the sequel, the factor $e^{i\omega t}$ has been deleted for brevity. Similarly the dependence of displacements and tractions on the frequency ω is implied.

The free-field displacement is next transformed to the xyz -coordinate system in which the boundary conditions at the surface of the canyon are imposed. For this purpose, the rotation of coordinates is introduced:

$$\begin{Bmatrix} x' \\ y' \\ z' \end{Bmatrix} = \begin{bmatrix} \cos\theta_h & \sin\theta_h & 0 \\ -\sin\theta_h & \cos\theta_h & 0 \\ 0 & 0 & 1 \end{bmatrix} \begin{Bmatrix} x \\ y \\ z \end{Bmatrix} = [T]^T \begin{Bmatrix} x \\ y \\ z \end{Bmatrix} \quad (6)$$

The free-field displacements at any point $\vec{x} = (x, y, z)$ are

$$\{u_{ff}(\vec{x})\} = \{\bar{u}_{ff}(\vec{x}_o)\}e^{-ikx} = [T]\{\bar{u}'_{ff}(z')\}e^{-ik'y\sin\theta_h}e^{-ikx} \quad (7)$$

where $\{\bar{u}_{ff}(\vec{x}_o)\}$ describes the displacements at $\vec{x}_o = (0, y, z)$ on the $y - z$ plane, $k = (\omega/c_p)\sin\theta_v\cos\theta_h$ for P-waves, $k = (\omega/c_s)\sin\theta_v\cos\theta_h$ for S-waves, and $k = (\omega/c_r)\cos\theta_h$ for Rayleigh waves. Equation (7) suggests that waves travelling in the x' -direction with speed \bar{c} described by equation (5), may be interpreted as propagating in the x -direction with an apparent speed of $\bar{c}/\cos\theta_h$.

In the presence of the canyon, the total displacement field $\{u(\vec{x})\}$ consists of the free-field motion $\{u_{ff}(\vec{x})\}$ and the scattered-field motion $\{u_s(\vec{x})\}$:

$$\{u(\vec{x})\} = \{u_{ff}(\vec{x})\} + \{u_s(\vec{x})\} \quad (8)$$

Similarly, the total traction vector $\{\vec{t}(\vec{x})\}$ on the canyon boundary and the half-space surface is

$$\{\vec{t}(\vec{x})\} = \{\vec{t}_{ff}(\vec{x})\} + \{\vec{t}_s(\vec{x})\} \quad (9)$$

where $\{t_{ff}^n(\vec{x})\}$ and $\{t_s^n(\vec{x})\}$ are the traction vectors associated with the free-field and scattered field respectively, and n denotes the normal to the canyon and half-space boundary at \vec{x} .

The traction vector $\{t_{ff}^n(\vec{x})\}$ can be determined from the displacement field $\{u_{ff}(\vec{x})\}$ through the strain-displacement relations and material constitutive law. It can be expressed as

$$\{t_{ff}^n(\vec{x})\} = \{t_{ff}^n(\vec{x}_o)\}e^{-ikx} \quad (10)$$

The traction free condition on the boundary Γ_c of the canyon requires that (using equation 9)

$$\{t_s^n(\vec{x})\} = -\{t_{ff}^n(\vec{x})\}, \quad \vec{x} \in \Gamma_c \quad (11)$$

On the boundary Γ_h of the half-space, the same condition leads to

$$\{t_s^n(\vec{x})\} = \{0\}, \quad \vec{x} \in \Gamma_h \quad (12)$$

because the free-field solution satisfies the traction free condition.

To determine the total displacements, $\{u(\vec{x})\}$, around the boundary of the canyon, only the scattered field in equation (8) needs to be evaluated since the free-field displacements are known from equation (7). The scattered displacement field is of the form

$$\{u_s(\vec{x})\} = \{\bar{u}_s(\vec{x}_o)\}e^{-ikx} \quad (13)$$

Thus, once the displacements along the boundary Γ_c in the plane $x = 0$ are determined, their values at the dam-foundation rock interface are known from equation (13).

Thus, the problem reduces to evaluating the displacements along the canyon boundary at the $x = 0$ plane associated with tractions at the canyon boundary and half-space surface that are known from equations (11) and (12). This problem is solved in the subsequent sections by the boundary element method, modified to recognize the uniform cross-section and infinite length of the canyon.

BOUNDARY INTEGRAL FORMULATION

The boundary integral equation can be obtained from the reciprocal theorem applied to a pair of elastodynamic equilibrium states; this theorem is a dynamic extension of the classical Betti's law for elastostatic systems. Both the selected elastodynamic equilibrium states satisfy the wave equation over the half-space with a cut canyon and radiation conditions at infinity, but not necessarily the boundary conditions. The first state is the unknown scattered displacement field $\{u_s(\vec{x})\}$ and the associated tractions $\{\overset{n}{t}_s(\vec{x})\}$ at the half-space surface and canyon boundary, which can be determined from equations (11) and (12). The second state is defined by the displacements $\{u^*(\vec{x}, \vec{x}_{os})\}$ and tractions $\{\overset{n}{t}^*(\vec{x}, \vec{x}_{os})\}$ in a full-space due to concentrated forces $\{P\} = \{P_x, P_y, P_z\}^T$ applied at a point $\vec{x}_{os} = (0, y_s, z_s)$ on $\bar{\Gamma}_c$ or $\bar{\Gamma}_h$, the intersection of the system boundary and the $x = 0$ plane. According to the reciprocal theorem, the work done by the tractions of the second state in undergoing the displacements of the first state is equal to the work done by the tractions of the first state through the displacements of the second state:

$$\int_{\Gamma_c \cup \Gamma_h \cup \Gamma_s} \int_{-\infty}^{\infty} \{\overset{n}{t}^*(\vec{x}, \vec{x}_{os})\}^T \{u_s(\vec{x})\} dx d\Gamma = \int_{\Gamma_c \cup \Gamma_h \cup \Gamma_s} \int_{-\infty}^{\infty} \{u^*(\vec{x}, \vec{x}_{os})\}^T \{\overset{n}{t}_s(\vec{x})\} dx d\Gamma \quad (14)$$

The integration is over the entire boundary S consisting of the surface of the half-space and the boundary of the canyon, modified slightly to avoid the singularity at the point of load application (Figure 3).

The displacements $\{u^*(\vec{x}, \vec{x}_{os})\}$ and tractions $\{\overset{n}{t}^*(\vec{x}, \vec{x}_{os})\}$ at a "receiver" point $\vec{x} = (x, y, z)$ on the boundary S are related to the concentrated forces applied at the "source" point $\vec{x}_{os} = (0, y_s, z_s)$ on the boundary $\bar{\Gamma}_c$ and $\bar{\Gamma}_h$:

$$\{u^*(\vec{x}, \vec{x}_{os})\} = [G^*(\vec{x}, \vec{x}_{os})]\{P\} \quad \vec{x}_{os} \in \bar{\Gamma}_c \cup \bar{\Gamma}_h, \vec{x} \in S \quad (15a)$$

$$\{\overset{n}{t}^*(\vec{x}, \vec{x}_{os})\} = [\overset{n}{F}^*(\vec{x}, \vec{x}_{os})]\{P\} \quad \vec{x}_{os} \in \bar{\Gamma}_c \cup \bar{\Gamma}_h, \vec{x} \in S \quad (15b)$$

The traction vector is associated with the normal n to the boundary, and $[G^*(\vec{x}, \vec{x}_{os})]$ and $[\overset{n}{F}^*(\vec{x}, \vec{x}_{os})]$ are 3×3 matrices of Green's functions. The first, second and third

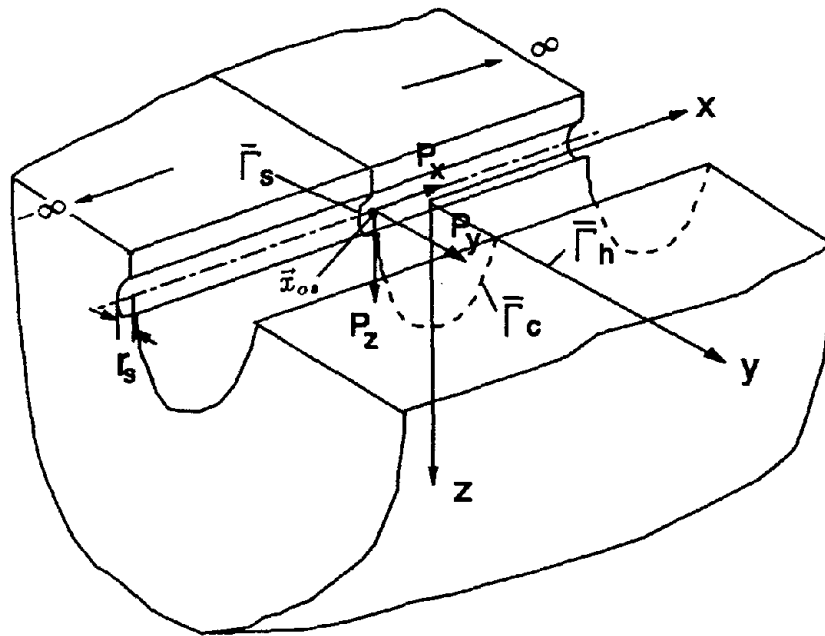


Fig.3 Definition of boundaries and source point; $\bar{\Gamma}_c$ is the cross-section of the canyon at $x=0$, $\bar{\Gamma}_h$ is the $x=0$ line on the surface of the half-space, and $\bar{\Gamma}_s$ is the small contour of radius r , around the source point.

columns of the matrices $[G^*(\vec{x}, \vec{x}_{os})]$ and $[\bar{F}^n(\vec{x}, \vec{x}_{os})]$ correspond to the displacement and traction vectors at \vec{x} for a unit point load acting at \vec{x}_{os} in the x , y and z directions, respectively. The 3×1 vector $\{P\}$ represents the unknown amplitudes of the forces. Expressions for matrices $[G^*(\vec{x}, \vec{x}_{os})]$ and $[\bar{F}^n(\vec{x}, \vec{x}_{os})]$ are presented in Appendix B [38].

The boundary integral equation is obtained by substituting equation (15) into equation (14) and recognizing that the latter should be satisfied for all force vectors $\{P\}$:

$$\begin{aligned} \int_{\bar{\Gamma}_c \cup \bar{\Gamma}_h \cup \bar{\Gamma}_s} \int_{-\infty}^{\infty} [\bar{F}^n(\vec{x}, \vec{x}_{os})]^T \{u_s(\vec{x})\} dx d\Gamma = \\ \int_{\bar{\Gamma}_c \cup \bar{\Gamma}_h \cup \bar{\Gamma}_s} \int_{-\infty}^{\infty} [G^*(\vec{x}, \vec{x}_{os})]^T \{t_s(\vec{x})\} dx d\Gamma \end{aligned} \quad (16)$$

For each source point \vec{x}_{os} , this equation represents three scalar equations in the unknown displacements $\{u_s(\vec{x})\}$.

Equation (16) can be simplified by substituting equations (10), (11) and (13) and analytically evaluating the integral along the x -axis, leading to

$$\int_{\bar{\Gamma}_c \cup \bar{\Gamma}_h \cup \bar{\Gamma}_s} ([\bar{F}^n(\vec{x}_o, \vec{x}_{os})]^T \{\bar{u}_s(\vec{x}_o)\} + [G(\vec{x}_o, \vec{x}_{os})]^T \{t_{ff}^n(\vec{x}_o)\}) d\Gamma = 0 \quad (17)$$

where

$$[G(\vec{x}_o, \vec{x}_{os})] = \int_{-\infty}^{\infty} [G^*(\vec{x}, \vec{x}_{os})] e^{-ikx} dx \quad (18a)$$

$$[\bar{F}^n(\vec{x}_o, \vec{x}_{os})] = \int_{-\infty}^{\infty} [\bar{F}^n(\vec{x}, \vec{x}_{os})] e^{-ikx} dx \quad (18b)$$

Expressions for these Fourier transforms are given in Appendix C. Thus the original boundary integral equation (16) has been transformed to a simpler form (equation 17) in which the remaining integration is only along the curve $\bar{\Gamma}_c \cup \bar{\Gamma}_h \cup \bar{\Gamma}_s$ at the $x = 0$ cross-section of the system.

The final step is to make the radius r_s of the small arc $\bar{\Gamma}_s$ around the source point, \vec{x}_{os} , approach zero. Following [39], it can be shown that

$$\lim_{r_s \rightarrow 0} \int_{\bar{\Gamma}_s} ([\bar{F}^n(\vec{x}_o, \vec{x}_{os})]^T \{\bar{u}_s(\vec{x}_o)\} + [G(\vec{x}_o, \vec{x}_{os})]^T \{t_{ff}^n(\vec{x}_o)\}) d\Gamma = [C(\vec{x}_{os})] \{\bar{u}_s(\vec{x}_{os})\} \quad (19)$$

where

$$[C(\vec{x}_{os})] = \lim_{r_s \rightarrow 0} \int_{\Gamma_s} [\vec{F}(\vec{x}_o, \vec{x}_{os})]^T d\Gamma \quad (20)$$

A general expression for the 3×3 matrix $[C(\vec{x}_{os})]$, which depends on the geometry of the boundary at the source point, is presented in Appendix C. If the boundary is smooth, i.e., it has a unique tangent, at the source point, $C_{ij}(\vec{x}_{os}) = \delta_{ij}/2$.

The final form of the boundary integral equation is obtained from equation (17) after utilizing equation (19):

$$\begin{aligned} [C(\vec{x}_{os})]\{\bar{u}_s(\vec{x}_{os})\} + \int_{\Gamma_c \cup \Gamma_h} [\vec{F}(\vec{x}_o, \vec{x}_{os})]^T \{\bar{u}_s(\vec{x}_o)\} d\Gamma \\ = - \int_{\Gamma_c \cup \Gamma_h} [G(\vec{x}_o, \vec{x}_{os})]^T \{t_{ff}(\vec{x}_o)\} d\Gamma \end{aligned} \quad (21)$$

In this equation, the traction vector $\{t_{ff}(\vec{x}_o)\}$ is known from equation (10) and the transformed Green's function matrices $[G(\vec{x}_o, \vec{x}_{os})]$ and $[\vec{F}(\vec{x}_o, \vec{x}_{os})]$ are known from equation (18) and Appendix C, whereas the scattered-field displacements at the plane $x = 0$ are the unknowns. These include $\{\bar{u}_s(\vec{x}_{os})\}$ at the source point and $\{\bar{u}_s(\vec{x}_o)\}$ at the rest of the boundary $\bar{\Gamma}_c \cup \bar{\Gamma}_h$. Once the displacements along the boundary $\bar{\Gamma}_c \cup \bar{\Gamma}_h$ are determined, the displacements at the rest of the boundary Γ , and in particular at the dam-foundation rock interface can be determined from equation (13).

By taking advantage of the uniform geometry of the system along the x -direction, the three-dimensional boundary integral equation (16) has been reduced to a "two-dimensional" problem (equation 21) involving Fourier transforms of Green's functions. This was possible because the x -variation of tractions and displacements is known analytically (equations 11 and 13) which permitted closed-form integration along the x -axis. The reduced problem is really not two-dimensional because the unknown scattered displacements along the boundary $\bar{\Gamma}_c \cup \bar{\Gamma}_h$ are three-dimensional vectors.

If the incident waves are perpendicular to the x -axis, $\theta_h = 90^\circ$ and therefore $k = 0$, equation (18) becomes

$$[G_o(\vec{x}_o, \vec{x}_{os})] = \int_{-\infty}^{\infty} [G^*(\vec{x}, \vec{x}_{os})] dx \quad (22a)$$

$$[\bar{F}_o^n(\bar{x}_o, \bar{x}_{os})] = \int_{-\infty}^{\infty} [F^n(\bar{x}, \bar{x}_{os})] dx \quad (22b)$$

In the 3×3 matrices $[G_o(\bar{x}_o, \bar{x}_{os})]$ and $[\bar{F}_o^n(\bar{x}_o, \bar{x}_{os})]$, the (1, 1) entry represents the Green's functions for the 2-D anti-plane shear motion; the (2, 2), (2, 3), (3, 2) and (3, 3) entries are the Green's functions associated with the 2-D plane-strain motion, and the remaining entries are zero because the in-plane and anti-plane motions are uncoupled. In this case, the boundary integral equation governs two uncoupled problems: the anti-plane shear problem associated with an incident SH wave and the plane-strain problem associated with incident P, SV and Rayleigh waves.

BOUNDARY ELEMENT FORMULATION

Discretization

In its present form, equation (21), which represents the exact formulation of the problem, cannot be solved analytically to determine the scattered displacements, even for the simplest canyon geometry. Therefore, the integration domain $\bar{\Gamma}_c \cup \bar{\Gamma}_h$ is discretized into M one-dimensional elements (Figure 4). Obviously, the discretization extends to only a finite distance along $\bar{\Gamma}_h$ on the half-space surface, which should be large enough to provide accurate solutions. In the simplest form, each element has two nodes, and the interpolation functions are linear. Following isoparametric element concepts, these interpolation functions are $N_1(\zeta) = 0.5(1 - \zeta)$ and $N_2(\zeta) = 0.5(1 + \zeta)$ where ζ varies from -1 to 1 (Figure 4). Thus the discretized system with M elements has $M_n = M + 1$ nodes.

The variation of the scattered-field displacements over the j th element can be expressed in terms of nodal displacements

$$\{\bar{u}_s(\zeta)\}_j = [N(\zeta)]\{\bar{U}\}_j \quad (23)$$

where $[N(\zeta)]$ is a 3×6 matrix consisting of interpolation functions

$$[N(\zeta)] = \begin{pmatrix} N_1 & 0 & 0 & N_2 & 0 & 0 \\ 0 & N_1 & 0 & 0 & N_2 & 0 \\ 0 & 0 & N_1 & 0 & 0 & N_2 \end{pmatrix} \quad (24)$$

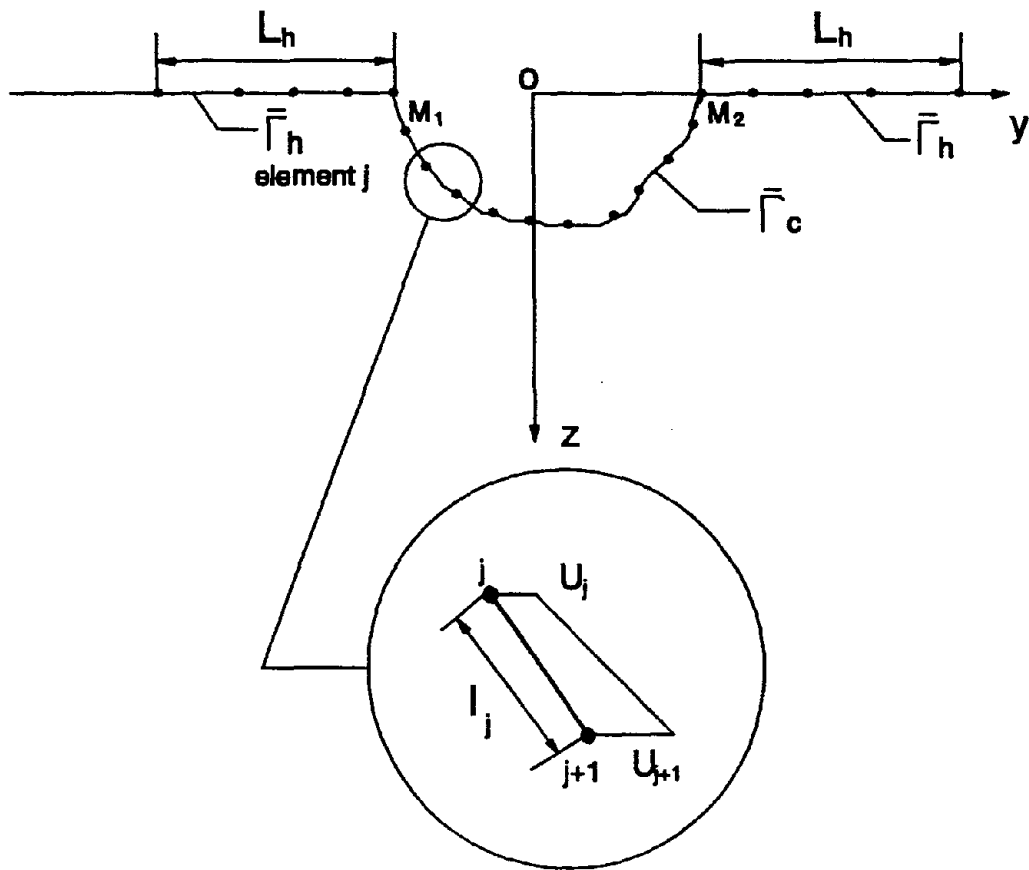


Fig.4 Boundary element discretization.

and $\{\bar{U}\}_j$ is the vector of displacements at the two nodes — j and $j+1$ — of the element

$$\{\bar{U}\}_j = \{\bar{U}_{xj}, \bar{U}_{yj}, \bar{U}_{zj}, \bar{U}_{x(j+1)}, \bar{U}_{y(j+1)}, \bar{U}_{z(j+1)}\}_j^T$$

Boundary Element Equations

The boundary integrations in equation (21) can now be expressed as summation of integrals over all the M elements

$$\begin{aligned} [C(\bar{x}_{os})]\{\bar{u}_s(\bar{x}_{os})\} + \sum_{j=1}^M \int_{\Gamma_j} [\bar{F}(\bar{x}_o, \bar{x}_{os})]_j^T \{\bar{u}_s(\bar{x}_o)\}_j d\Gamma \\ = - \sum_{j=M_1}^{M_2} \int_{\Gamma_j} [G(\bar{x}_o, \bar{x}_{os})]_j^T \{\bar{t}_{ff}(\bar{x}_o)\}_j d\Gamma \end{aligned} \quad (25)$$

where $\bar{\Gamma}_j$ represents the extent of the j th element. The summation on the right side extends over only the elements of $\bar{\Gamma}_c$, the canyon boundary (Figure 4), because the free-field tractions $\{\bar{t}_{ff}(\bar{x}_o)\}$ vanish on $\bar{\Gamma}_h$, the half-space surface, and hence the contribution of the corresponding elements is zero. By expressing the displacement field in terms of nodal displacements through equation (23), and changing the integration variable to ζ , the contributions of the j th element in equation (25) become

$$\int_{\Gamma_j} [\bar{F}(\bar{x}_o, \bar{x}_{os})]_j^T \{\bar{u}_s(\bar{x}_o)\}_j d\Gamma = \frac{1}{2} l_j \int_{-1}^1 [\bar{F}(\zeta, \bar{x}_{os})]_j^T [N(\zeta)] d\zeta \{\bar{U}\}_j \quad (26a)$$

$$\int_{\Gamma_j} [G(\bar{x}_o, \bar{x}_{os})]_j^T \{\bar{t}_{ff}(\bar{x}_o)\}_j d\Gamma = \frac{1}{2} l_j \int_{-1}^1 [G(\zeta, \bar{x}_{os})]_j^T \{\bar{t}_{ff}(\zeta)\}_j d\zeta \quad (26b)$$

where l_j is the length of the j th element. Substituting these equations, equation (25) can be expressed in matrix form:

$$[C(\bar{x}_{os})]\{\bar{u}_s(\bar{x}_{os})\} + [\bar{A}(\bar{x}_{os})]\{\bar{U}\} = \{\bar{Q}(\bar{x}_{os})\} \quad (27)$$

Equation (27) represents three equations associated with the source point $\bar{x}_{os} = (0, y_s, z_s)$, where the 3×3 matrix $[C(\bar{x}_{os})]$ is given by equation (20), the 3×1 column vector $\{\bar{u}_s(\bar{x}_{os})\}$ represents the unknown displacements at the source point, $\{\bar{U}\}$ is a

$3M_n \times 1$ column vector of unknown nodal displacements (3 displacement components at each of the M_n nodes), $[\tilde{A}(\vec{x}_{os})]$ is a $3 \times 3M_n$ matrix assembled from the integrals of the products of the transformed traction Green's functions and element interpolation functions:

$$[\tilde{A}(\vec{x}_{os})] = \frac{1}{2} \sum_{\substack{j=1 \\ \text{assemble}}}^M l_j \int_{-1}^1 [\tilde{F}(\zeta, \vec{x}_{os})]_j^T [N(\zeta)] d\zeta \quad (28)$$

and $\{\tilde{Q}(\vec{x}_{os})\}$ is a 3×1 vector defined by

$$\{\tilde{Q}(\vec{x}_{os})\} = -\frac{1}{2} \sum_{j=M_1}^{M_2} l_j \int_{-1}^1 [G(\zeta, \vec{x}_{os})]_j^T \{t_{jf}(\zeta)\}_j d\zeta \quad (29)$$

The matrix $[\tilde{A}(\vec{x}_{os})]$ is obtained by appropriately assembling the contribution of the various elements, a process that is reminiscent of the stiffness matrix assembly process in the direct stiffness method. The vector $\{\tilde{Q}(\vec{x}_{os})\}$ is obtained by direct addition of the contributions of the various elements. The construction of both of these matrices for a small system is illustrated in Figure 5.

Equation (27) is a discrete form of equation (21) obtained by introducing two approximations: (1) interpolation of displacements over each element in terms of nodal displacements (in this particular formulation the interpolation functions were chosen to be linear); and (2) truncation of the integration over $\bar{\Gamma}_h$ to a finite distance.

Formation of System Matrices

Associated with the source point $\vec{x}_{os} = (0, y_s, z_s)$, equation (27) represents 3 linear algebraic equations in $3M_n$ unknown displacements. Obviously a total of $3M_n$ equations are needed to determine the unknown displacements. These equations can be obtained by successively choosing the source point at each of the nodes of the discretized boundary. When the source point coincides with the i th node, \vec{x}_i , equation (27) becomes

$$[C(\vec{x}_i)]\{\bar{u}_s(\vec{x}_i)\} + [\tilde{A}(\vec{x}_i)]\{\bar{U}\} = \{\tilde{Q}(\vec{x}_i)\} \quad (30)$$

Such equations associated with all nodes can be obtained from equation (30) by

varying $i = 1, 2, \dots, M_n$ and assembling the resulting equations in the following form:

$$[A]\{\bar{U}\} = \{Q\} \quad (31)$$

where $[A]$ is a square matrix of order $3M_n$ given by

$$[A] = \begin{pmatrix} [C(\bar{x}_1)] & & & \\ & \cdot & & \\ & & \cdot & \\ & & & [C(\bar{x}_{M_n})] \end{pmatrix} + \begin{pmatrix} [\tilde{A}(\bar{x}_1)] \\ \cdot \\ \cdot \\ [\tilde{A}(\bar{x}_{M_n})] \end{pmatrix} \quad (32)$$

and $\{Q\}$ is a $3M_n \times 1$ column vector

$$\{Q\} = \begin{pmatrix} \{\tilde{Q}(\bar{x}_1)\} \\ \cdot \\ \cdot \\ \{\tilde{Q}(\bar{x}_{M_n})\} \end{pmatrix} \quad (33)$$

The coefficient matrix $[A]$ is unsymmetric and fully populated, which is typical of the boundary element method equations.

Evaluation of Displacements

Solution of the system of linear algebraic equations (31) leads to the nodal displacements $\{\bar{U}\}$ and thereafter the displacement variation over each finite element from equation (23). The resulting displacements represent an approximation to $\{\bar{u}_s(\bar{x}_o)\}$, the scattered displacement field along the boundary $\bar{\Gamma}_c \cup \bar{\Gamma}_h$ at the plane $x = 0$. The scattered displacements $\{u_s(\bar{x})\}$ on the boundary surface at any other plane are then given by equation (13), which when combined with the known free-field displacements (equation 7) lead to the total displacements, $\{u(\bar{x})\}$ (equation 8).

Summary

The boundary element procedure developed in the preceding sections may be summarized as follows:

1. Discretize $\bar{\Gamma}_c$, the canyon boundary at $x = 0$, and $\bar{\Gamma}_h$, the half-space surface at $x = 0$, into M line elements. If linear interpolation functions are selected for each element, the discretized system contains $M_n = M + 1$ nodes.

2. Establish equation (30) which includes three linear algebraic equations associated with the i th node, \vec{x}_i , in $3M_n$ unknowns (3 displacement components at each of the M_n nodes) by the following steps:
 - (a) Compute the elements of the 3×3 matrix $[C(\vec{x}_i)]$ which depend on the geometry of the boundary at the i th node, see Appendix C. These elements are given by $C_{jk}(\vec{x}_i) = \delta_{jk}/2$ if the boundary is smooth, i.e., it has a unique tangent at \vec{x}_i .
 - (b) Compute the $3 \times 3M_n$ matrix $[\tilde{A}(\vec{x}_i)]$ from equation (28) by assembling the contributions of all the M elements, as described in Figure 5. Element contributions are determined from the integrals of the transformed traction Green's functions (equation 18b) and element interpolation functions. Analytical expressions for the transformed traction Green's functions are available in Appendix C.
 - (c) Compute the 3×1 vector $\{\tilde{Q}(\vec{x}_i)\}$ from equation (29) by adding the contributions of the elements on the canyon boundary, as described in Figure 5. Element contributions are determined from the integrals of the products of transformed displacement Green's functions (equation 18a) and free-field tractions. Analytical expressions for the transformed Green's functions are available in Appendix C and the traction vector is determined from the free-field displacements $\{u_{ff}(\vec{x})\}$ given by equation (7) through the strain-displacement relations and material constitutive law.
3. Repeat the computations summarized in step 2 for each of the nodes, $i = 1, 2, \dots, M_n$ to determine $[C(\vec{x}_i)]$, $[\tilde{A}(\vec{x}_i)]$ and $\{\tilde{Q}(\vec{x}_i)\}$ for all the nodes.
4. Evaluate the square matrix $[A]$ of order $3M_n$ and vector $\{Q\}$ of size $3M_n$ for the boundary element system from the corresponding individual nodal matrices (step 3) using equations (32) and (33).
5. Solve the system of $3M_n$ linear algebraic equations to determine the nodal displacements $\{\tilde{U}\}$ and thereafter the displacement variations over each finite element

from equation (23).

6. Determine the scattered displacements $\{u_s(\vec{x})\}$ at the dam-foundation rock interface, or any plane other than $x = 0$, from the displacements at the $x = 0$ plane (step 5) using equation (13).
7. Add the scattered displacements $\{u_s(\vec{x})\}$ from step 6 and the free-field displacements $\{u_{ff}(\vec{x})\}$, determined from equation (7), to obtain the total displacements $\{u(\vec{x})\}$.

A computer program has been developed to implement the procedures summarized above for an incident wave of frequency ω with its propagation direction defined by angles θ_v to the vertical, z -axis and θ_h to the horizontal, x -axis of the canyon.

The boundary element formulation summarized above is for a canyon cut in a homogeneous viscoelastic half-space. In principle, this method can be extended to a layered half-space with non-horizontal layers. A boundary integral equation, similar to equation (21), can be obtained for each layer and the underlying half-space. The interfaces between layers would also require discretization because full-space Green's functions are used. Thus this approach may become computationally impractical for multi-layered systems.

DISCRETIZATION ERRORS

As mentioned earlier, discretization of the boundary obviously extends only a finite distance, L_h , along the half-space surface at the plane $x = 0$ (Figure 4). The minimum L_h necessary for accurate solution of the problem is examined next. Computed by the present procedure, with different L_h values, the displacement amplitudes around a semi-circular canyon of radius L are presented in Figures 6 to 9 for P, SH, SV and Rayleigh waves for incidence angles $\theta_h = 30^\circ$ and $\theta_v = 45^\circ$ and three values of the normalized frequency, $\Omega = \omega L / \pi \bar{c}_s$. For $L = 800$ ft, and $\bar{c}_s = 6000$ ft/sec, $\Omega = 0.5, 1$ and 2 represent frequencies $f = 1.9, 3.8$ and 7.5 Hz. The results are presented for four selections of $L_h : L, 2L, 4L$ and $6L$; in each case the element size is taken as $L/8$. The

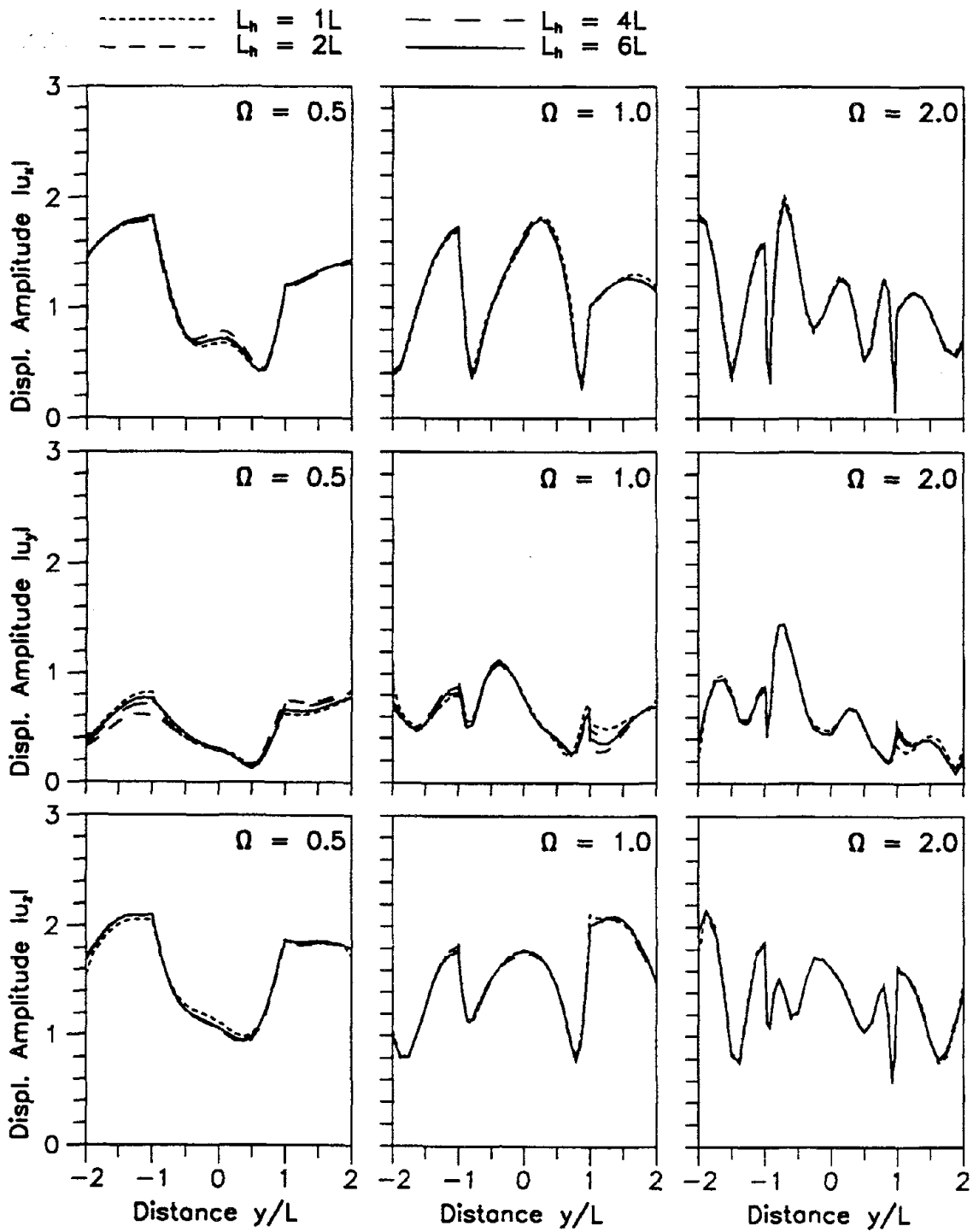


Fig.6 Influence of L_h on computed response of a semi-circular canyon to P-wave excitation ($\theta_h = 30^\circ$, $\theta_v = 45^\circ$).

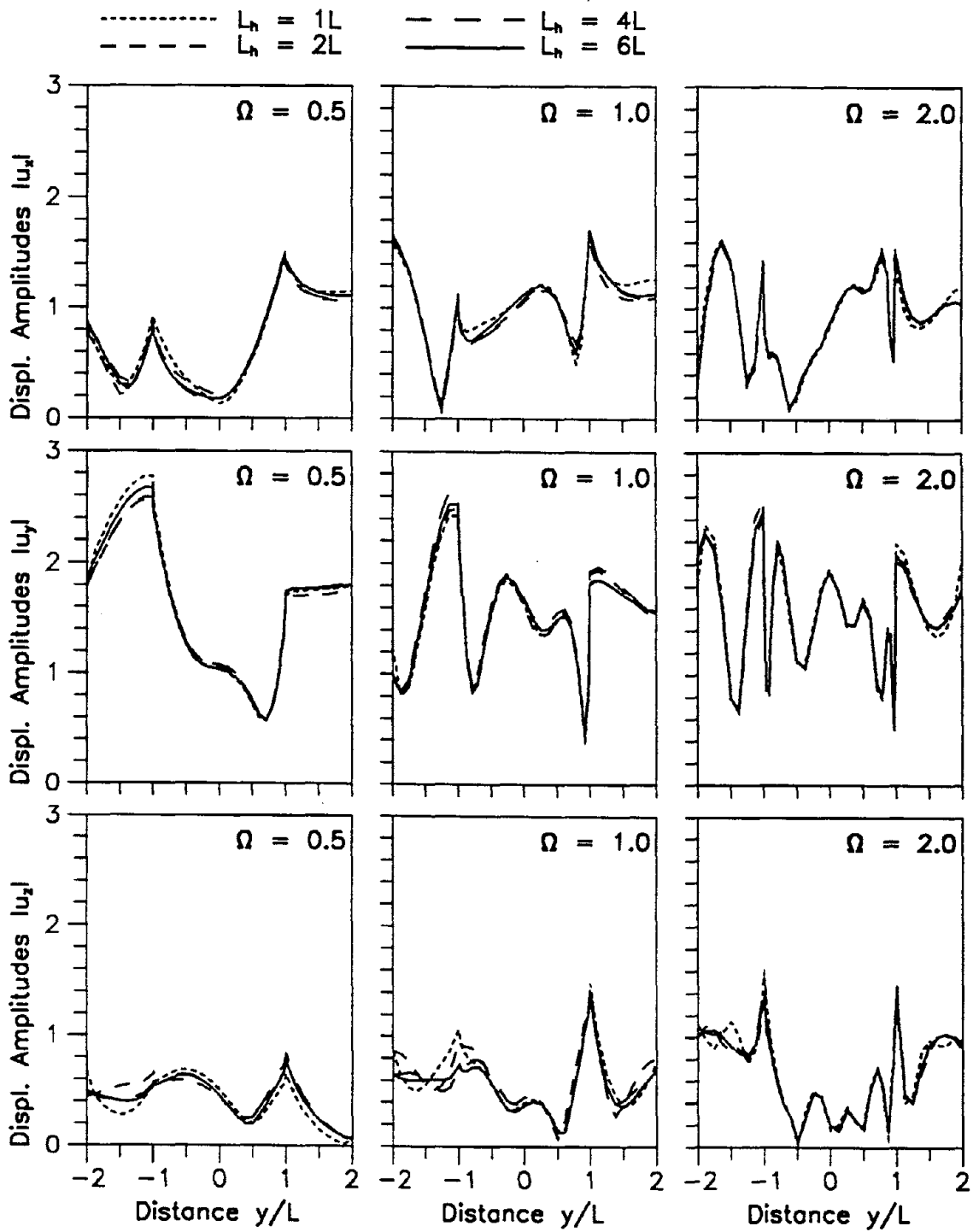


Fig.7 Influence of L_h on computed response of a semi-circular canyon to SH-wave excitation ($\theta_h = 30^\circ$, $\theta_v = 45^\circ$).

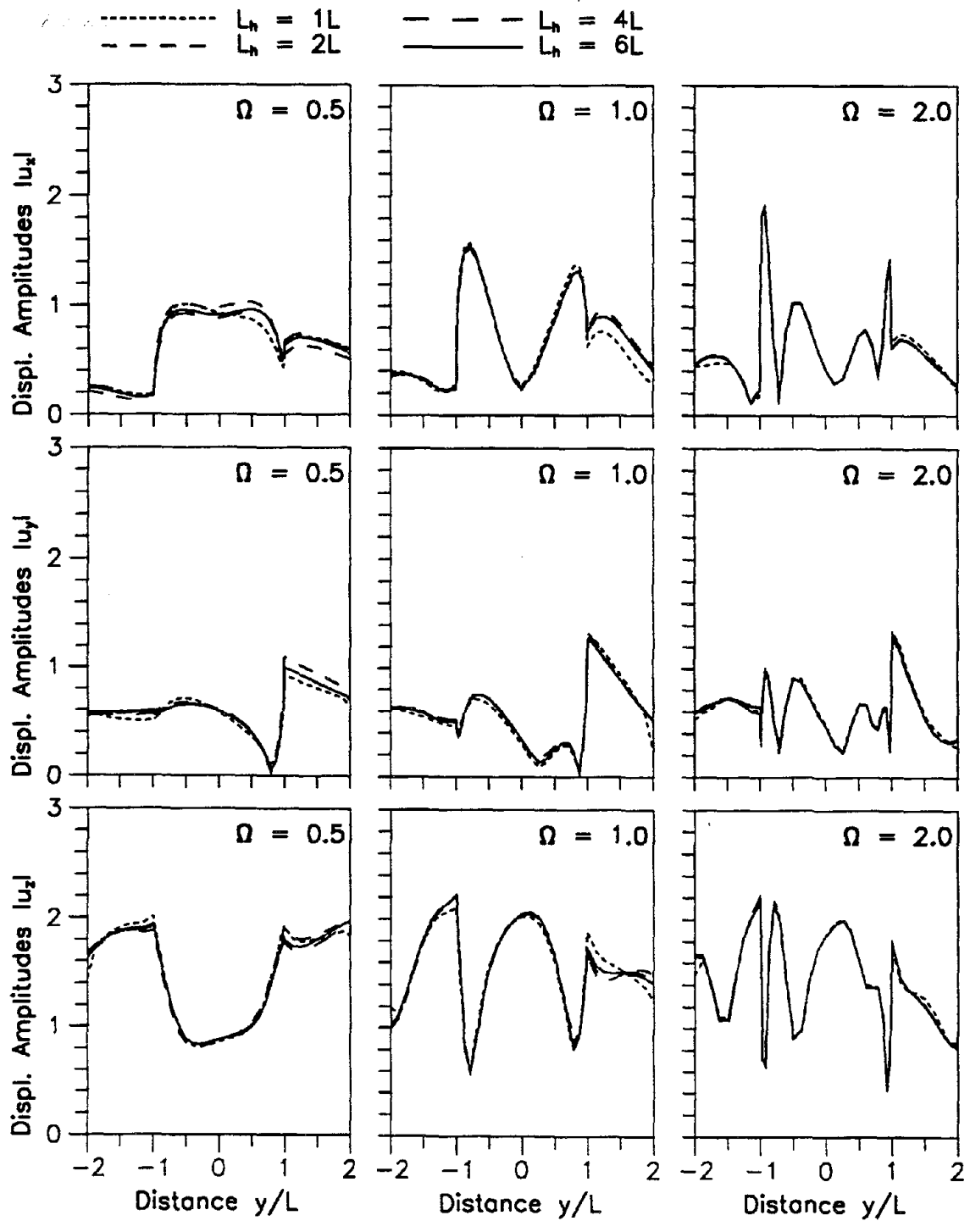


Fig.8 Influence of L_h on computed response of a semi-circular canyon to SV-wave excitation ($\theta_h = 30^\circ$, $\theta_v = 45^\circ$).

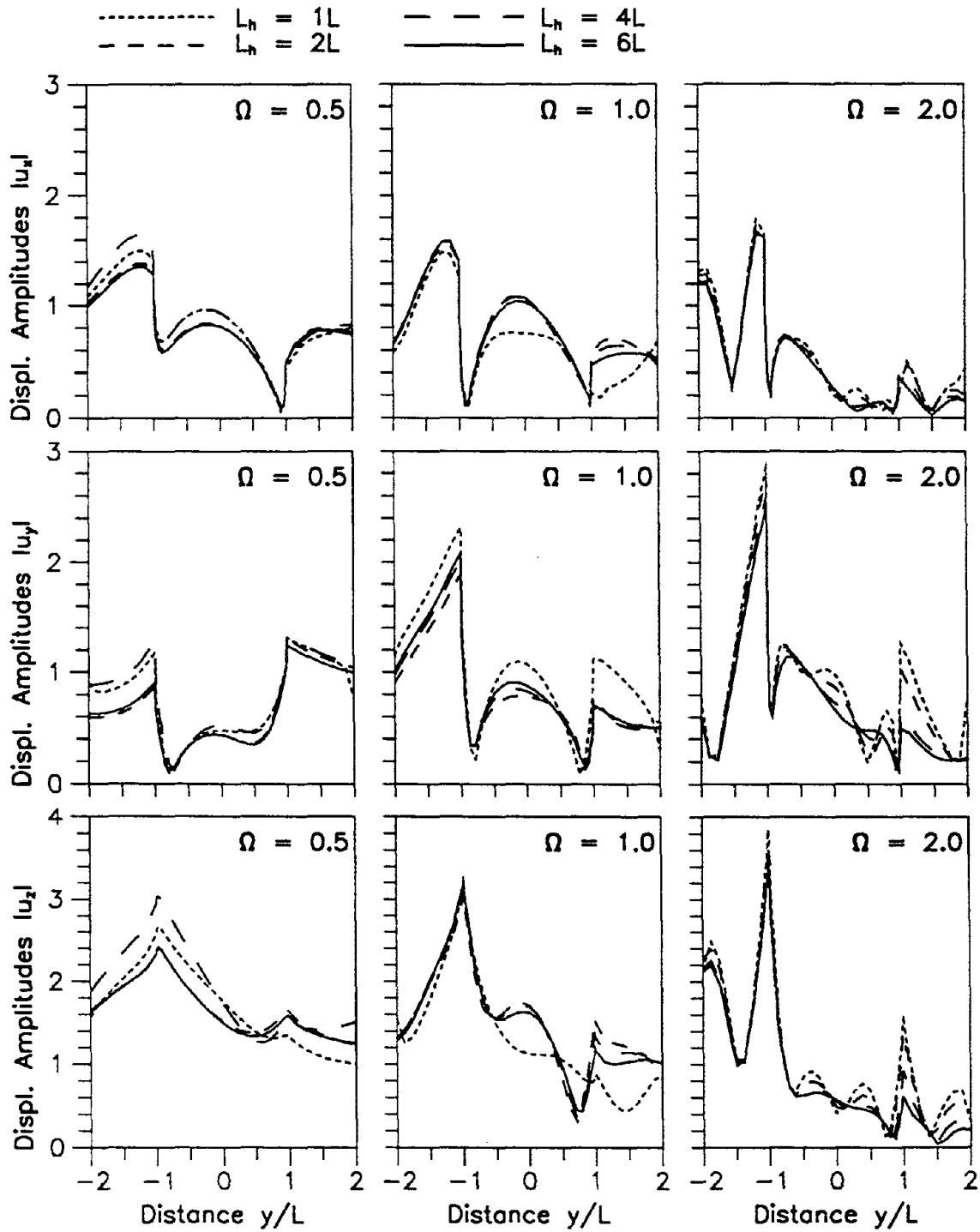


Fig.9 Influence of L_h on computed response of a semi-circular canyon to Rayleigh wave excitation ($\theta_h = 30^\circ$).

semi-circular curve $\bar{\Gamma}_c$, which is the intersection of the canyon and plane $x = 0$, is discretized into 24 elements.

It is apparent from the results of Figures 6 to 9 that, in most cases, the displacements on the canyon surface are not very sensitive to the L_h value. The dependence on L_h decreases for higher frequency. It is more meaningful to define the required L_h as a multiple of the shear wavelength. Such results demonstrate that if L_h exceeds twice the shear wavelength the results are accurate.

The dependence of the boundary element solution on the fineness of the discretization is examined next. Computed by the present procedure, the displacement amplitudes around a semi-circular canyon are presented in Figures 10 to 13 for P, SH, SV and Rayleigh waves for normalized frequency $\Omega = 0.5, 1, 2$ and $\theta_h = \theta_v = 45^\circ$. The corresponding shear wave lengths are equal to $4L$, $2L$ and L where L is the radius of the canyon. The canyon boundary is divided into N_c elements and the half-space surface into N_h elements with the latter covering an extent of $L_h = 4L$ on both sides of the canyon. The element size on $\bar{\Gamma}_h$ is about the same as that on $\bar{\Gamma}_c$. The results obtained from three different discretizations are shown in Figures 10 to 13 together with what might be considered as the "exact" result. The latter was obtained with very fine discretization, $N_c = 32$ and $N_h = 40$. It is apparent that, as the discretization becomes finer, the results converge to the "exact" values. A coarse mesh gives reasonably accurate results only at low frequency, and a finer mesh must be used at high frequency to describe the rapid variations of the displacements. It is the ratio of the shear wavelength to the element size that determines if a chosen mesh is fine enough. Reliable results are obtained when this ratio is greater than 5.

In summary, the present method is reliable and can be used to analyze the spatial variations of motion around an infinitely-long canyon of arbitrary shape. In order to control discretization errors, the element size on the canyon surface should be kept smaller than one-fifth of the shear wavelength, and the half-space surface should be

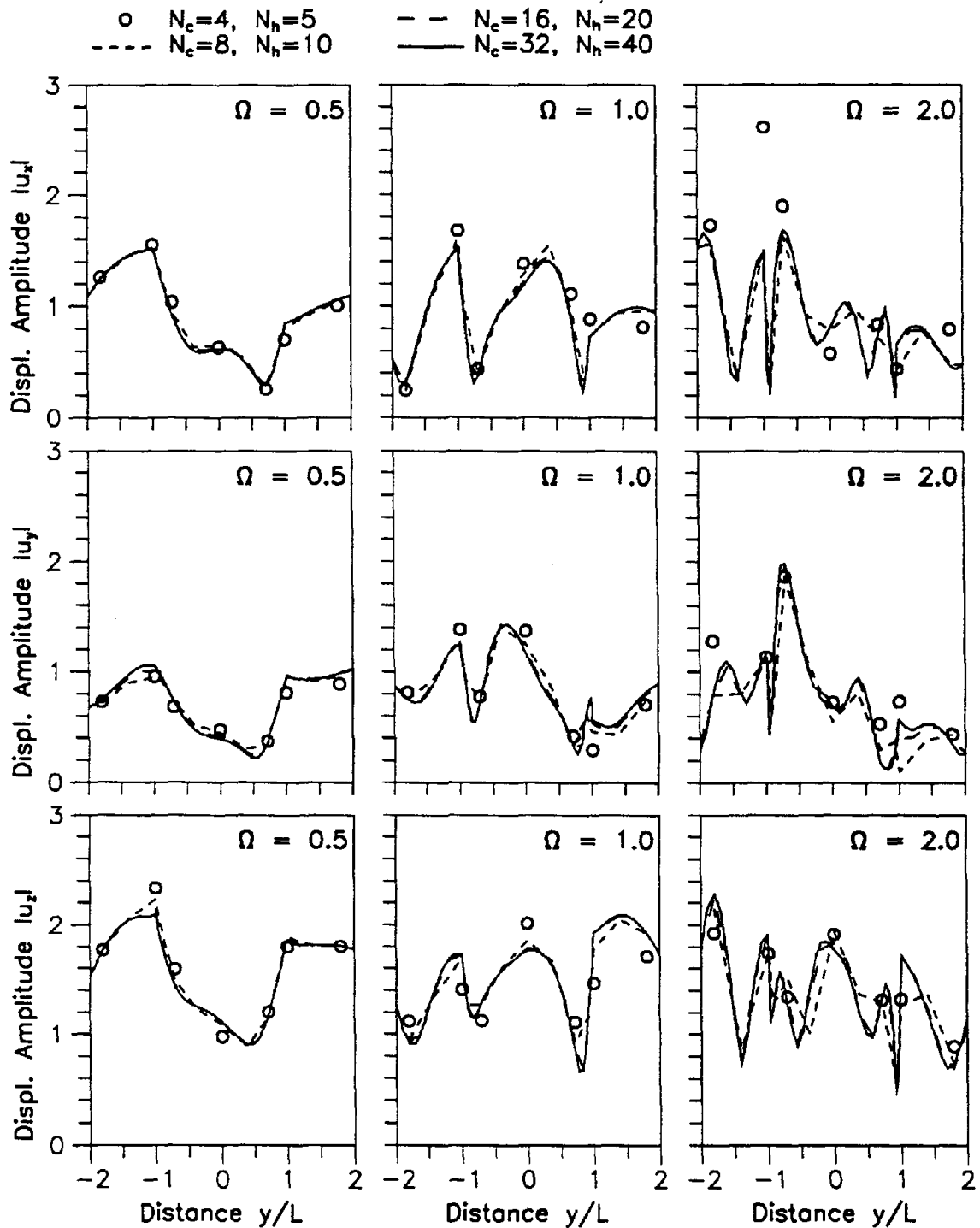


Fig.10 Influence of mesh refinement on computed response of a semi-circular canyon to P-wave excitation ($\theta_h = \theta_v = 45^\circ$, $L_h = 4L$).

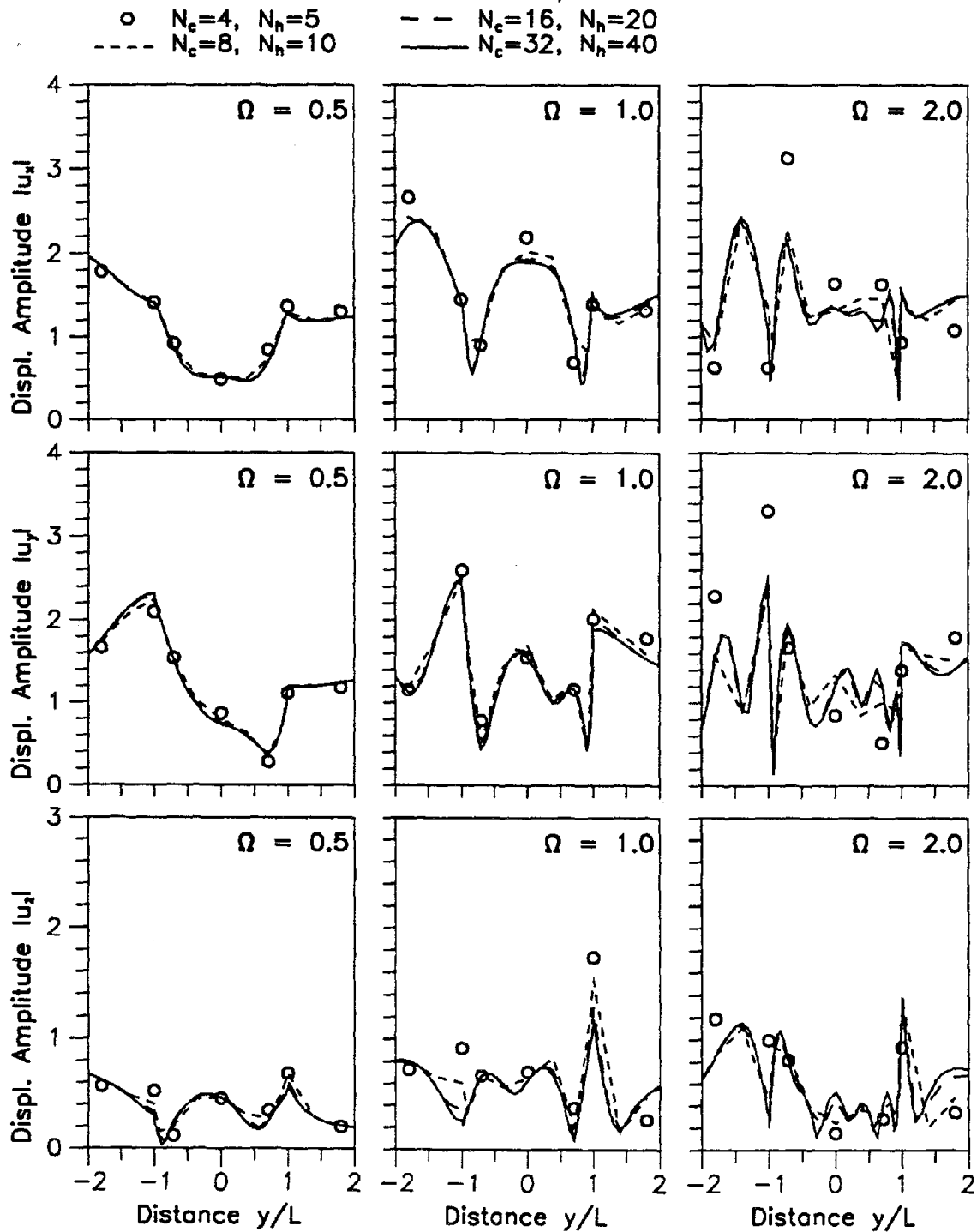


Fig.11 Influence of mesh refinement on computed response of a semi-circular canyon to SH-wave excitation ($\theta_h = \theta_v = 45^\circ$, $L_h = 4L$).

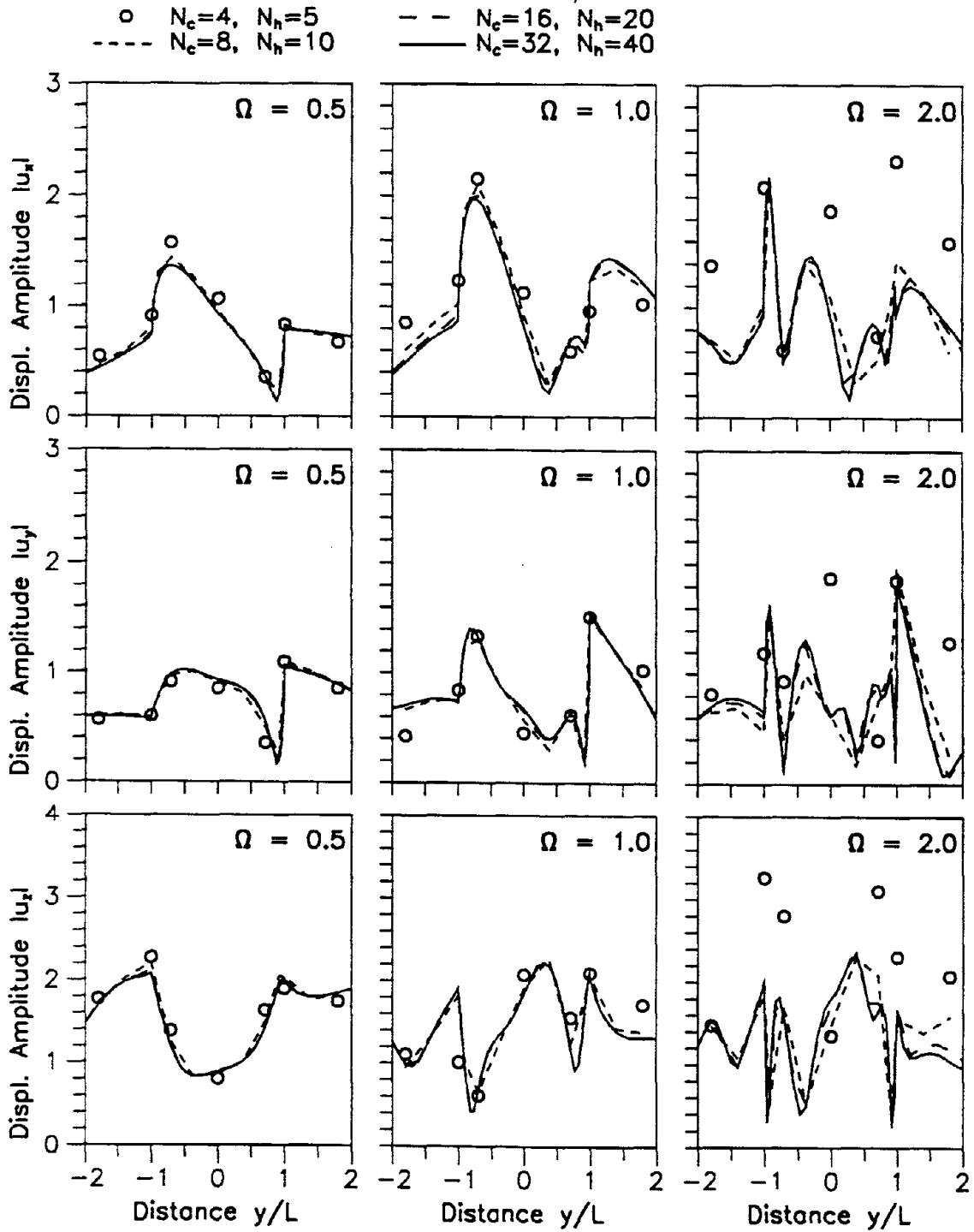


Fig.12 Influence of mesh refinement on computed response of a semi-circular canyon to SV-wave excitation ($\theta_h = \theta_v = 45^\circ$, $L_h = 4L$).

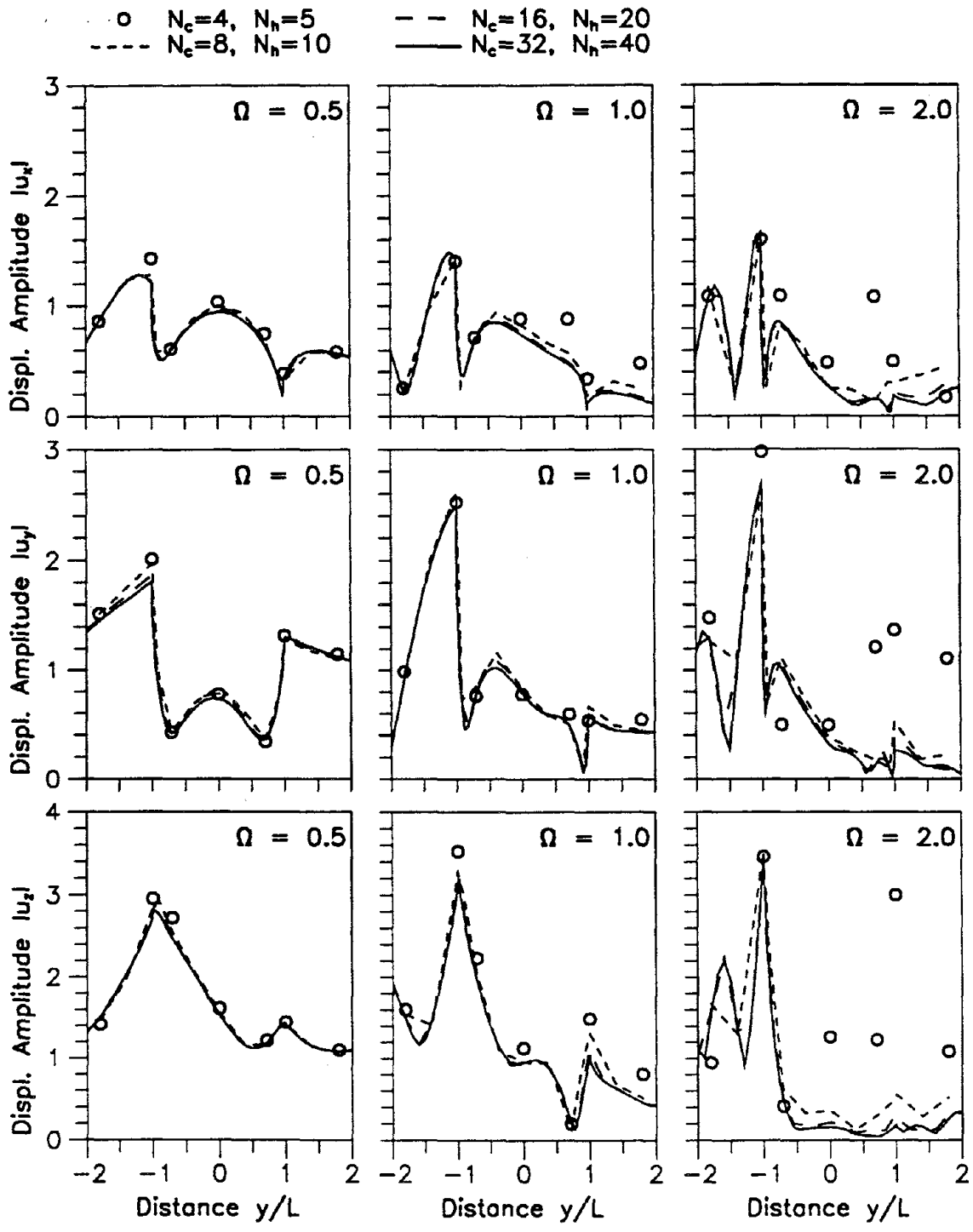


Fig.13 Influence of mesh refinement on computed response of a semi-circular canyon to Rayleigh wave excitation ($\theta_h = 45^\circ$, $L_h = 4L$).

discretized on both sides of the canyon over a distance of at least two times the shear wavelength.

VERIFICATION

The analytical procedure and the implementing computer program were tested by solving problems for which previous results are available. In all cases, an infinitely-long canyon with semi-circular cross-section of radius L cut in a homogeneous half-space is considered. The earlier results [4,9] for the two-dimensional response of the canyon are for a elastic half-space with $\bar{c}_p = 2\bar{c}_s$, i.e. Poisson's ratio = $1/3$. The recent results [34] for the three-dimensional response of the canyon are for a slightly dissipative viscoelastic half-space characterized by $\bar{c}_p = 2\bar{c}_s$ and $\eta_p = \eta_s = 0.02$. The present approach is implemented for the latter set of material properties, with the canyon boundary $\bar{\Gamma}_c$ discretized into 32 equal elements and each side of the half-space boundary $\bar{\Gamma}_p$ is discretized into 30 equal elements covering $L_h = 4L$ (Figure 4).

The results obtained by the present method for the two-dimensional anti-plane shear motion arising from an SH wave of unit amplitude impinging normal to the canyon axis are compared in Figure 14a with the exact solution of Trifunac [4]. The results presented describe the displacement amplitudes around the canyon for $\theta_v = 1^\circ, 45^\circ$ and 85° and a dimensionless frequency $\Omega = \omega L / \pi \bar{c}_s = 1$. A similar comparison is presented in Figure 14b for $\theta_v = 0^\circ$ and $\theta_h = 0^\circ$ which corresponds to a vertically incident SH wave with particle motion perpendicular to the axis of the canyon. For this plane-strain case, the numerical results are available (e.g. Wong [9]). Figure 15 shows the results for the two-dimensional response of the canyon to P and SV waves impinging normal to the axis of the canyon ($\theta_h = 90^\circ$) at various vertical angles θ_v and for a dimensionless frequency $\Omega = \omega L / \pi \bar{c}_s = 1$. The comparisons in Figures 14 and 15 indicate that the present method provides reasonably accurate results for the two-dimensional limiting cases considered.

We now turn to the three-dimensional response of a canyon to incident waves

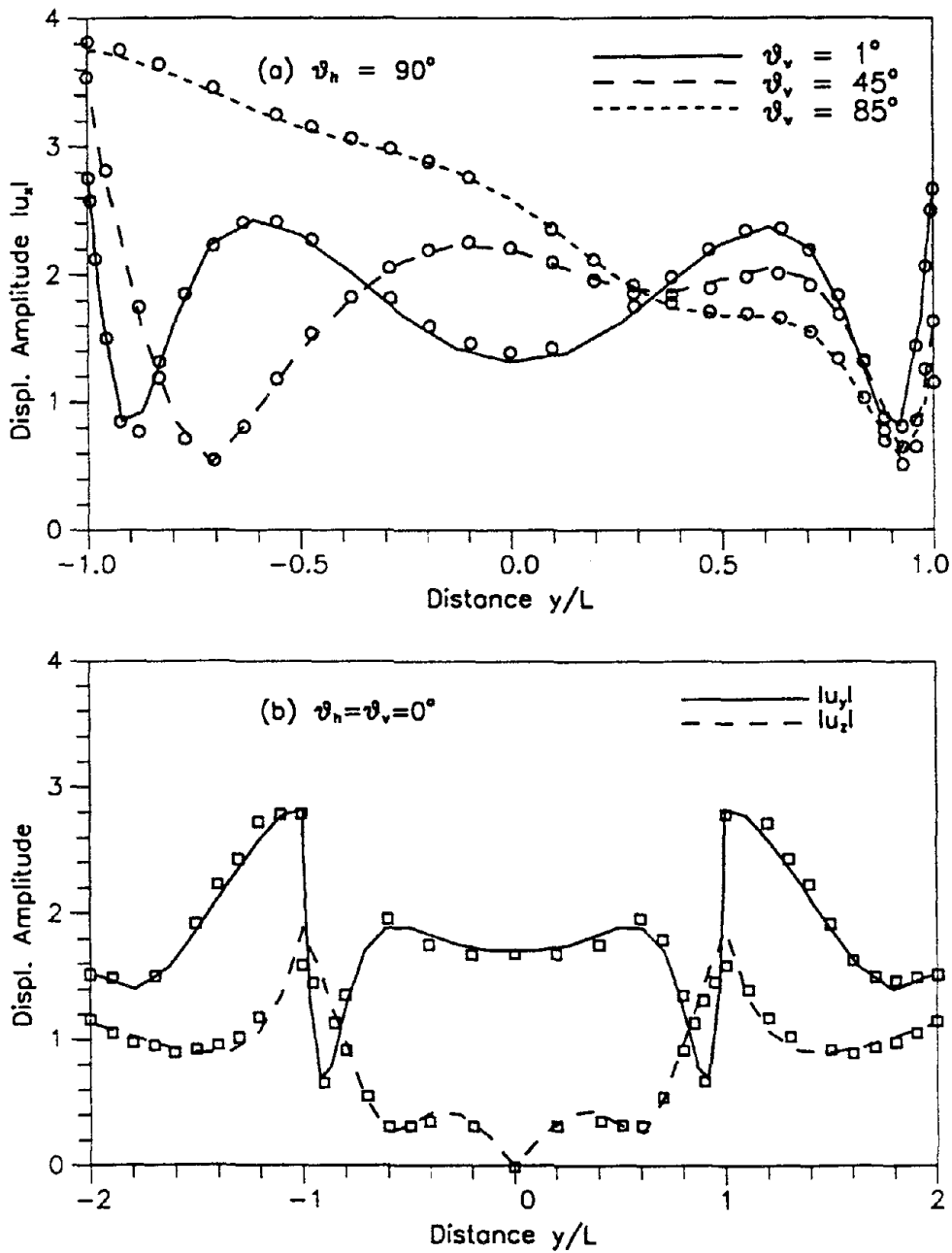


Fig.14 Comparison of results of present method (lines) with previous results (Ref.[4] shown by \circ , and Ref.[9] shown by \square) for SH-wave excitation; $\Omega = 1$.

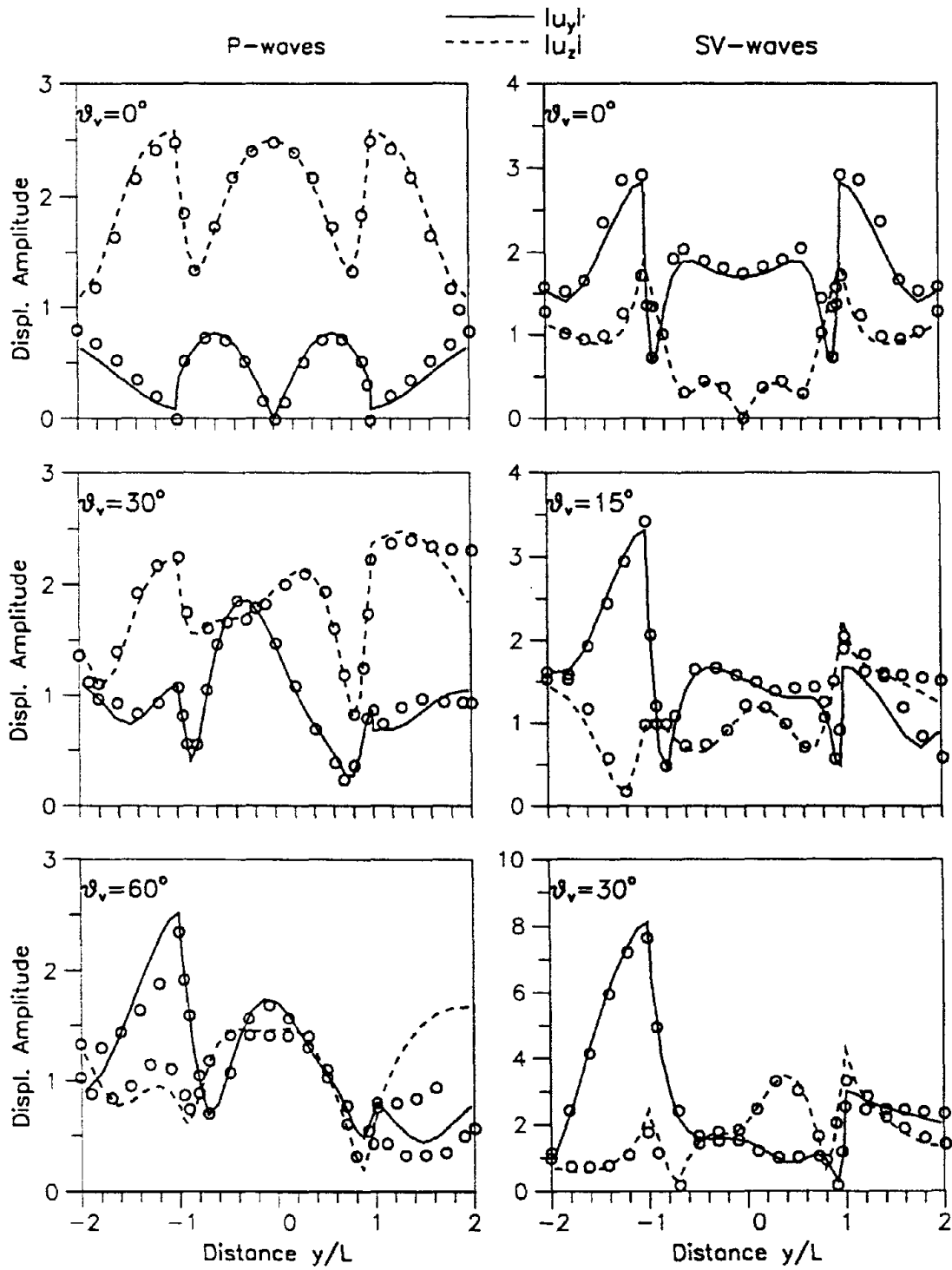


Fig.15 Comparison of results of present method (lines) with previous results (Ref.[9] shown by \circ) for P- and SV- wave excitations; $\Omega = 1, \theta_h = 90^\circ$.

impinging from an arbitrary direction. The calculated amplitudes of the three displacement components ($|u_x|$, $|u_y|$, and $|u_z|$) for incident P, SH and SV waves of unit amplitude, dimensionless frequency $\Omega = \omega L / \pi \bar{c}_s = 1$, vertical angle of incidence $\theta_v = 45^\circ$, and horizontal angle of incidence $\theta_h = 45^\circ$ are presented as solid lines in Figure 16 for an infinitely-long canyon of semi-circular cross-section, dashed lines represent the results obtained by the indirect boundary method [34]. This comparison indicates that the present method provides reasonably accurate results also for the three-dimensional problem.

Also included in Figure 16 are the displacement amplitudes around the canyon computed by analyzing a finite-length canyon by a fully three-dimensional version of the present boundary element method. In this case, discretization is necessary even along the canyon axis (Figure 17) in contrast to the method presented in the preceding sections where integrations in the x -direction could be evaluated analytically (equation 14). The results at $x = 0$ obtained for the finite-length canyon of Figure 17 with $d = 4L$ and $L_h = 1.5L$ are shown in Figure 16 by discrete symbols. The finiteness of the canyon has only a small effect on the displacements far from the ends of the canyon. The results for the finite-length canyon can be improved in accuracy at the expense of increased computational effort — by increasing L_h and by using a finer discretization on the canyon boundary.

The results presented in Figure 18 are for an infinitely-long canyon (Figure 1) and finite canyons (Figure 19) of four different lengths subjected to Rayleigh waves with dimensionless frequency $\Omega = \omega L / \pi \bar{c}_s = 1$, and horizontal angles of incidence $\theta_h = 30^\circ$ and 60° . This comparison indicates that the results obtained for infinite and finite canyons are generally similar and become closer with increasing length of the finite canyon. The accuracy of the results obtained for the finite-length canyon is limited because of the coarseness of the discretization on the canyon boundary and the short distance, $L_h = 1.5L$, over which the discretization extends on the half-space surface (Figure 19). Compared with the fully three-dimensional version of the boundary

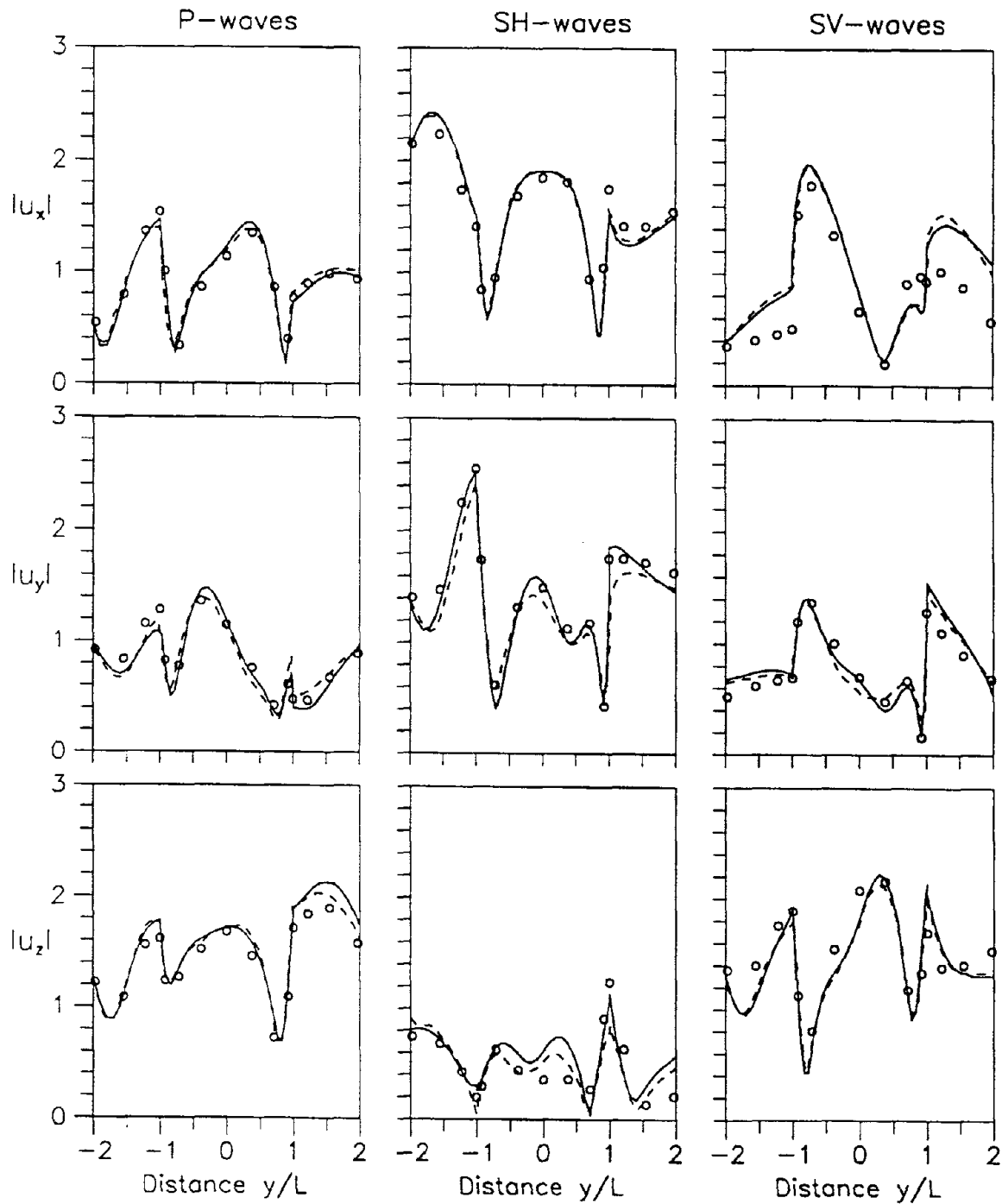


Fig.16 Comparison of results of present method (continuous lines) with previous results (Ref.[34] shown by dashed lines) for P-, SH- and SV-wave excitations ($\Omega = 1.0$, $\theta_h = \theta_v = 45^\circ$, $\eta_p = \eta_s = 0.02$). Results for finite-length canyon ($d = 4L$) are shown by discrete symbols.

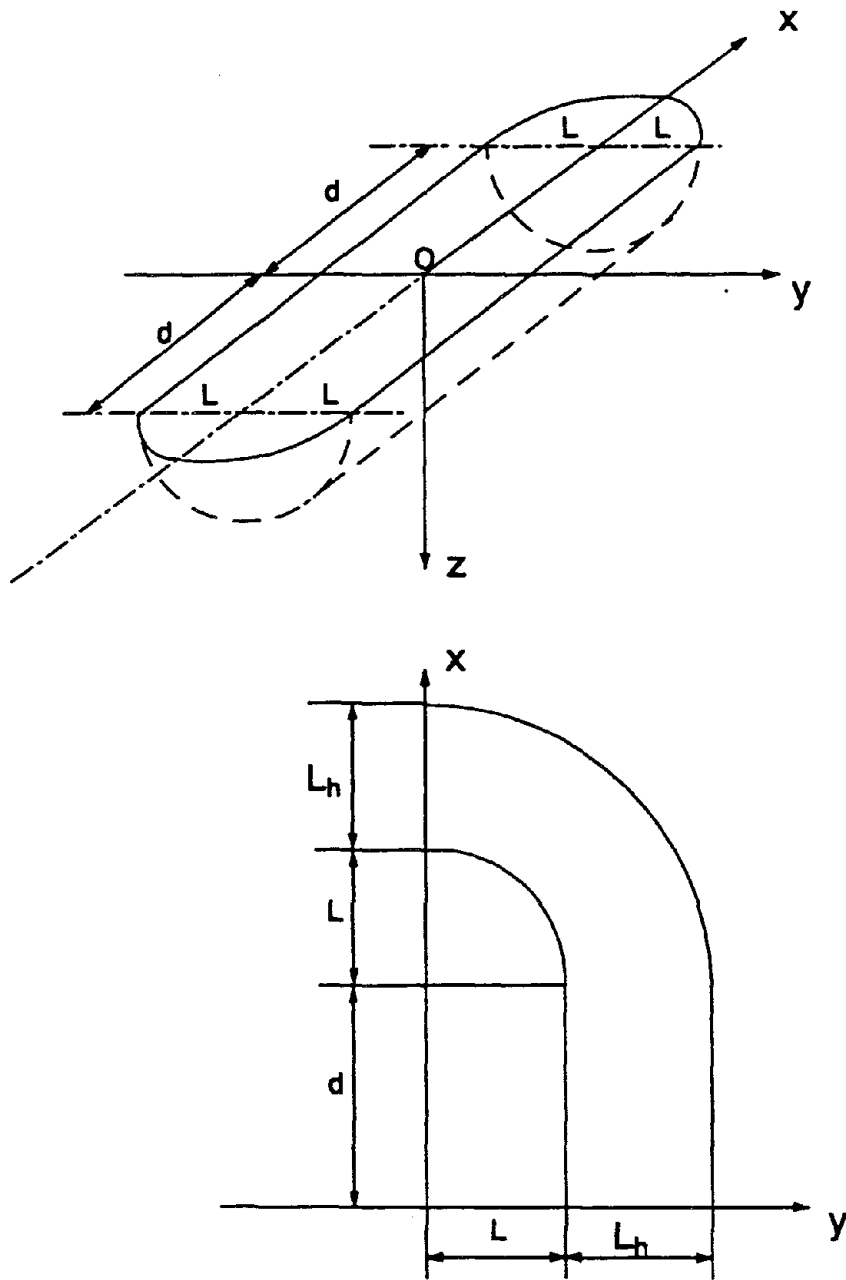


Fig.17 Canyon of finite-length.

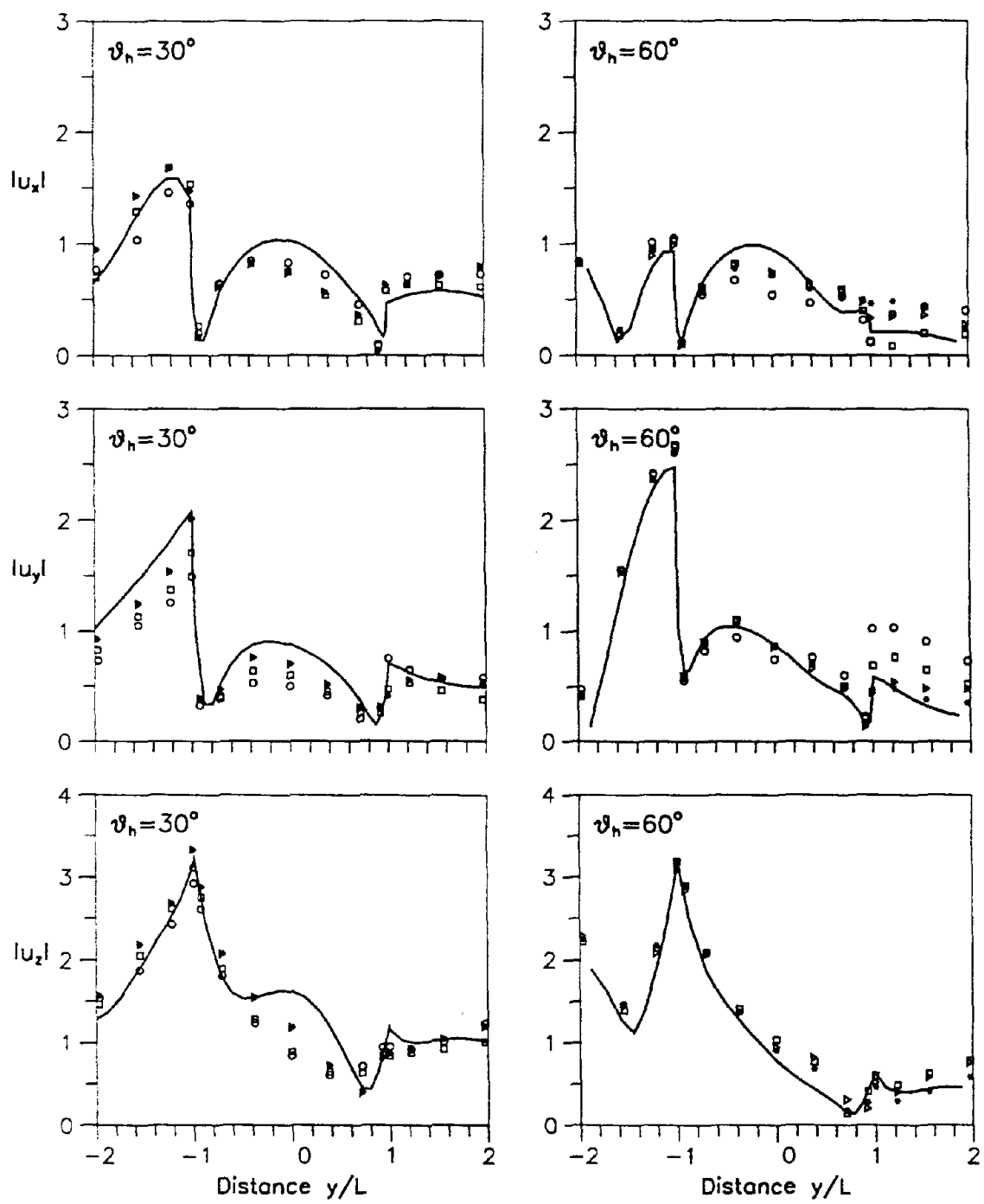
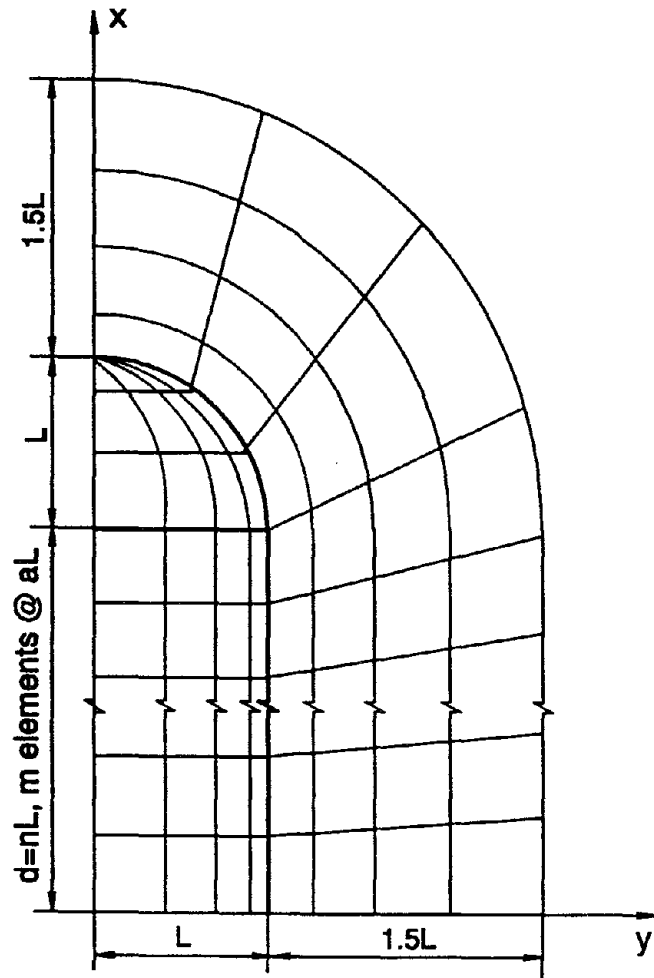


Fig.18 Comparison of results for infinite canyon by the present method (lines) and for finite canyons of different lengths ($d = L$ shown by \circ , $d = 2L$ by \square , $d = 3L$ by \triangleright and $d = 4L$ by $*$) by the 3-D BEM for Rayleigh wave excitation ($\Omega = 1$, $\eta_p = \eta_s = 0.02$).



n	m	a
1	4	0.250
2	6	0.333
3	8	0.375
4	8	0.500

Fig.19 Top view of a quarter of the discretized system for finite canyons of four different lengths.

element method, the present approach is much more efficient as it permits analytical integration along the canyon axis.

CONCLUSIONS

A direct boundary element procedure to calculate the three-dimensional response of an infinitely-long canyon of arbitrary but uniform cross-section cut in a homogeneous viscoelastic half-space to incident seismic waves has been presented. The seismic excitation is represented by P, SH, SV or Rayleigh waves at arbitrary angles with respect to the axis of the canyon. The uniform cross-section of the infinitely-long canyon permits analytical integration along the canyon axis of the three-dimensional boundary integral equation. Thus the original three-dimensional problem is reduced to a computationally efficient "two-dimensional" boundary element problem involving Fourier transforms of full-space Green's functions.

The accuracy of the procedure and implementing computer program has been verified by comparison with previous solutions for the limiting case of two-dimensional response, recently obtained three-dimensional response results for infinitely-long canyons by the indirect boundary method, and three-dimensional boundary element method solutions presented here for finite canyons. The finiteness of the canyon has only a small effect on the displacements far from the ends of the canyon. Compared with the fully three-dimensional version of the boundary element method, the present method is much more efficient as it permits analytical integration along the canyon axis. This method is suitable for research studies concerning the influence of spatial variations in input motions on the earthquake response of arch dams.

REFERENCES

1. P.S. Nowak, "Effect of nonuniform seismic input on arch dams," *Report No. EERL 88-03*, California Institute of Technology, Pasadena, California, 1988.
2. S.B. Kojić and M.D. Trifunac, "Earthquake stresses in arch dams. I: theory and antiplane excitation," *J. Engineering Mechanics, ASCE*, **117**, No. 3, pp.532-552, 1991.
3. S.B. Kojić and M.D. Trifunac, "Earthquake stresses in arch dams. II: excitation by SV-, P-, and Rayleigh waves," *J. Engineering Mechanics, ASCE*, **117**, No. 3, pp.553-574, 1991.
4. M.D. Trifunac, "Scattering of plane SH waves by a semi-cylindrical canyon," *Earthquake Engineering and Structural Dynamics*, **1**, pp.267-281, 1973.
5. H.L. Wong and M.D. Trifunac, "Scattering of plane SH wave by a semi-elliptical canyon," *Earthquake Engineering and Structural Dynamics*, **3**, pp.157-169, 1974.
6. H.L. Wong and P.C. Jennings, "Effects of canyon topography on strong ground motion," *Bull. Seism. Soc. Am.*, **65**, pp.1239-1257, 1975.
7. F.J. Sánchez-Sesma and E. Rosenblueth, "Ground motion at canyons of arbitrary shape under incident SH waves," *Earthquake Engineering and Structural Dynamics*, **7**, pp.441-450, 1979.
8. W.D. Smith, "The application of finite element analysis to body wave propagation problems," *J. Geophys.*, **44**, pp.747-768, 1975.
9. H.L. Wong, "Effect of surface topography on the diffraction of P, SV, and Rayleigh waves," *Bull. Seism. Soc. Am.*, **72**, pp.1167-1183, 1982.
10. F.J. Sánchez-Sesma, M.A. Bravo and I. Herrera, "Surface motion of topographical irregularities for incident P, SV, and Rayleigh waves," *Bull. Seism. Soc. Am.*, **75**, pp.263-269, 1985.
11. H. Cao and V.W. Lee, "Scattering and diffraction of plane P waves by circular cylindrical canyons with variable depth-to-width ratio," *Soil Dynamics and Earthquake Engineering*, **9**, No.3, pp.141-150, 1990.
12. V.W. Lee and H. Cao, "Diffraction of SV waves by circular canyons of various depths," *J. Engineering Mechanics, ASCE*, **115**, No.9, pp.2035-2056, 1989.
13. D.E. Beskos, B. Dasgupta and I.G. Vardoulakis, "Vibration isolation using open or filled trenches," *Computational Mechanics*, **1**, pp.43-63, 1986.
14. R.F. Vogt, J.P. Wolf and H. Bachmann, "Wave scattering by a canyon of arbitrary shape in a layered half-space," *Earthquake Engineering and Structural Dynamics*, **16**, pp.803-812, 1988.
15. H. Kawase, "Time-domain response of a semi-circular canyon for incident SV, P, and Rayleigh waves calculated by the discrete wavenumber boundary element method," *Bull. Seism. Soc. Am.*, **78**, pp.1415-1437, 1988.
16. S. Hirose and M. Kitahara, "Elastic wave scattering by inhomogeneous and anisotropic bodies in a half space," *Earthquake Engineering and Structural Dynamics*, **18**, pp.285-297, 1989.
17. T.K. Mossessian and M. Dravinski, "Application of a hybrid method for scattering of P, SV, and Rayleigh waves by near-surface irregularities," *Bull. Seism. Soc. Am.*, **77**, pp.1784-1803, 1987.
18. F.J. Sánchez-Sesma, "Diffraction of elastic waves by three-dimensional surface irregularities," *Bull. Seism. Soc. Am.*, **73**, pp.1621-1636, 1983.

19. F.J. Sánchez-Sesma, L.E. Pérez-Rocha, and S. Chávez-Pérez, "Diffraction of elastic waves by three-dimensional surface irregularities. Part II," *Bull. Seism. Soc. Am.*, **79**, pp.101-112, 1989.
20. H. Eshraghi and M. Dravinski, "Scattering of Plane Harmonic SH, SV, P, and Rayleigh waves by non-axisymmetric three-dimensional canyons: a wave function expansion approach," *Earthquake Engineering and Structure Dynamics*, **18**, pp.983-998, 1989.
21. T. Mossessian and M. Dravinski, "Amplification of elastic waves by a three dimensional valley, Part I: Steady state response," *Earthquake Engineering and Structural Dynamics*, **19**, pp.667-680, 1990.
22. V.W. Lee, "A note on the scattering of elastic plane waves by a hemispherical canyon," *Soil Dynamics and Earthquake Engineering*, **1**, No.3, pp.122-129, 1982.
23. V.W. Lee, "Three-dimensional diffraction of elastic waves by a spherical cavity in an elastic half-space, I: Closed-form solutions," *Soil Dynamics and Earthquake Engineering*, **7**, No.3, pp.149-161, 1988.
24. P.K. Banerjee, S. Ahmad and K. Chen, "Advanced application of BEM to wave barriers in multi-layered three-dimensional soil media," *Earthquake Engineering and Structural Dynamics*, **16**, pp.1041-1060, 1988.
25. F.J. Rizzo, D.J. Shippy and M. Rezayat, "A boundary integral equation method for radiation and scattering of elastic waves in three dimensions," *Int. J. for Numerical Methods in Engineering*, **21**, pp.115-129, 1985.
26. M. Rezayat, D.J. Shippy and F.J. Rizzo, "On time-harmonic elastic-wave analysis by the boundary element method for moderate to high frequencies," *Computer Methods in Applied Mechanics and Engineering*, **55**, pp.349-367, 1986.
27. H.L. Wong, "Effects of surface topography and site conditions," *Strong Ground Motion Simulation and Earthquake Engineering Applications* (R.E.Scholl and J.L.King Eds.), Earthquake Engineering Research Institute, Berkeley, CA, pp.24-1 to 24-5, Nov. 1985.
28. D.E. Beskos, "Boundary element methods in dynamic analysis," *Applied Mechanics Reviews*, **40**, No.1, pp.1-23, 1987.
29. F.J. Sánchez-Sesma, "Site effects on strong ground motion," *Soil Dynamics and Earthquake Engineering*, **6**, No.2, pp.124-132, 1987.
30. K.C. Wong, S.K. Datta and A.H. Shah, "Three dimensional motion of a buried pipeline. I. analysis," *J. Engineering Mechanics, ASCE*, **112**, No. 12, pp.1319-1337, 1986.
31. J.E. Luco and J.G. Anderson, "Steady-state response of an elastic half-space to a moving dislocation of finite width," *Bull. Seism. Soc. Am.*, **73**, pp.1-22, 1983.
32. A. Mendez and J.E. Luco, "Near-source ground motion from a steady-state dislocation model in a layered half-space," *J. Geophysical Research*, **93**, pp.12041-12054, 1988.
33. S.W. Liu, S.K. Datta, M. Bouden and A.H. Shah, "Scattering of obliquely incident seismic waves by a cylindrical valley in a layered half-space," *Earthquake Engineering and Structural Dynamics*, to be published.
34. J.E. Luco, H.L. Wong and F.C.P. de Barros, "Three-dimensional response of a cylindrical canyon in a layered half-space," *Earthquake Engineering and Structural Dynamics*, **19**, pp.799-818, 1990.
35. K.F. Graff, *Wave Motion in Elastic Solids*, Ohio State University Press, 1975.

36. J.E. Luco and H.L. Wong, "Seismic Response of Foundations Embedded in a Layered Half-Space," *Earthquake Engineering and Structural Dynamics*, **15**, pp.233-247, 1987.
37. J.P. Wolf and P. Oberhuber, "Free-Field Response from Inclined SV- And P-Waves And Rayleigh-Waves," *Earthquake Engineering and Structural Dynamics*, **10**, pp.847-869, 1982.
38. A.C. Eringen and E.S. Suhubi, *Elastodynamics, Vol.II, Linear Theory*, Academic Press, N.Y., 1975.
39. F. Hartmann, "Computing the C-matrix in non-smooth boundary points," *New Developments in Boundary Element Methods*, (Ed. by C.A.Brebbia), CML Publications, pp.367-379, 1980.

NOTATION

a	numerical coefficient
a_p	$= \sqrt{k^2 - k_p^2}$
a_s	$= \sqrt{k^2 - k_s^2}$
A	measure of incident wave amplitude
$[A]$	square coefficient matrix for the boundary element system (equation 32)
$[\tilde{A}]$	$3 \times 3M_n$ matrix assembled from the integrals of the products of $[F]^T$ and $[N]$ associated with a single source point (equation 28)
A_1, A_2	numerical coefficients
A_p	amplitude of reflected P wave
A_s	amplitude of reflected SV wave
b	numerical constant
b_L	$= k_r(1 - c_r^2/c_p^2)^{1/2}$
b_T	$= k_r(1 - c_r^2/c_s^2)^{1/2}$
c_p	P wave velocity including damping
\bar{c}_p	P wave velocity without damping
c_r	Rayleigh wave velocity including damping
\bar{c}_r	Rayleigh wave velocity without damping
c_s	shear wave velocity including damping
\bar{c}_s	shear wave velocity without damping
$[C(\vec{x})]$	3×3 matrix related to the geometric shape of the boundary at \vec{x} (equation 20)
d	$= \sqrt{(x - x_s)^2 + (y - y_s)^2 + (z - z_s)^2}$, distance between source and receiver points
\bar{d}	$= \sqrt{(y - y_s)^2 + (z - z_s)^2}$, distance between source and receiver points projected on plane $x = 0$
f	frequency in Hz
$[F]$	transformed full-space Green's traction functions (equation 18b)

$[F^*]$	traction functions associated with full-space Green's displacement functions $[G^*]$
$[F_0]$	traction functions associated with the transformed full-space Green's displacement functions $[F]$ for $k = 0$ (equation 22b)
$[G]$	transformed full-space Green's displacement functions (equation 18a)
$[G^*]$	full-space Green's displacement functions
$[G_0]$	transformed full-space Green's displacement functions for $k = 0$ (equation 22a)
i	$= \sqrt{-1}$
k	wavenumber in x -direction
k'	wavenumber in x' -direction
k_p	P wavenumber
k_r	Rayleigh wavenumber
k_s	shear wavenumber
$K_0(), K_1()$	modified Bessel functions of second kind of order zero and order one
l_j	length of the j th element on $\bar{\Gamma}_c \cup \bar{\Gamma}_h$
L	half width of the uniform canyon
L_h	discretization range on the half-space surface
M	number of one-dimensional elements on the boundaries $\bar{\Gamma}_c \cup \bar{\Gamma}_h$
M_n	number of nodes on the boundaries $\bar{\Gamma}_c \cup \bar{\Gamma}_h$
M_1, M_2	element number for the first and the last one-dimensional elements on boundary $\bar{\Gamma}_c$
n, n_1, n_2, n_3	outgoing normal to the boundary and its components
$[N]; N_j$	shape function matrix for the one-dimensional element on $\bar{\Gamma}_c \cup \bar{\Gamma}_h$; j th shape function
N_c	number of elements on canyon boundary $\bar{\Gamma}_c$
N_h	number of elements on one side of the half-space boundary $\bar{\Gamma}_h$
$\{P\}, P_x, P_y, P_z$	vector and components of concentrated forces associated with the second elastodynamic state

$\{Q\}$	vector assembled from $\{\tilde{Q}\}$ associated with all nodes on $\bar{\Gamma}_c \cup \bar{\Gamma}_h$ (equation 33)
$\{\tilde{Q}\}$	3×1 vector from integrals of the products of transformed Green's displacement functions and the free-field tractions (equation 29)
r_s	radius of a circular curve around a source point
S	the entire boundary of the system which consists of the surface of the half-space and the boundary of the canyon
t	time
$\{t\}$	traction vector
$\{\bar{t}\}$	traction vector at plane $x = 0$
$\{t^*\}$	traction vector associated with the second elastodynamic state in reciprocal theorem
$\{t_{ff}\}$	traction vector associated with the free-field motion
$\{\bar{t}_{ff}\}$	traction vector associated with the free-field motion at plane $x = 0$
$\{t_s\}$	traction vector associated with the scattered field motion
$[T]$	3×3 coordinate transformation matrix (equation 6)
$\{u\}$	displacement vector
$\{\bar{u}\}$	displacement vector at plane $x = 0$
$\{u'\}$	displacement vector in $x'y'z'$ -coordinate system
$\{\bar{u}'\}$	displacement vector at plane $x' = 0$ in $x'y'z'$ -coordinate system
$\{u^*\}$	displacement vector for the second elastodynamic state in reciprocal theorem
$\{u_{ff}\}$	displacement vector for the free-field motion
$\{\bar{u}_{ff}\}$	displacement vector for the free-field motion at plane $x = 0$
$\{u'_{ff}\}$	displacement vector for the free-field motion in $x'y'z'$ -coordinate system
$\{\bar{u}'_{ff}\}$	displacement vector for the free-field motion at plane $x' = 0$ in $x'y'z'$ -coordinate system
$\{u_s\}$	displacement vector for the scattered field
$\{\bar{u}_s\}$	displacement vector for the scattered field at plane $x = 0$
$\{\bar{U}\}, \bar{U}_{xj}, \bar{U}_{yj}, \bar{U}_{zj}$	vector containing nodal displacements at plane $x = 0$ and its components at the j th node

x, y, z	spatial coordinates
x', y', z'	spatial coordinates in $x'y'z'$ -coordinate system
x_s, y_s, z_s	spatial coordinates of source point
\bar{x}	$= (x, y, z)$, an arbitrary point
\bar{x}'	$= (x', y', z')$, an arbitrary point in $x'y'z'$ -coordinate system
\bar{x}_o	$= (0, y, z)$, an arbitrary point at plane $x = 0$
\bar{x}_{o_s}	$= (0, y_s, z_s)$, a source point at plane $x = 0$
α	number
β	number
γ	numerical coefficient
Γ_c	canyon surface
$\bar{\Gamma}_c$	cross-section of the canyon at plane $x = 0$
Γ_h	half-space surface
$\bar{\Gamma}_h$	cross-section of the half-space surface at plane $x = 0$
$\bar{\Gamma}_j$	extent of the j th element
$\bar{\Gamma}_s$	small contour of radius r_s around the source point at plane $x = 0$
δ_{nj}	Kronecker delta function
ζ	natural coordinate
η_p	constant hysteretic damping factor for P wave
η_r	constant hysteretic damping factor for Rayleigh wave
η_s	constant hysteretic damping factor for shear wave
θ_{cr}	critical incidence angle for SV wave
θ_h	azimuth incidence angle between the wave propagation plane and x -axis (Figure 2)
θ_v	angle between the normal to the incident wave front and the vertical axis (Figure 2)
λ_s	shear wavelength
μ	shear modulus for the half-space medium
ν	Poisson's ratio for the half-space medium

ν'	wavenumber in z' -direction
ρ	material density for the half-space medium
ϕ_1, ϕ_2	angles of tangent lines passing through a non-smooth boundary point on $\bar{\Gamma}_c \cup \bar{\Gamma}_h$
ω	frequency in rad/sec.
Ω	non-dimensional frequency defined by $\Omega = \omega L / \pi \bar{c}_s$

APPENDIX A: FREE-FIELD GROUND MOTIONS FOR SH, P, SV AND RAYLEIGH WAVES

By definition, the free-field motion is the displacement field that exists inside the half-space in absence of the canyon. Except for incident Rayleigh surface wave, the free-field motion consists of the incident wave and waves reflected by the half-space surface. In the following expressions, the waves are assumed to travel parallel to $x' - z'$ plane (see Figure 2). The vertical incidence angle is θ_v and the amplitudes of the reflected P and S waves are A_p and A_s , respectively. In $x'y'z'$ -coordinate system, the free-field displacement fields can be expressed as [35]:

For Incident SH Wave

$$\{u'_{ff}(\vec{x}')\} = \begin{pmatrix} 0 \\ 1 \\ 0 \end{pmatrix} e^{k_s(-\sin\theta_v x' + \cos\theta_v z')}i + \begin{pmatrix} 0 \\ 1 \\ 0 \end{pmatrix} e^{k_s(-\sin\theta_v x' - \cos\theta_v z')}i \quad (A \cdot 1)$$

For Incident P Wave

$$\begin{aligned} \{u'_{ff}(\vec{x}')\} = & \begin{pmatrix} \sin\theta_v \\ 0 \\ -\cos\theta_v \end{pmatrix} e^{k_p(-\sin\theta_v x' + \cos\theta_v z')}i + A_p \begin{pmatrix} \sin\theta_v \\ 0 \\ \cos\theta_v \end{pmatrix} e^{k_p(-\sin\theta_v x' - \cos\theta_v z')}i \\ & + A_s \begin{pmatrix} \cos\gamma \\ 0 \\ -\sin\gamma \end{pmatrix} e^{k_s(-\sin\gamma x' - \cos\gamma z')}i \end{aligned} \quad (A \cdot 2)$$

where

$$\begin{aligned} \sin\gamma &= \frac{c_s}{c_p} \sin\theta_v \\ A_p &= \frac{\sin(2\theta_v)\sin(2\gamma) - (c_p/c_s)^2 \cos^2(2\gamma)}{\sin(2\theta_v)\sin(2\gamma) + (c_p/c_s)^2 \cos^2(2\gamma)} \\ A_s &= \frac{2(c_p/c_s)\sin(2\theta_v)\cos(2\gamma)}{\sin(2\theta_v)\sin(2\gamma) + (c_p/c_s)^2 \cos^2(2\gamma)} \end{aligned}$$

For Incident SV Wave

The free-field motions for incident SV wave are given by two different expressions, depending on whether the vertical incidence angle θ_v is smaller than the critical incidence angle θ_{cr} defined by

$$\theta_{cr} = \arcsin(c_s/c_p)$$

(1) $\theta_v < \theta_{cr}$

$$\begin{aligned} \{u'_{ff}(\vec{x}')\} &= \begin{pmatrix} \cos\theta_v \\ 0 \\ \sin\theta_v \end{pmatrix} e^{k_s(-\sin\theta_v x' + \cos\theta_v z')i} + A_s \begin{pmatrix} -\cos\theta_v \\ 0 \\ \sin\theta_v \end{pmatrix} e^{-k_s(\sin\theta_v x' + \cos\theta_v z')i} \\ &+ A_p \begin{pmatrix} \sin\gamma \\ 0 \\ \cos\gamma \end{pmatrix} e^{k_p(-\sin\gamma x' - \cos\gamma z')i} \end{aligned} \quad (A \cdot 3)$$

where

$$\begin{aligned} \sin\gamma &= \frac{c_p}{c_s} \sin\theta_v \\ A_s &= \frac{(c_p/c_s) \sin(4\theta_v)}{\sin(2\theta_v) \sin(2\gamma) + (c_p/c_s)^2 \cos^2(2\theta_v)} \\ A_p &= \frac{\sin(2\theta_v) \sin(2\gamma) - (c_p/c_s)^2 \cos^2(2\theta_v)}{\sin(2\theta_v) \sin(2\gamma) + (c_p/c_s)^2 \cos^2(2\theta_v)} \end{aligned}$$

(2) $\theta_v > \theta_{cr}$

$$\begin{aligned} \{u'_{ff}(\vec{x}')\} &= \begin{pmatrix} \cos\theta_v \\ 0 \\ \sin\theta_v \end{pmatrix} e^{k_s(-\sin\theta_v x' + \cos\theta_v z')i} + iA_1 \begin{pmatrix} -\cos\theta_v \\ 0 \\ \sin\theta_v \end{pmatrix} e^{-k_s(\sin\theta_v x' + \cos\theta_v z')i} \\ &- A_2 \begin{pmatrix} ik_s \sin\theta_v \\ 0 \\ a \end{pmatrix} e^{-az' - ik_s \sin\theta_v x'} \end{aligned} \quad (A \cdot 4)$$

where

$$\begin{aligned} a &= \sqrt{k_s^2 \sin^2\theta_v - k_p^2} \\ A_1 &= \frac{-2a \sin\theta_v \sin(2\theta_v) + k_s \cos^2(2\theta_v)i}{k_s \cos^2(2\theta_v) - 2a \sin\theta_v \sin(2\theta_v)i} \\ A_2 &= \frac{k_s \sin(4\theta_v)i}{k_s [k_s \cos^2(2\theta_v) - 2a \sin\theta_v \sin(2\theta_v)i]} \end{aligned}$$

For Incident Rayleigh Wave

$$\{u'_{ff}(\vec{x}')\} = \begin{pmatrix} e^{-b_L z'} - \frac{1}{2} \left(2 - \frac{c_r^2}{c_s^2}\right) e^{-b_T z'} \\ 0 \\ ik_r \left[-\frac{b_L}{k_r^2} e^{-b_L z'} + \frac{1}{2b_T} \left(2 - \frac{c_r^2}{c_s^2}\right) e^{-b_T z'}\right] \end{pmatrix} e^{-ik_r x'} \quad (A \cdot 5)$$

where

$$\begin{aligned} b_L &= k_r \left(1 - \frac{c_r^2}{c_p^2}\right)^{1/2} \\ b_T &= k_r \left(1 - \frac{c_r^2}{c_s^2}\right)^{1/2} \end{aligned}$$

and c_r and k_r are Rayleigh wave velocity and the corresponding wavenumber.

APPENDIX B: FULL-SPACE GREEN'S FUNCTIONS

The full-space Green's functions can be found in Reference [38]. Let the source and receiver points be $\vec{x}_{os} = (x_{o1}, x_{o2}, x_{o3})$ and $\vec{x} = (x_1, x_2, x_3)$ respectively and n be the normal to the surface at the receiver \vec{x} with corresponding components denoted by $n = (n_1, n_2, n_3)$ where, in order to make the formulation compact, the coordinate notations have been changed from (x, y, z) to (x_1, x_2, x_3) . The displacement and traction components at \vec{x} in the j th direction due to concentrated force at \vec{x}_{os} in the k th direction are given by

$$G_{jk}^*(\vec{x}, \vec{x}_{os}) = \frac{1}{4\pi\rho} \left\{ \left(\frac{3d_j d_k}{d^3} - \frac{\delta_{jk}}{d} \right) \left[\frac{1}{\omega^2 d^2} (e^{-ik_s d} - e^{-ik_p d}) + \frac{i}{\omega d} \left(\frac{1}{c_s} e^{-ik_s d} - \frac{1}{c_p} e^{-ik_p d} \right) \right] \right. \\ \left. + \frac{d_j d_k}{d^3} \left(\frac{1}{c_p^2} e^{-ik_p d} - \frac{1}{c_s^2} e^{-ik_s d} \right) + \frac{\delta_{jk}}{d c_s^2} e^{-ik_s d} \right\} \quad (B \cdot 1)$$

$$\begin{aligned} \overset{n}{F}_{jk}^*(\vec{x}, \vec{x}_{os}) = & \frac{n_l}{4\pi} \left\{ -6c_s^2 \left[\frac{5d_j d_k d_l}{d^5} - \frac{\delta_{jk} d_l + \delta_{kl} d_j + \delta_{jl} d_k}{d^3} \right] \right. \\ & \times \left[\frac{1}{\omega^2 d^2} (e^{-ik_s d} - e^{-ik_p d}) + \frac{i}{\omega d} \left(\frac{1}{c_s} e^{-ik_s d} - \frac{1}{c_p} e^{-ik_p d} \right) \right] \\ & + 2 \left[\frac{6d_j d_k d_l}{d^5} - \frac{\delta_{jk} d_l + \delta_{kl} d_j + \delta_{jl} d_k}{d^3} \right] \left(e^{-ik_s d} - \frac{c_s^2}{c_p^2} e^{-ik_p d} \right) \\ & + \frac{2ik_s d_j d_k d_l}{d^4} \left(e^{-ik_s d} - \frac{c_s^3}{c_p^3} e^{-ik_p d} \right) - \frac{d_k \delta_{jl}}{d^3} \left(1 - 2\frac{c_s^2}{c_p^2} \right) (1 + ik_p d) e^{-ik_p d} \\ & \left. - \frac{\delta_{jk} d_l + \delta_{kl} d_j}{d^3} (1 + ik_s d) e^{-ik_s d} \right\} \quad (B \cdot 2) \end{aligned}$$

where $j, k, l = 1, 2, 3$,

$$d_1 = x_1 - x_{o1}$$

$$d_2 = x_2 - x_{o2}$$

$$d_3 = x_3 - x_{o3}$$

$$d^2 = d_1^2 + d_2^2 + d_3^2$$

and k_p and k_s are P and S wavenumbers, respectively.

APPENDIX C: TRANSFORMED GREEN'S FUNCTIONS

Transformed Green's Displacement Functions

The transformed Green's displacement functions are defined (equation 18a) by

$$G_{ij}(\vec{x}_o, \vec{x}_{os}, k) = \int_{-\infty}^{\infty} G_{ij}^*(\vec{x}, \vec{x}_{os}) e^{-ikx_1} dx_1, \quad i, j = 1, 2, 3 \quad (C \cdot 1)$$

where $G_{ij}^*(\vec{x}, \vec{x}_{os})$ is the i th displacement component at receiver point $\vec{x} = (x_1, x_2, x_3)$ due to concentrated force at source point $\vec{x}_{os} = (0, x_{o2}, x_{o3})$ in the j th direction in full-space. In order to make the formulations compact, the notation for the coordinates has been changed from (x, y, z) to (x_1, x_2, x_3) . Correspondingly, the coordinates of the source point become $(0, x_{o2}, x_{o3})$.

From Reference [38], the Green's displacement functions, G_{ij}^* , can be expressed either in the form given in Appendix B or in the following more compact form

$$G_{ij}^* = \frac{1}{4\pi\rho} \left[\frac{1}{\omega^2} \frac{\partial^2}{\partial x_i \partial x_j} \left(\frac{e^{-ik_s d} - e^{-ik_p d}}{d} \right) + \frac{\delta_{ij}}{dc_s^2} e^{-ik_s d} \right] \quad i, j = 1, 2, 3 \quad (C \cdot 2)$$

where d is the distance between the source and receiver points

$$d = \sqrt{x_1^2 + (x_2 - x_{o2})^2 + (x_3 - x_{o3})^2}$$

In order to obtain explicit expressions for G_{ij} , it is necessary to use following relation

$$\int_{-\infty}^{\infty} \frac{e^{ibd}}{d} e^{-ikx_1} dx_1 = 2K_o(\bar{d}\sqrt{k^2 - b^2}) \quad (C \cdot 3)$$

where b is a complex constant, \bar{d} is the distance between the source and receiver projected to the plane $x_1 = 0$:

$$\bar{d} = \sqrt{(x_2 - x_{o2})^2 + (x_3 - x_{o3})^2}$$

and $K_o()$ is modified Bessel function of the zeroth order.

Substituting (C·2) into (C·1) and utilizing (C·3) lead to

$$G_{11} = \frac{1}{2\pi\mu} \left[K_o(a_s \bar{d}) \left(1 - \frac{k^2}{k_s^2} \right) + \frac{k^2}{k_s^2} K_o(a_p \bar{d}) \right] \quad (C \cdot 4)$$

$$G_{1j} = G_{j1} = \frac{1}{2\pi\mu} \frac{ik}{k_s^2} \frac{\partial}{\partial x_j} [K_o(a_s \bar{d}) - K_o(a_p \bar{d})], \quad j = 2, 3 \quad (C \cdot 5)$$

$$G_{\alpha\beta} = \frac{1}{2\pi\mu} \left[\frac{1}{k_s^2} \frac{\partial^2}{\partial x_\alpha \partial x_\beta} [K_o(a_s \bar{d}) - K_o(a_p \bar{d})] + \delta_{\alpha\beta} K_o(a_s \bar{d}) \right], \quad \alpha, \beta = 2, 3 \quad (C \cdot 6)$$

where

$$a_p = \sqrt{k^2 - k_p^2}$$

$$a_s = \sqrt{k^2 - k_s^2}$$

and μ is the shear modulus for the full-space medium. It should be pointed out that k is a real variable while a_p and a_s are complex numbers in general. When damping is included, a_p and a_s never vanish. Thus, G_{ij} is always bounded for $\bar{d} \neq 0$.

Transformed Green's Traction Functions

The transformed Green's traction functions $\bar{F}_{ij}^n(\bar{x}_o, \bar{x}_{os}, k)$ are defined (equation 18b) by

$$\bar{F}_{ij}^n(\bar{x}_o, \bar{x}_{os}, k) = \int_{-\infty}^{\infty} \bar{F}_{ij}^{*n}(\bar{x}, \bar{x}_{os}) e^{-ikx_1} dx_1 \quad i, j = 1, 2, 3 \quad (C \cdot 7)$$

where $\bar{F}_{ij}^{*n}(\bar{x}, \bar{x}_{os})$ is the i th traction component at the receiver point $\bar{x} = (x_1, x_2, x_3)$ due to a concentrated force at source point $\bar{x}_{os} = (0, x_{o2}, x_{o3})$ in j th direction. \bar{F}_{ij}^{*n} can be obtained by substituting the expressions of \bar{F}_{ij}^{*n} , which are given in Appendix B, into (C.7) and finding the integrations term by term. However, since finding derivatives is much easier than deriving integrations, it is more convenient to find \bar{F}_{ij}^n through following ways:

(1) Assume a displacement field given by

$$u_{ij} = G_{ij}(\bar{x}_o, \bar{x}_{os}, k) e^{ikx_1} \quad (C \cdot 8)$$

(2) Find the corresponding stresses and tractions for this field and express the latter as

$$t_{ij} = \bar{F}_{ij}^n(\bar{x}_o, \bar{x}_{os}, k) e^{ikx_1} \quad (C \cdot 9)$$

(3) Remove e^{ikx_1} from (C.9) and one obtains \bar{F}_{ij}^n

It can be shown that \bar{F}_{ij}^n thus obtained are the same as what would be obtained by substituting \bar{F}_{ij}^* into equation (C·7) and deriving the integrations term by term.

The final expressions for \bar{F}_{ij}^n are given by ($j = 1, 2, 3$)

$$\bar{F}_{1j}^n = \mu \left[n_2 \left(\frac{\partial G_{1j}}{\partial x_2} + ikG_{2j} \right) + n_3 \left(\frac{\partial G_{1j}}{\partial x_3} + ikG_{3j} \right) \right] \quad (C \cdot 10)$$

$$\bar{F}_{2j}^n = \mu \left\{ \frac{2n_2}{1-2\nu} \left[ik\nu G_{1j} + (1-\nu) \frac{\partial G_{2j}}{\partial x_2} + \nu \frac{\partial G_{3j}}{\partial x_3} \right] + n_3 \left(\frac{\partial G_{2j}}{\partial x_3} + \frac{\partial G_{3j}}{\partial x_2} \right) \right\} \quad (C \cdot 11)$$

$$\bar{F}_{3j}^n = \mu \left\{ \frac{2n_3}{1-2\nu} \left[ik\nu G_{1j} + (1-\nu) \frac{\partial G_{3j}}{\partial x_3} + \nu \frac{\partial G_{2j}}{\partial x_2} \right] + n_2 \left(\frac{\partial G_{2j}}{\partial x_3} + \frac{\partial G_{3j}}{\partial x_2} \right) \right\} \quad (C \cdot 12)$$

where n_2 and n_3 are the components of outgoing normal to the surface, $n = (0, n_2, n_3)$, and ν is the Poisson's ratio for the half-space medium.

Expression for Matrix [C]

Matrix [C] depends on the position of the source point; and, when the source point is on the boundary, it is a function of the geometric shape of the system at the source point. From equation (20), matrix [C] is defined by

$$[C(\bar{x}_{os})] = \lim_{r, -0} \int_{\Gamma_s} [\bar{F}^n(\bar{x}_o, \bar{x}_{os}, k)]^T d\Gamma \quad (C \cdot 13)$$

Substituting $[\bar{F}^n]$ into (C·13) and following similar procedures presented in Reference [39], it can be found that

$$[C(\bar{x}_{os})] = \begin{bmatrix} C_{11} & 0 & 0 \\ 0 & C_{22} & C_{23} \\ 0 & C_{32} & C_{33} \end{bmatrix} \quad (C \cdot 14)$$

where

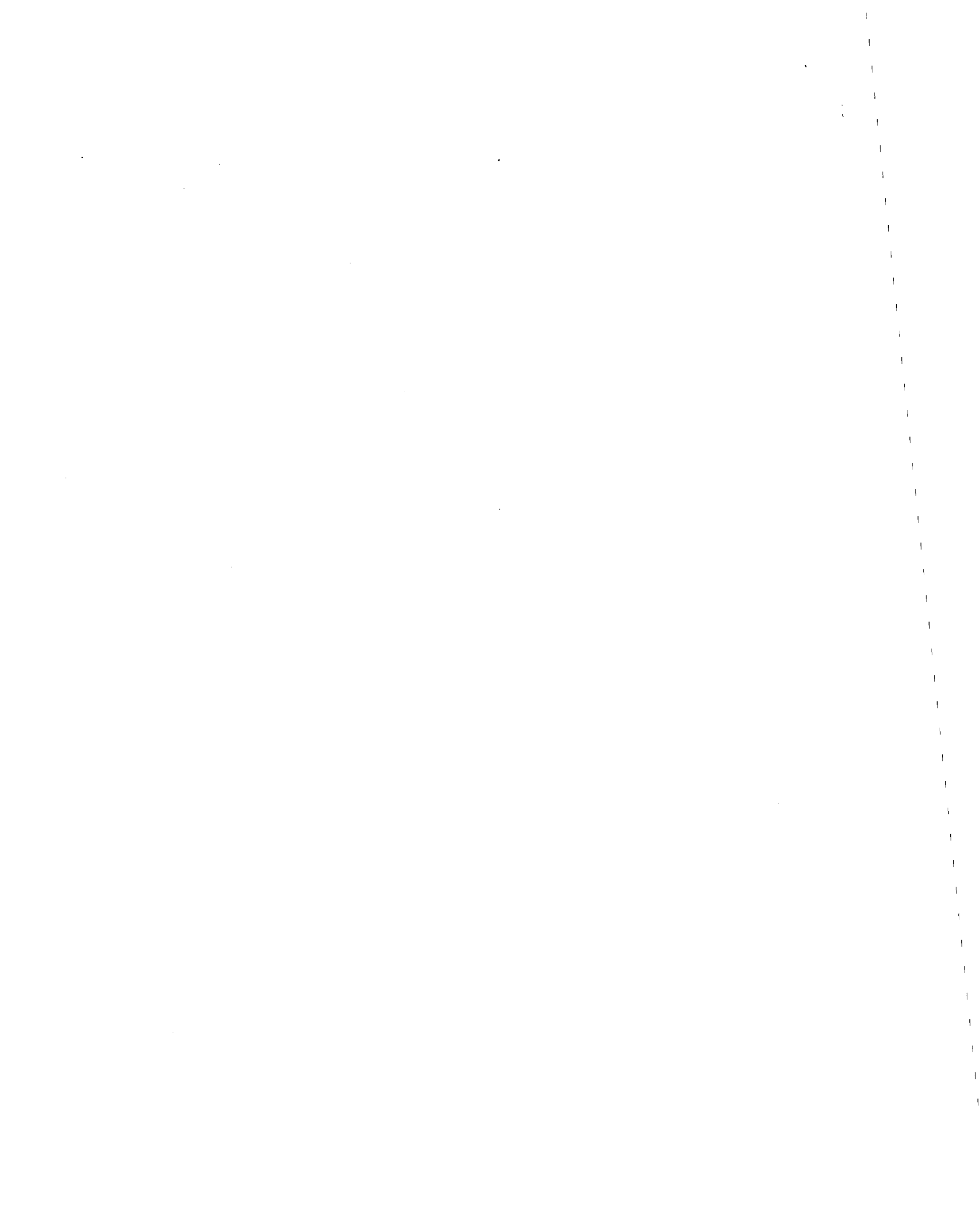
$$C_{11} = \frac{1}{2\pi}(\phi_1 - \phi_2) \quad (C \cdot 15)$$

$$C_{22} = \frac{1}{4\pi(1-\nu)} \left[2(1-\nu)(\phi_1 - \phi_2) + \frac{1}{2}(\sin(2\phi_1) - \sin(2\phi_2)) \right] \quad (C \cdot 16)$$

$$C_{23} = C_{32} = \frac{1}{4\pi(1-\nu)} (\sin^2 \phi_1 - \sin^2 \phi_2) \quad (C \cdot 17)$$

$$C_{33} = \frac{1}{4\pi(1-\nu)} \left[2(1-\nu)(\phi_1 - \phi_2) - \frac{1}{2}(\sin(2\phi_1) - \sin(2\phi_2)) \right] \quad (C \cdot 18)$$

In the above equations, ϕ_1 and ϕ_2 are the angles of tangent lines passing through the source point \bar{x}_{os} at the boundary. The detailed definition of ϕ_1 and ϕ_2 can be found in Reference [39].



PART II

**IMPEDANCE FUNCTIONS FOR THREE-DIMENSIONAL
FOUNDATIONS SUPPORTED ON AN INFINITELY-
LONG CANYON OF UNIFORM CROSS-SECTION IN A
HOMOGENEOUS HALF-SPACE**

INTRODUCTION

Required in the substructure method for earthquake analysis of concrete dams is the impedance matrix (or the frequency-dependent stiffness matrix) for the foundation rock region, defined at the nodal points on the dam-foundation rock interface [1,2]. Computation of this foundation impedance matrix for analysis of arch dams requires solution of a series of mixed boundary value problems governing the steady-state response of the canyon cut in a three-dimensional, unbounded foundation rock region. Because such analyses are extremely complicated, usually only the foundation flexibility is considered in analysis of arch dams, i.e. the material and radiation damping as well as inertial effects of the foundation rock are ignored [2-4]. The objective of this work is to overcome these limitations with the long term goal of analyzing the earthquake response of arch dams including dam-foundation rock interaction.

Computation of foundation impedance matrices has been the subject of many investigations over the past two decades leading to a variety of analysis techniques. Impedance matrices for two-dimensional embedded foundations have been determined by the indirect boundary element method (BEM) with half-space Green's functions [5], direct boundary element method with full-space Green's functions [6], and by a hybrid method [7]. Procedures were developed to determine the impedance matrices for three-dimensional surface-supported or embedded foundations by an integral equation technique with half-space Green's functions [8,9], nonsingular integral equation approach [10-12], and a hybrid method combining indirect BEM with FEM using half-space Green's functions [13].

Boundary methods utilizing half-space Green's functions have the advantage that they are applicable to layered media and do not require discretization of the half-space surface. However, because of the high cost in computing half-space Green's functions, application of these methods has been restricted to either arbitrary-shape, surface-supported foundations or axisymmetric embedded foundations. In contrast, full-space

Green's functions are simple to compute and have been used widely in the direct BEM to determine foundation impedance matrices [14-19]. However, use of full-space Green's functions seems computationally impractical for analysis of foundations in layered media because of the requirement to discretize interfaces between layers.

In addition to various boundary methods using different Green's functions, other techniques have been developed for evaluation of foundation impedance matrices. These include the finite element method in the frequency domain with transmitting boundaries [20-23], finite element method in the time domain [24], spherical wave function expansion approach [25], infinite element approach [26,27] and various hybrid methods [e.g. 28,29]. More extensive reviews of the various techniques developed to determine foundation impedance matrices are available in [30,31].

The various techniques mentioned above have been applied to the analysis of a wide variety of foundations either supported on the surface of a half-space or embedded in a finite-sized excavation in the half-space. However, these techniques appear to be either inapplicable or computationally impractical for the system of Figure 1. It is an infinitely-long canyon of arbitrary but uniform cross-section cut in a homogeneous viscoelastic half-space. In this work this system is analyzed to determine the impedance matrix at the arch dam-foundation rock interface by the direct boundary element method in conjunction with full-space Green's functions. The uniform cross-section of the infinitely-long canyon, which seems to be a reasonable idealization for practical analysis of arch dams, permits analytical integration along the canyon axis leading to a series of two-dimensional boundary problems involving Fourier transforms of the full-space Green's functions. The assumption of a homogeneous half-space seems to be appropriate for arch dam sites where similar rock usually extends to considerable depth.

PROBLEM STATEMENT

The system considered is an arch dam, idealized as a finite element system,

supported in an infinitely-long canyon of arbitrary but uniform cross-section cut in a homogeneous half-space (Figure 1). The substructure method has proven to be an effective approach to the earthquake analysis of dams including dam-foundation rock interaction effects. These interaction effects introduce an impedance matrix, or a dynamic (frequency-dependent) stiffness matrix, for the foundation rock region in the equations of motion governing the steady-state response of the dam to harmonic ground motion.

Our objective is to determine the impedance matrix, $[S_f(\omega)]$, where ω is the frequency of the harmonic excitation, defined at the interface Γ_i between the dam and foundation rock. This impedance matrix, $[S_f(\omega)]$, relates the interaction forces $\{R(t)\}$ at the interface Γ_i to the corresponding displacements $\{r(t)\}$, relative to the earthquake induced ground displacements in the absence of the dam:

$$[S_f(\omega)]\{\bar{r}(\omega)\} = \{\bar{R}(\omega)\} \quad (1)$$

where the overbar denotes Fourier transform of the time-functions. The square matrix $[S_f(\omega)]$ is of order equal to the number of degrees-of-freedom (DOF) in the finite element idealization at the interface. The n th column of this matrix multiplied by $e^{i\omega t}$ is the set of complex-valued forces required at the interface DOF to maintain a unit harmonic displacement, $e^{i\omega t}$, in the n th DOF with zero displacements in all other DOF.

Evaluation of these forces requires solution of a series of mixed boundary value problems with displacements prescribed at the interface Γ_i and tractions outside Γ_i — on the canyon as well as the half-space surface — are prescribed as zero. Instead of directly solving this mixed boundary value problem, it is more convenient to solve a stress boundary value problem in which non-zero tractions are specified at the interface Γ_i and the resulting displacements at Γ_i are determined. Assembled from these displacements, the dynamic flexibility influence matrix is inverted to determine the matrix $[S_f(\omega)]$.

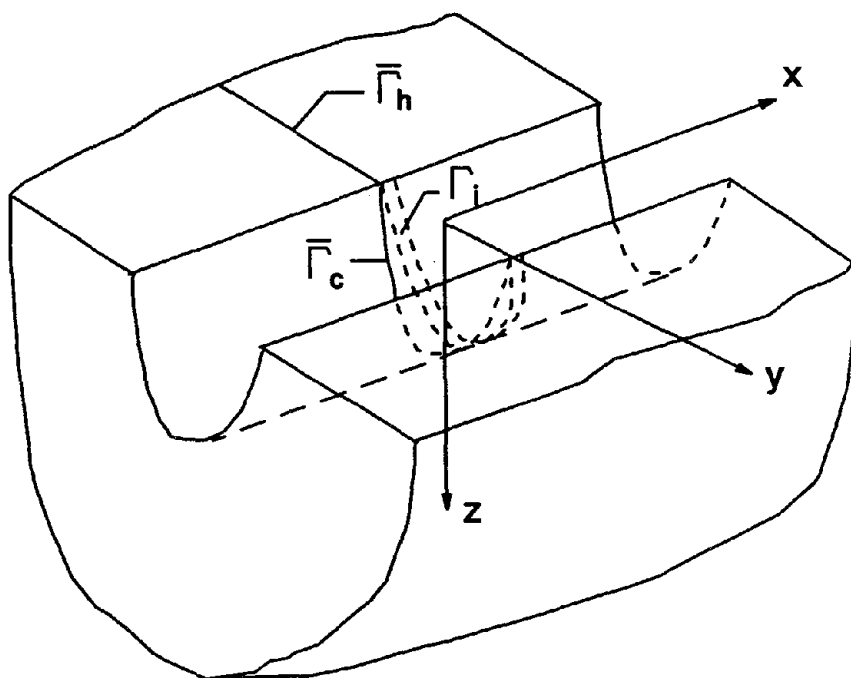


Fig.1 Infinitely-long canyon of arbitrary but uniform cross-section; $\bar{\Gamma}_c$ is the cross-section of the canyon at $x = 0$; Γ_i is the interface between the dam and foundation rock.

The frequency-dependent impedance matrix $[S_f(\omega)]$ is function of the material properties of the foundation rock and the geometry of both the canyon and the dam-foundation rock interface. For the system considered, the material properties of the half-space medium are characterized by the complex P and S wave velocities $c_p = \bar{c}_p(1 + i\eta_p)^{1/2}$ and $c_s = \bar{c}_s(1 + i\eta_s)^{1/2}$. The terms η_p and η_s represent the constant hysteretic damping factors for P and S waves respectively; and \bar{c}_p and \bar{c}_s denote the P and S wave velocities if the medium were undamped. Similarly, the Rayleigh wave velocity is given by $c_r = \bar{c}_r(1 + i\eta_r)^{1/2}$ where \bar{c}_r is the Rayleigh wave velocity without damping and η_r is the corresponding hysteretic damping factor. Both \bar{c}_r and η_r are related to \bar{c}_p , \bar{c}_s , η_p and η_s .

FOURIER REPRESENTATION OF TRACTIONS AND DISPLACEMENTS

Because the system geometry is uniform along the length of the canyon, it is useful to express tractions and displacements through their Fourier integral representations. The tractions are prescribed over the dam-foundation rock interface, which is discretized into two-dimensional curved boundary elements compatible with the finite element discretization at the base of the dam. The prescribed traction on the j th boundary element is $\{t(\bar{x})\}_j e^{i\omega t}$, where $\bar{x} = (x, y, z)$ is an arbitrary point within the element, and the vector $\{t(\bar{x})\}_j$ contains the x , y and z components of tractions. The traction vector is expressed through its Fourier integral representation:

$$\{t(\bar{x})\}_j = \int_{-\infty}^{\infty} \{\bar{t}(\bar{x}_o, k)\}_j e^{-ikx} dk \quad (2)$$

where $\bar{x}_o = (0, y, z)$ and $\{\bar{t}(\bar{x}_o, k)\}_j$ is the Fourier transform of $\{t(\bar{x})\}_j$ with respect to x

$$\{\bar{t}(\bar{x}_o, k)\}_j = \frac{1}{2\pi} \int_{-\infty}^{\infty} \{t(\bar{x})\}_j e^{ikx} dx \quad (3)$$

The Fourier transform parameter k can be interpreted physically as a wavenumber since $\{\bar{t}(\bar{x}_o, k)\}_j e^{-ikx} e^{i\omega t}$ represents tractions associated with a wave travelling along the x -axis. Thus equation (2) suggests that the prescribed tractions can be considered as a superposition over all wavenumbers of tractions associated with waves travelling

in opposite directions along the x -axis. In particular, a negative value of k indicates waves travelling in the negative x -direction and a positive k represents waves moving in the positive x -direction. The superposition of these waves, which travel at speed $c = \omega/|k|$, results in the prescribed tractions in the form of a standing wave.

The prescribed tractions on the dam-foundation rock interface are next expressed in terms of traction distributions over individual boundary elements. Along the line parallel to the x -axis passing through \bar{x}_o , the traction distribution is given by the superposition of tractions associated with each of the elements intersected by the line:

$$\{t(\bar{x})\} = \int_{-\infty}^{\infty} \{\bar{t}(\bar{x}_o, k)\} e^{-ikx} dk \quad (4)$$

where

$$\{\bar{t}(\bar{x}_o, k)\} = \sum_j \{\bar{t}(\bar{x}_o, k)\}_j \quad (5)$$

The tractions are obviously zero at all locations on the canyon surface and half-space surface that are outside the dam-foundation rock interface.

The steady-state displacements $\{u(\bar{x})\}e^{i\omega t}$ resulting from the prescribed tractions with harmonic time-variation at frequency ω can also be expressed as a superposition of displacements associated with travelling waves. Thus, the vector $\{u(\bar{x})\}$ containing the three components of displacements at the canyon boundary Γ_c , or the half-space surface Γ_h , resulting from the prescribed tractions (equation 4) is given by

$$\{u(\bar{x})\} = \int_{-\infty}^{\infty} \{\bar{u}(\bar{x}_o, k)\} e^{-ikx} dk \quad \bar{x} \in \Gamma_h \cup \Gamma_c \quad (6)$$

where $\{\bar{u}(\bar{x}_o, k)\}$ is the Fourier transform of the displacement vector given by

$$\{\bar{u}(\bar{x}_o, k)\} = \frac{1}{2\pi} \int_{-\infty}^{\infty} \{u(\bar{x})\} e^{ikx} dx \quad (7)$$

For any particular wavenumber k , $\{\bar{u}(\bar{x}_o, k)\}e^{-ikx}$ represents a wave with displacement pattern $\{\bar{u}(\bar{x}_o, k)\}$ travelling in the x -direction with speed $c = \omega/|k|$. As mentioned before, a positive value of k indicates a wave travelling in the positive x -direction,

and vice-versa. In addition, the dependence of the displacements and tractions on the frequency ω is implied throughout.

We have now expressed the prescribed tractions and unknown displacements in terms of their Fourier integral representation which implies superposition over all wavenumbers (equations 4 and 6). Considering one wavenumber at a time, the prescribed boundary tractions are $\{\bar{t}(\bar{x}_o, k)\}e^{-ikx}e^{i\omega t}$ and the unknown displacements are $\{\bar{u}(\bar{x}_o, k)\}e^{-ikx}e^{i\omega t}$, where ω is the excitation frequency and k is the wavenumber. The problem to be solved for a particular wavenumber involves determining the displacements $\{\bar{u}(\bar{x}_o, k)\}$ at the curve $\bar{\Gamma}_c$, where $x = 0$, due to the travelling wave associated with tractions $\{\bar{t}(\bar{x}_o, k)\}$ obtained from equation (5) at $x = 0$. The resulting displacements for all wavenumbers are superposed to obtain the displacements at any location \bar{x} on the boundary (equation 6); in particular, the displacements at the dam-foundation rock interface, Γ_i , can be determined.

BOUNDARY INTEGRAL FORMULATION

The boundary integral equation for the system considered, consisting of an infinitely long canyon of uniform cross-section, can be obtained from the reciprocal theorem and can be expressed as (Part I)

$$\int_{\bar{\Gamma}_c \cup \bar{\Gamma}_h \cup \bar{\Gamma}_s} \int_{-\infty}^{\infty} \left([\bar{F}^n(\bar{x}, \bar{x}_{os})]^T \{u(\bar{x})\} - [G^*(\bar{x}, \bar{x}_{os})]^T \{t(\bar{x})\} \right) dx d\Gamma = 0 \quad (8)$$

where $\{t(\bar{x})\}$ is the prescribed traction at \bar{x} on the boundary with its normal denoted by n , $\{u(\bar{x})\}$ is the resulting unknown displacement vector, and $[\bar{F}^n(\bar{x}, \bar{x}_{os})]$ and $[G^*(\bar{x}, \bar{x}_{os})]$ are 3×3 matrices of Green's functions for a full-space. The first, second and third columns of these matrices correspond to the traction and displacement vectors at \bar{x} due to a unit point load applied in the x , y and z directions, respectively, at a source point $\bar{x}_{os} = (0, y_s, z_s)$ on $\bar{\Gamma}_c$ or $\bar{\Gamma}_h$, the intersection line of the system boundary and the plane $x = 0$. The integration is over the entire system boundary, consisting of the surface of the half-space and the boundary of the canyon, modified slightly to avoid the singularity in the Green's functions at the point of load application (Figure 2).

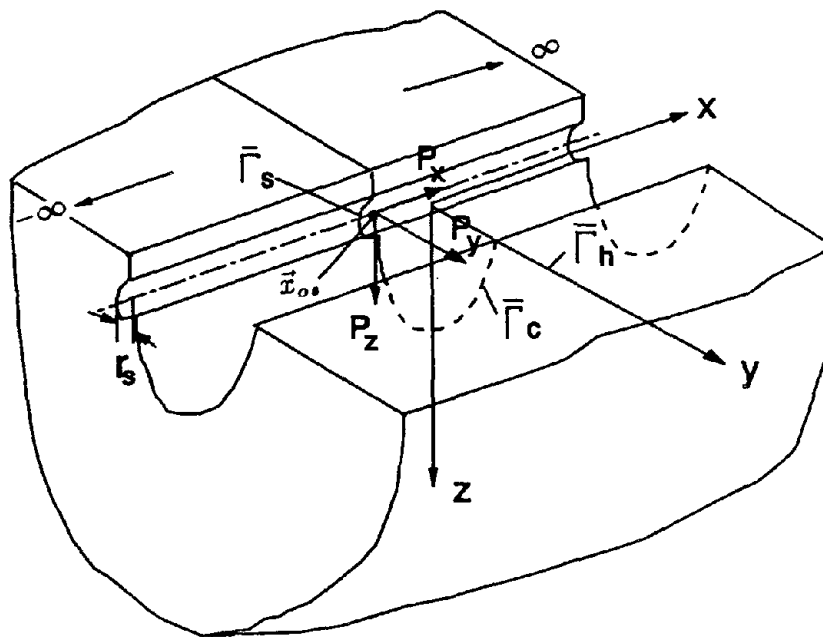


Fig.2 Definition of boundaries and source point; $\bar{\Gamma}_c$ is the cross-section of the canyon at $x=0$, $\bar{\Gamma}_h$ is the $x=0$ line on the surface of the half-space, and $\bar{\Gamma}_s$ is the small contour of radius r , around the source point.

Expressions for $[\bar{F}^*(\bar{x}, \bar{x}_{os})]$ and $[G^*(\bar{x}, \bar{x}_{os})]$ are given in Appendix B of Part I. For each source point, \bar{x}_{os} , equation (8) provides three scalar equations in the unknown displacements $\{u(\bar{x})\}$.

Substituting equations (4) and (6) into equation (8) and interchanging the order of integration lead to

$$\int_{-\infty}^{\infty} \int_{\bar{\Gamma}_c \cup \bar{\Gamma}_h \cup \bar{\Gamma}_s} \int_{-\infty}^{\infty} \left([\bar{F}^*(\bar{x}, \bar{x}_{os})]^T \{\bar{u}(\bar{x}_o, k)\} - [G^*(\bar{x}, \bar{x}_{os})]^T \{\bar{t}(\bar{x}_o, k)\} \right) e^{-ikx} dx d\Gamma dk = 0 \quad (9)$$

After analytically evaluating the integral along the x -axis, equation (9) becomes

$$\int_{-\infty}^{\infty} \int_{\bar{\Gamma}_c \cup \bar{\Gamma}_h \cup \bar{\Gamma}_s} \left([\bar{F}(\bar{x}_o, \bar{x}_{os}, k)]^T \{\bar{u}(\bar{x}_o, k)\} - [G(\bar{x}_o, \bar{x}_{os}, k)]^T \{\bar{t}(\bar{x}_o, k)\} \right) d\Gamma dk = 0 \quad (10)$$

where

$$[G(\bar{x}_o, \bar{x}_{os}, k)] = \int_{-\infty}^{\infty} [G^*(\bar{x}, \bar{x}_{os})] e^{-ikx} dx \quad (11a)$$

$$[\bar{F}(\bar{x}_o, \bar{x}_{os}, k)] = \int_{-\infty}^{\infty} [\bar{F}^*(\bar{x}, \bar{x}_{os})] e^{-ikx} dx \quad (11b)$$

Expressions for the transformed Green's functions, $[G]$ and $[F]$, are given in Appendix C of Part I.

As mentioned earlier, the displacements resulting from prescribed tractions $\{\bar{t}(\bar{x}_o, k)\} e^{-ikx} e^{i\omega t}$ have the form $\{\bar{u}(\bar{x}_o, k)\} e^{-ikx} e^{i\omega t}$, i.e., $\{\bar{t}(\bar{x}_o, k)\}$ and $\{\bar{u}(\bar{x}_o, k)\}$ correspond to the same wave travelling at speed $c = \omega/k$, where k is the wavenumber. Thus, equation (10) implies that the following equation must be satisfied for each k

$$\int_{\bar{\Gamma}_c \cup \bar{\Gamma}_h \cup \bar{\Gamma}_s} \left([\bar{F}(\bar{x}_o, \bar{x}_{os}, k)]^T \{\bar{u}(\bar{x}_o, k)\} - [G(\bar{x}_o, \bar{x}_{os}, k)]^T \{\bar{t}(\bar{x}_o, k)\} \right) d\Gamma = 0 \quad (12)$$

The final step is to make the radius r_s of the small arc $\bar{\Gamma}_s$ around the source point \bar{x}_{os} approach zero. Following the steps in [32], the final form of the boundary integral equation (12) can be expressed as

$$[C(\bar{x}_{os})] \{\bar{u}(\bar{x}_{os}, k)\} + \int_{\bar{\Gamma}_c \cup \bar{\Gamma}_h} [\bar{F}(\bar{x}_o, \bar{x}_{os}, k)]^T \{\bar{u}(\bar{x}_o, k)\} d\Gamma =$$

$$\int_{\Gamma_c \cup \Gamma_h} [G(\vec{x}_o, \vec{x}_{os}, k)]^T \{\bar{t}(\vec{x}_o, k)\} d\Gamma \quad (13)$$

where

$$[C(\vec{x}_{os})] = \lim_{r_s \rightarrow 0} \int_{\Gamma_s} [F(\vec{x}_o, \vec{x}_{os}, k)]^T d\Gamma \quad (14)$$

The general expression for the 3×3 matrix $[C(\vec{x}_{os})]$ is given in Appendix C of Part I. It is independent of the wavenumber k and depends only on the geometry of the boundary at the source point \vec{x}_{os} . If the boundary is smooth, i.e., it has a unique tangent, $C_{ij}(\vec{x}_{os}) = \delta_{ij}/2$.

Equation (13) is the exact formulation for the problem, requiring solution of the displacements $\{\bar{u}(\vec{x}_o, k)\}$ along $\bar{\Gamma}_c$ and $\bar{\Gamma}_h$, i.e. $x = 0$, due to tractions $\{\bar{t}(\vec{x}_o, k)\}e^{-ikx}$ associated with a single wave travelling at speed $c = \omega/k$. In this equation, $\{\bar{t}(\vec{x}_o, k)\}$ is known from equation (5), the transformed Green's function matrices $[G]$ and $[F]$ are known from equation (11) and Appendix C of Part I, whereas the unknowns are the displacements $\{\bar{u}(\vec{x}_o, k)\}$ at both the source point \vec{x}_{os} and the rest of the boundary $\bar{\Gamma}_c \cup \bar{\Gamma}_h$. Thus, by taking advantage of the uniform geometry of the system along the x -direction, the displacements associated with a single travelling wave can be determined by solving a "two-dimensional" boundary integral problem (equation 13) in which the remaining integration is only along the curve $\bar{\Gamma}_c \cup \bar{\Gamma}_h$.

Solution of an infinite number of such two-dimensional problems, each corresponding to a particular wavenumber, would lead to the displacements $\{\bar{u}(\vec{x}_o, k)\}$ for all wavenumbers, which are combined in accordance with equation (6) to determine the displacements $\{u(\vec{x})\}$ at any location on the boundary, and in particular at the dam-foundation rock interface. In practice, of course, the infinite integration range in equation (6) would be replaced by a finite range and the truncated integral would be numerically evaluated from results at an appropriate set of wavenumbers.

BOUNDARY ELEMENT FORMULATION

Discretization

In its present form, equation (13) cannot be solved analytically for the displace-

ments $\{\bar{u}(\bar{x}_o, k)\}$, even for the simplest canyon geometry. Therefore, the integration domain $\bar{\Gamma}_c \cup \bar{\Gamma}_h$ is discretized into M one-dimensional line elements (Figure 3). Along the half-space surface $\bar{\Gamma}_h$, the discretization obviously extends to only a finite distance L_y , which should be large enough to provide accurate solutions. The number of nodes in each element depends on the element type; in this study, two node elements are used with linear interpolation functions given by $N_1(\zeta) = 0.5(1 - \zeta)$ and $N_2(\zeta) = 0.5(1 + \zeta)$ where ζ varies from -1 to 1 . Thus the discretized system with M elements has $M_n = M + 1$ nodes.

The variation of the unknown displacements $\{\bar{u}(\bar{x}_o, k)\}$ over the j th element on $\bar{\Gamma}_c \cup \bar{\Gamma}_h$ can be expressed in terms of nodal displacements

$$\{\bar{u}(\bar{x}_o, k)\}_j = [N(\zeta)]\{\bar{U}\}_j \quad (15)$$

where $[N(\zeta)]$ is a 3×6 matrix consisting of interpolation functions

$$[N(\zeta)] = \begin{pmatrix} N_1 & 0 & 0 & N_2 & 0 & 0 \\ 0 & N_1 & 0 & 0 & N_2 & 0 \\ 0 & 0 & N_1 & 0 & 0 & N_2 \end{pmatrix} \quad (16)$$

and $\{\bar{U}\}_j$ is the vector of displacements at the two nodes — j and $j + 1$ — of the element

$$\{\bar{U}\}_j = \{\bar{U}_{xj}, \bar{U}_{yj}, \bar{U}_{zj}, \bar{U}_{x(j+1)}, \bar{U}_{y(j+1)}, \bar{U}_{z(j+1)}\}_j^T$$

As mentioned before, the dam-foundation rock interface Γ_i is discretized into two-dimensional curved elements compatible with the finite element discretization at the base of the dam. The total number of nodes on Γ_i is denoted by M_i . On each element, the prescribed tractions can be expressed in terms of nodal tractions; for the j th element

$$\{t(\bar{x})\}_j = [h(\bar{x})]_j \{T\}_j \quad (17)$$

where the matrix $[h(\bar{x})]_j$ consists of two-dimensional interpolation functions and $\{T\}_j$ is the vector of tractions at all the nodal points of the element. If the j th element has \bar{M} nodes, $[h(\bar{x})]_j$ is of size $3 \times 3\bar{M}$ and $\{T\}_j$ is of dimension $3\bar{M}$. As a result, the

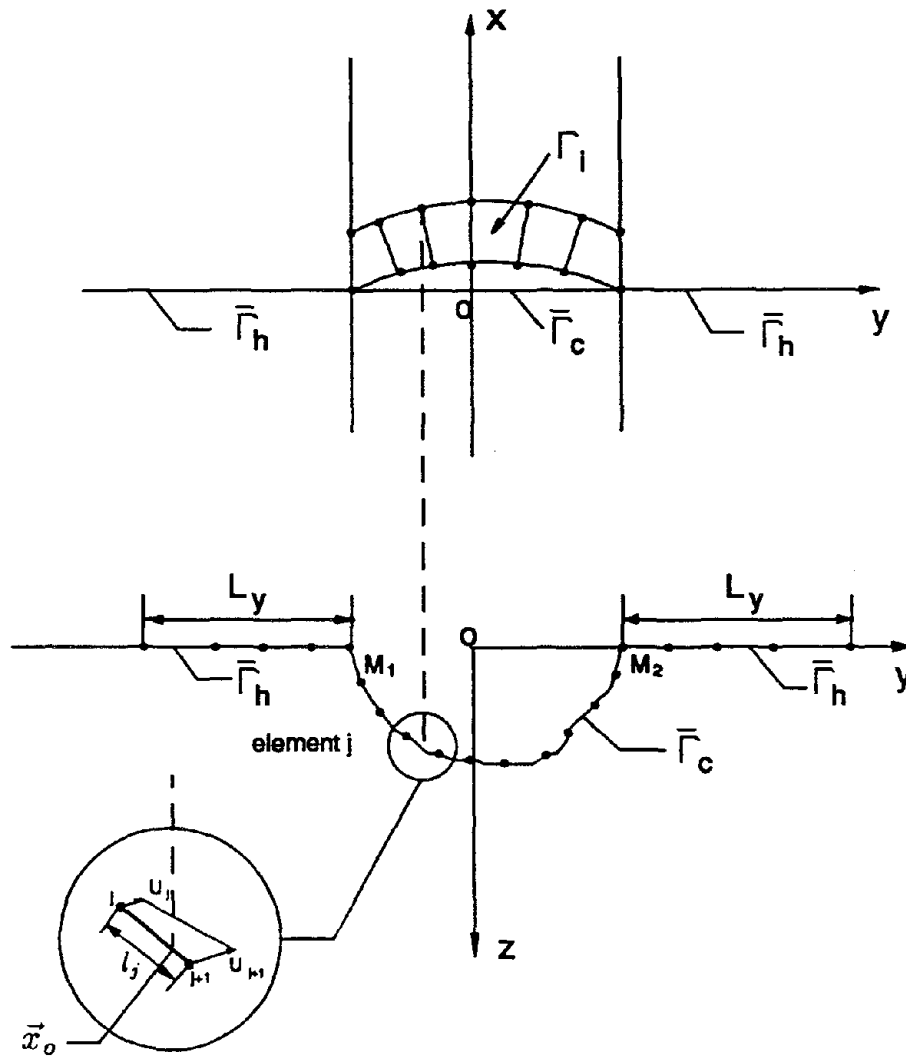


Fig.3 Boundary element discretization.

Fourier transforms of the prescribed tractions (equation 3) in the j th element on Γ_i can be represented by

$$\{\bar{t}(\bar{x}_o, k)\}_j = [\bar{h}(\bar{x}_o, k)]_j \{T\}_j \quad (18)$$

where $[\bar{h}(\bar{x}_o, k)]_j$ is the Fourier transform of the two-dimensional interpolation functions with respect to x

$$[\bar{h}(\bar{x}_o, k)]_j = \frac{1}{2\pi} \int_{-\infty}^{\infty} [h(\bar{x})]_j e^{ikx} dx \quad (19)$$

Expressions of $[\bar{h}(\bar{x}_o, k)]_j$ for 4, 6 and 8 node elements are given in Appendix A.

Combining the contributions of all boundary elements on Γ_i intersected by the line $\bar{x} = \bar{x}_o$ (equation 5), the Fourier transform of the traction distribution along this line is given by

$$\{\bar{t}(\bar{x}_o, k)\} = \sum_{\substack{j \\ \text{assemble}}} [\bar{h}(\bar{x}_o, k)]_j \{T\}_j \quad (20)$$

which, after assembly, can be expressed in matrix form as

$$\{\bar{t}(\bar{x}_o, k)\} = [\bar{H}(\bar{x}_o, k)] \{T\}_{\bar{x}_o} \quad (21)$$

In equation (21), $\{T\}_{\bar{x}_o}$ contains the tractions at all the nodal points on the elements intersected by the line $\bar{x} = \bar{x}_o$.

Thus, after discretizing $\bar{\Gamma}_c \cup \bar{\Gamma}_h$ into one-dimensional line elements and Γ_i into two-dimensional elements, the Fourier transforms of the unknown displacements, $\{\bar{u}(\bar{x}_o, k)\}$, have been expressed in terms of nodal displacements (equation 15) and, $\{\bar{t}(\bar{x}_o, k)\}$, the Fourier transforms of the prescribed tractions, have been represented through nodal tractions $\{T\}$ (equation 21).

Boundary Element Equations

The next step is to replace the boundary integrations in equation (13) by the summation of integrals over all the M elements

$$[C(\bar{x}_{os})] \{\bar{u}(\bar{x}_{os}, k)\} + \sum_{j=1}^M \int_{\Gamma_j} [F(\bar{x}_o, \bar{x}_{os}, k)]_j^T \{\bar{u}(\bar{x}_o, k)\}_j d\Gamma$$

$$= \sum_{j=M_1}^{M_2} \int_{\bar{\Gamma}_j} [G(\bar{x}_o, \bar{x}_{os}, k)]_j^T \{\bar{t}(\bar{x}_o, k)\}_j d\Gamma \quad (22)$$

where $\bar{\Gamma}_j$ is the extent of the j th element. The summation on the right side only covers the elements on the canyon boundary, $\bar{\Gamma}_c$, since the tractions are zero on the half-space surface, $\bar{\Gamma}_h$. By expressing the displacements and the tractions in terms of nodal displacements and tractions through equations (15) and (21) and changing the integration variable to ζ , the contributions from the j th element in equation (22) become

$$\int_{\bar{\Gamma}_j} [\bar{F}^n(\bar{x}_o, \bar{x}_{os}, k)]_j^T \{\bar{u}(\bar{x}_o, k)\}_j d\Gamma = \frac{1}{2} l_j \int_{-1}^1 [\bar{F}^n(\zeta, \bar{x}_{os}, k)]_j^T [N(\zeta)] d\zeta \{\bar{U}\}_j \quad (23a)$$

$$\int_{\bar{\Gamma}_j} [G(\bar{x}_o, \bar{x}_{os}, k)]_j^T \{\bar{t}(\bar{x}_o, k)\}_j d\Gamma = \frac{1}{2} l_j \int_{-1}^1 [G(\zeta, \bar{x}_{os}, k)]_j^T [\bar{H}(\zeta, k)]_j \{T\}_\zeta d\zeta \quad (23b)$$

where l_j is the length of the j th element. Substituting these equalities, equation (22) can be expressed in matrix form

$$[C(\bar{x}_{os})] \{\bar{u}(\bar{x}_{os}, k)\} + [\bar{A}(\bar{x}_{os}, k)] \{\bar{U}\} = [\bar{B}(\bar{x}_{os}, k)] \{T\} \quad (24)$$

Equation (24) represents three equations associated with each source point $\bar{x}_{os} = (0, y_s, z_s)$ and each wavenumber k , where the 3×3 matrix $[C(\bar{x}_{os})]$ is given by equation (14), the 3×1 vector $\{\bar{u}(\bar{x}_{os}, k)\}$ represents the unknown displacements at the source point, $\{\bar{U}\}$ is a $3M_n \times 1$ column vector of unknown nodal displacements (3 displacement components at each of the M_n nodes on the boundary $\bar{\Gamma}_c \cup \bar{\Gamma}_h$), $\{T\}$ is a $3M_i \times 1$ column vector of nodal tractions (3 components at each of the M_i nodes on Γ_i), $[\bar{A}(\bar{x}_{os}, k)]$ is a $3 \times 3M_n$ matrix assembled from the integrals of the products of the transformed traction Green's functions and element interpolation functions

$$[\bar{A}(\bar{x}_{os}, k)] = \frac{1}{2} \sum_{\substack{j=1 \\ \text{assemble}}}^M l_j \int_{-1}^1 [\bar{F}^n(\zeta, \bar{x}_{os}, k)]_j^T [N(\zeta)] d\zeta \quad (25)$$

and $[\bar{B}(\bar{x}_{os}, k)]$ is a $3 \times 3M_i$ matrix assembled from the integrals of the products of the transformed displacement Green's functions and Fourier transform of the two-

dimensional interpolation functions (equation 21)

$$[\tilde{B}(\vec{x}_{os}, k)] = \frac{1}{2} \sum_{\substack{j=M_1 \\ \text{assemble}}}^{M_2} l_j \int_{-1}^1 [G(\zeta, \vec{x}_{os}, k)]_j^T [\tilde{H}(\zeta, k)]_j d\zeta \quad (26)$$

Both $[\tilde{A}(\vec{x}_{os}, k)]$ and $[\tilde{B}(\vec{x}_{os}, k)]$ are obtained by appropriately assembling the contribution of the various elements, a process similar to the stiffness matrix assembly in the direct stiffness method. The construction of both of these matrices for a small system is illustrated in Figure 4.

Equation (24) is a discrete form of equation (13) obtained by introducing two approximations: (1) interpolation of the unknown displacements over each element on $\bar{\Gamma}_c \cup \bar{\Gamma}_h$ in terms of nodal displacements (in this particular formulation, the interpolation functions were chosen to be linear); and (2) truncation of the integration on $\bar{\Gamma}_h$ to a finite distance.

Formation of System Matrices

Associated with the source point $\vec{x}_{os} = (0, y_s, z_s)$, equation (24) represents 3 linear algebraic equations in $3M_n$ unknown displacements. Clearly, a total of $3M_n$ equations are needed to determine the unknown displacements. These equations can be obtained by successively choosing the source point at each of the nodes of the discretized boundary $\bar{\Gamma}_c \cup \bar{\Gamma}_h$. When the source point coincides with the i th node, equation (24) becomes

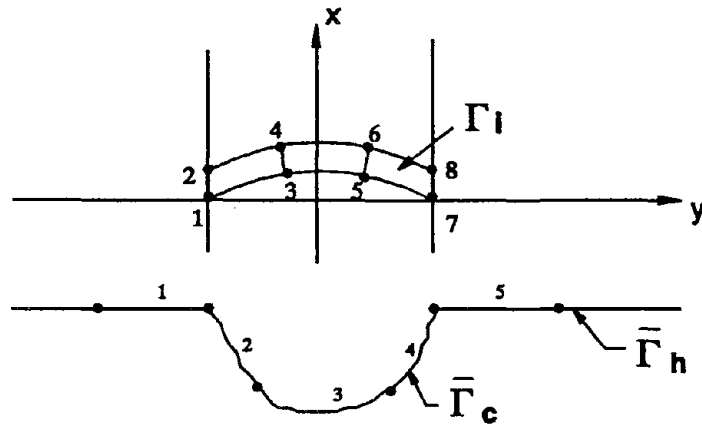
$$[C(\vec{x}_i)]\{\bar{u}(\vec{x}_i, k)\} + [\tilde{A}(\vec{x}_i, k)]\{\bar{U}\} = [\tilde{B}(\vec{x}_i, k)]\{T\} \quad (27)$$

By varying $i = 1, 2, \dots, M_n$ and assembling the resulting equations, a system of $3M_n$ linear equations can be obtained

$$[A(k)]\{\bar{U}\} = [B(k)]\{T\} \quad (28)$$

where $[A(k)]$ is a square matrix of order $3M_n$, given by

$$[A(k)] = \begin{pmatrix} [C(\vec{x}_1)] & & & \\ & \cdot & & \\ & & \cdot & \\ & & & [C(\vec{x}_{M_n})] \end{pmatrix} + \begin{pmatrix} [\tilde{A}(\vec{x}_1, k)] \\ \cdot \\ \cdot \\ [\tilde{A}(\vec{x}_{M_n}, k)] \end{pmatrix} \quad (29)$$



$$\begin{aligned}
 & [C(\vec{x}_{os})] \{ \bar{u}(\vec{x}_{os}, k) \} + \left\{ \begin{array}{l} \text{Matrix 1} \\ \text{Matrix 2} \\ \text{Matrix 3} \\ \text{Matrix 4} \\ \text{Matrix 5} \end{array} \right\} \{ \bar{U} \} \\
 & \quad \leftarrow \text{contribution of element 3} = [\tilde{A}(\vec{x}_{os}, k)]_3 \\
 & = \left\{ \begin{array}{l} \text{Matrix 6} \\ \text{Matrix 7} \\ \text{Matrix 8} \end{array} \right\} \{ T \} \\
 & \quad \leftarrow \text{contribution of element 3} = [\tilde{B}(\vec{x}_{os}, k)]_3 \\
 & \quad \downarrow [\tilde{A}(\vec{x}_{os}, k)] \\
 & [C(\vec{x}_{os})] \{ \bar{u}(\vec{x}_{os}, k) \} + \left\{ \begin{array}{l} \text{Matrix 9} \end{array} \right\} \{ \bar{U} \} \\
 & = \left\{ \begin{array}{l} \text{Matrix 10} \end{array} \right\} \{ T \} \\
 & \quad \uparrow [\tilde{B}(\vec{x}_{os}, k)]
 \end{aligned}$$

Fig.4 Assembly of Matrices.

and $[B(k)]$ is a $3M_n \times 3M_i$ matrix given by

$$[B(k)] = \begin{pmatrix} [\tilde{B}(\bar{x}_1, k)] \\ \vdots \\ [\tilde{B}(\bar{x}_{M_n}, k)] \end{pmatrix} \quad (30)$$

The coefficient matrix $[A(k)]$ is fully populated and unsymmetric, which is of typical of direct boundary element method equations.

Evaluation of Displacements

Solution of the equation (28) leads to the displacements $\{\bar{U}\}$ at the M_n nodes on the boundary $\bar{\Gamma}_c \cup \bar{\Gamma}_h$ in terms of the nodal tractions $\{T\}$ for a particular wavenumber k

$$\{\bar{U}\} = [A(k)]^{-1}[B(k)]\{T\} \quad (31)$$

Once the nodal displacements are determined, the displacement variation $\{\bar{u}(\bar{x}_o, k)\}$ over each finite element on $\bar{\Gamma}_c$ can be obtained from equation (15).

IMPEDANCE MATRIX

After the displacements $\{\bar{u}(\bar{x}_o, k)\}$ at the $y-z$ plane ($x = 0$) of the canyon boundary, $\bar{\Gamma}_c$, and the half-space surface, $\bar{\Gamma}_h$, are obtained for various values of the wavenumber, k , the displacements at any other location on these boundaries can be obtained from equation (6). In particular, the displacements at the dam-foundation rock interface, Γ_i , can be determined. The indefinite integral of equation (6) is truncated at a finite range $(-K, K)$ and it is evaluated from the displacements obtained for a discrete set of wavenumbers k_q using an appropriate integration scheme:

$$\{u(\bar{x})\} = \sum_q W_q \{\bar{u}(\bar{x}_o, k_q)\} e^{-ik_q x} \quad (32)$$

where W_q are weighting coefficients associated with the numerical integration scheme, and k_q is the q th sampling point in the wavenumber domain k . Guidelines for selecting sampling points in the wavenumber domain will be presented later.

Thus, the vector of displacements at the j th node on Γ_i , defined by the coordinates $\vec{x}_j = (x_j, y_j, z_j)$, due to the prescribed tractions is given by

$$\{\bar{r}\}_j = \sum_q W_q \{\bar{u}(\vec{x}_{oj}, k_q)\} e^{-ik_q x_j} \quad (33)$$

where $\vec{x}_{oj} = (0, y_j, z_j)$, and $\{\bar{u}(\vec{x}_{oj}, k_q)\}$ is obtained from the solution of equation (31) for the nodal displacements and the displacement interpolation relation (15). If \vec{x}_{oj} falls in the m th element (Figure 3) in the plane $x = 0$ with ζ_j as the corresponding natural coordinate, $\{\bar{u}(\vec{x}_{oj}, k_q)\}$ is given by (see equation 15)

$$\{\bar{u}(\vec{x}_{oj}, k_q)\} = N_1(\zeta_j)\{\bar{U}\}_m + N_2(\zeta_j)\{\bar{U}\}_{m+1} \quad (34)$$

where $N_1(\zeta_j)$ and $N_2(\zeta_j)$ are the linear interpolation functions given in the previous section, and $\{\bar{U}\}_m$ and $\{\bar{U}\}_{m+1}$ are the 3×1 vectors of displacements at the m th and $(m+1)$ th nodes on $\bar{\Gamma}_c \cup \bar{\Gamma}_h$ associated with the q th sampling point k_q . Since the nodal displacements are linear combinations of the nodal tractions (equation 31), $\{\bar{u}(\vec{x}_{oj}, k_q)\}$ in equation (34) can also be expressed as linear combinations of $\{T\}$, leading to

$$\{\bar{u}(\vec{x}_{oj}, k_q)\} = [E(\vec{x}_{oj}, k_q)]\{T\} \quad (35)$$

where $[E(\vec{x}_{oj}, k_q)]$ is a $3 \times 3M_i$ matrix relating the Fourier transform of the displacements along the line $\vec{x} = \vec{x}_{oj}$ to the nodal tractions. Thus from equations (33) and (35), the vector of displacements at the j th node on Γ_i becomes

$$\{\bar{r}\}_j = [\tilde{f}_j]\{T\} \quad (36)$$

where

$$[\tilde{f}_j] = \sum_q W_q [E(\vec{x}_{oj}, k_q)] e^{-ik_q x_j} \quad (37)$$

Combining equations (36) for each of the M_i nodes on Γ_i leads to

$$\{\bar{r}\} = [f]\{T\} \quad (38)$$

where $\{\bar{r}\}$ is a $3M_i \times 1$ vector of nodal displacements (3 components at each of the M_i nodes) and $[f]$ is a square matrix of order $3M_i$ given by

$$[f] = \begin{pmatrix} [\bar{f}_1] \\ \vdots \\ [\bar{f}_{M_i}] \end{pmatrix} \quad (39)$$

The matrix $[f]$ in the above equation is the frequency-dependent flexibility influence matrix which relates the displacements at the DOF on the dam-foundation rock interface Γ_i to the corresponding nodal tractions $\{T\}$.

As mentioned earlier, the impedance matrix $[S_f(\omega)]$ for the foundation rock relates nodal forces to nodal displacements at the discretized dam-foundation rock interface. This matrix is obtained from equation (38) by transforming distributed tractions to nodal forces:

$$\{\bar{R}\} = [\Phi]\{T\} \quad (40)$$

where $\{\bar{R}\}$ is a $3M_i \times 1$ vector of nodal forces (3 components at each of the M_i nodes on Γ_i), and $[\Phi]$ is a square matrix of order $3M_i$ assembled from the products of the two-dimensional interpolation functions

$$[\Phi] = \int_{\Gamma_i} [h(\bar{x})]^T [h(\bar{x})] d\Gamma \quad (41)$$

Combining equations (38) and (40) gives

$$\{\bar{R}(\omega)\} = [\Phi][f(\omega)]^{-1}\{\bar{r}(\omega)\} \quad (42)$$

wherein it is recognized that the nodal forces $\{\bar{R}(\omega)\}$, the nodal displacements $\{\bar{r}(\omega)\}$ and the flexibility influence matrix $[f(\omega)]$ are frequency-dependent. Thus, comparing equations (1) and (42) leads to the $3M_i \times 3M_i$ impedance matrix

$$[\hat{S}(\omega)] = [\Phi][f(\omega)]^{-1} \quad (43)$$

The impedance matrix determined from equation (43) will not be exactly symmetric due to the approximations inherent in the boundary element procedures; it is

nearly symmetric, however. By minimizing the differences in the unsymmetric off-diagonal terms in a least square sense [16], a symmetric impedance matrix is given by

$$[S_f(\omega)] = \frac{1}{2}([\hat{S}(\omega)] + [\hat{S}(\omega)]^T) \quad (44)$$

For a rigid foundation on the surface of the canyon, the nodal displacements at the foundation-rock interface can be expressed as

$$\{\bar{r}(\omega)\} = [\alpha]\{\bar{r}_o(\omega)\} \quad (45)$$

where $\{\bar{r}_o(\omega)\}$ is the 6×1 vector containing the six rigid-body DOFs of the foundation and $[\alpha]$ is a $3M_i \times 6$ matrix relating the nodal displacements on Γ_i with $\{\bar{r}_o(\omega)\}$. Thus the 6×6 impedance matrix for the rigid foundation is given by

$$[S_r(\omega)] = [\alpha]^T[S_f(\omega)][\alpha] \quad (46)$$

SUMMARY OF PROCEDURE

The boundary element procedure developed in the preceding sections to determine the impedance matrix, or dynamic stiffness matrix, corresponding to an excitation frequency ω , for the foundation rock region, defined at the DOF of the dam-foundation rock interface, may be summarized as follows:

1. Discretize Γ_i , the dam-foundation rock interface, into two-dimensional surface elements, select interpolation functions $[h(\vec{x})]$, and determine their Fourier transforms (equation 19). The expressions of these Fourier transforms for 4, 6 and 8 node surface elements are available in Appendix A.
2. Discretize $\bar{\Gamma}_c$, the canyon boundary at $x = 0$, and $\bar{\Gamma}_h$, the half-space surface at $x = 0$, into M line elements covering a range L_y on $\bar{\Gamma}_h$ (Figure 3). If linear interpolation functions are selected for each element, the discretized system contains $M_n = M + 1$ nodes.
3. Choose an appropriate integration scheme and its associated weighting coefficients W_q and a discrete set of wavenumber sampling points k_q (equation 32). Guidelines

for selection of k_q and the truncated integration range $(-K,K)$ are presented in a later section. For each $k = k_q$, repeat steps 4 to 7 to express the nodal displacements $\{\bar{U}\}$ on $\bar{\Gamma}_c \cup \bar{\Gamma}_h$ in terms of nodal tractions $\{T\}$ on Γ_i (equation 31).

4. Establish equation (27) which includes three linear algebraic equations associated with \bar{x}_i , the i th node on $\bar{\Gamma}_c \cup \bar{\Gamma}_h$, in $3M_n$ unknowns (3 displacement components at each of the M_n nodes) by the following steps:
 - (a) Compute the elements of the 3×3 matrix $[C(\bar{x}_i)]$ which depend on the geometry of the boundary at the i th node; see Appendix C of Part I. These elements are given by $C_{jk}(\bar{x}_i) = \delta_{jk}/2$ if the boundary is smooth, i.e., it has a unique tangent at \bar{x}_i .
 - (b) Compute the $3 \times 3M_n$ matrix $[\tilde{A}(\bar{x}_i, k_q)]$ from equation (25) by assembling the contributions of all the M elements, as described in Figure 4. Element contributions are determined from the integrals of the transformed traction Green's functions, $[\tilde{F}]$, (equation 11b) and element interpolation functions. Analytical expressions for $[\tilde{F}]$ are available in Appendix C of Part I.
 - (c) Compute the $3 \times 3M_i$ matrix $[\tilde{B}(\bar{x}_i, k_q)]$ from equation (26) by assembling the contributions from all the elements on $\bar{\Gamma}_c$, as described in Figure 4. The line element contributions are determined from equation (26) wherein the transformed displacement Green's functions, $[G]$, are computed from equation (11a) and the assembled Fourier transforms of the two-dimensional interpolation functions, $[\bar{H}]$, from equation (21). Analytical expression for $[G]$ is available in Appendix C of Part I and the Fourier transforms of the two-dimensional interpolation functions are given in Appendix A.
5. Repeat the computations summarized in step 4 for each of the nodes, $i = 1, 2, \dots, M_n$ to determine $[C(\bar{x}_i)]$, $[\tilde{A}(\bar{x}_i, k_q)]$ and $[\tilde{B}(\bar{x}_i, k_q)]$ for all the nodes.
6. Evaluate the square matrix $[A(k_q)]$ of order $3M_n$ and the rectangular matrix $[B(k_q)]$ of size $3M_n \times 3M_i$ for the boundary element system from the corresponding

individual nodal matrices (step 5) using equations (29) and (30).

7. Solve the system of $3M_n$ linear algebraic equations (28) to express the nodal displacements $\{\bar{U}\}$ on $\bar{\Gamma}_c \cup \bar{\Gamma}_h$ in terms of the nodal tractions $\{T\}$ (equation 31).
8. For each sampling point $k = k_q$, compute the $3 \times 3M_i$ matrix $[E(\bar{x}_{oj}, k_q)]$ (equation 35) by interpolating the nodal displacements $\{\bar{U}\}$ determined in step 7.
9. Compute the $3 \times 3M_i$ matrix $[\tilde{f}_j(\omega)]$ from equation (37) wherein $[E(\bar{x}_{oj}, k_q)]$ for any k_q is known from step 8 and the wavenumber sampling points k_q were selected in step 3.
10. Repeat the computations summarized in step 9 for each of the nodes, $j = 1, 2, \dots, M_i$, on Γ_i and combine the resulting $[\tilde{f}_j(\omega)]$ according to equation (39) to obtain the $3M_i \times 3M_i$ flexibility influence matrix $[f(\omega)]$.
11. Compute the $3M_i \times 3M_i$ transformation matrix $[\Phi]$ from equation (41) wherein $[h(\bar{x})]$ was determined in step 1.
12. Compute the square matrix $[\hat{S}(\omega)]$ of order $3M_i$ from equation (43) wherein $[f(\omega)]$ and $[\Phi]$ are known from steps 10 and 11. The symmetric impedance matrix $[S_f(\omega)]$ is determined from equation (44).
13. Repeat the computations of steps 3 through 12 for each harmonic excitation frequency ω of interest to obtain the corresponding impedance matrix. The excitation frequencies should be selected to cover the frequency range over which the ground motion and dam response are significant.

NUMERICAL ASPECTS

Selection of Sampling Points in Wavenumber Domain

As mentioned in steps 3, 9 and 10 of the procedure summary, the computation to determine the nodal displacements $\{\bar{U}\}$ is repeated for a discrete set of wavenumbers k_q distributed over a truncated range $(-K, K)$. However, analyses are necessary only for positive wavenumbers because they indirectly also provide the displacements as-

sociated with corresponding negative wavenumbers (Appendix B). Having determined the displacements $\{\bar{U}\}$ associated with various k_q and $\{\bar{u}(\bar{x}_o, k_q)\}$ from equation (34), the displacements at the dam-foundation rock interface Γ_i are determined by numerically evaluating the integral of equation (6). Since solution of the "two-dimensional" problem to determine $\{\bar{u}(\bar{x}_o, k_q)\}$ requires much more computational effort compared to evaluation of the integral of equation (6), the integration scheme chosen should require as few sampling points in k_q as sufficient for required accuracy.

In order to properly select the discrete set of wavenumbers over the range $(0, K)$, the variation of $\{\bar{u}(\bar{x}_o, k)\}$ with k is examined next. This variation is plotted for the system shown in Figure 5. It is an infinitely-long canyon with a semi-circular cross-section of radius L and a dam-foundation rock interface of width $b = 0.2L$ subjected to uniform horizontal traction on the interface. The displacement-wavenumber plot for point A is presented in Figure 5. For each wavenumber k , the displacement at A is determined by implementing steps 4 to 7 of the procedure summary wherein $\{T\}^T = (0, 1, 0, \dots, 0, 1, 0)$ in equation (31). It is apparent that the displacements peak sharply at the Rayleigh wavenumber: $k_r = 1.07$ for $a_o = 1$ and $k_r = 4.29$ for $a_o = 4$ where $a_o = \omega L / \bar{c}_s$ is the normalized frequency. Thus finely-spaced wavenumber values would be necessary in the vicinity of k_r , whereas coarse spacing would suffice away from k_r .

Thus the wavenumber domain $(0, K)$ is divided into several subdomains, each with different step size, with the subdomain as well as step sizes depending on the excitation frequency, and the size and discretization of the system. Typically the four subdomains chosen were: $(0, k_r - \Delta k)$, $(k_r - \Delta k, k_r + \Delta k)$, $(k_r + \Delta k, k_r + \Delta k_1)$ and $(k_r + \Delta k_1, K)$ where $0 < \Delta k < k_r$ and $\Delta k_1 \geq 3\Delta k$. The integration is truncated at $k_q = K$ when the maximum amplitude of the displacements $\{\bar{U}\}$ is smaller than a specified tolerance. The four-point Gauss integration scheme utilized is convenient to implement and flexible to use. However, it has the disadvantage that, when accuracy needs to be improved, the previous results cannot be reused and the entire computation has

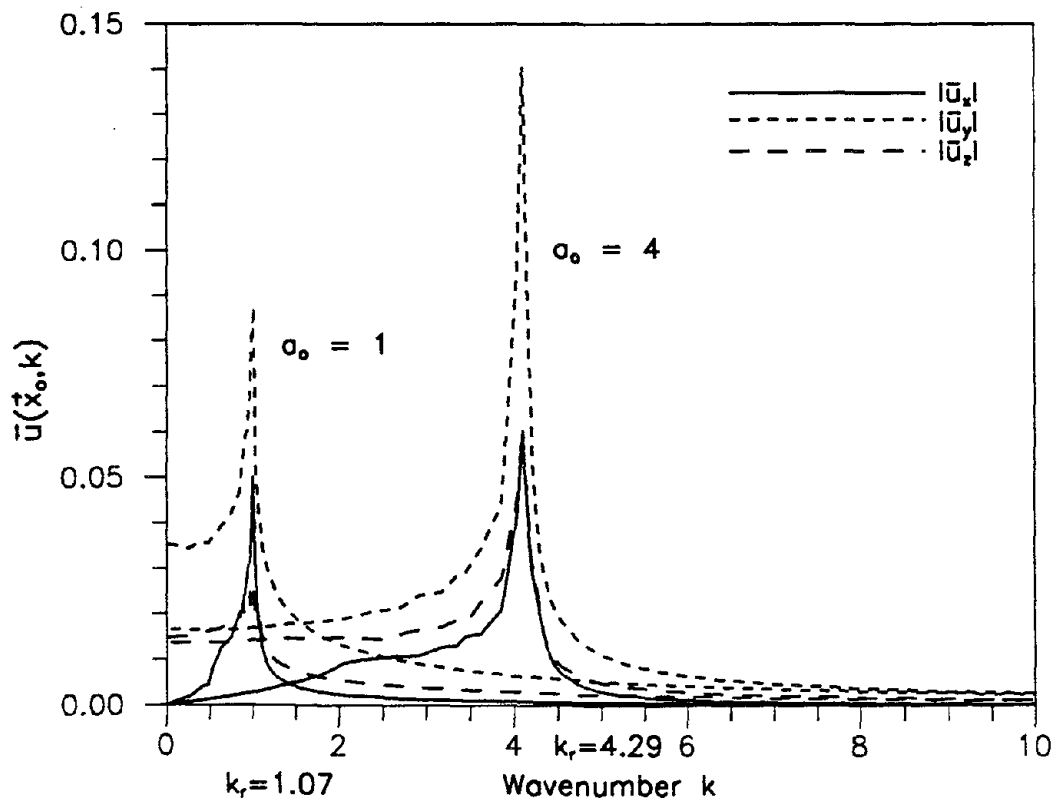
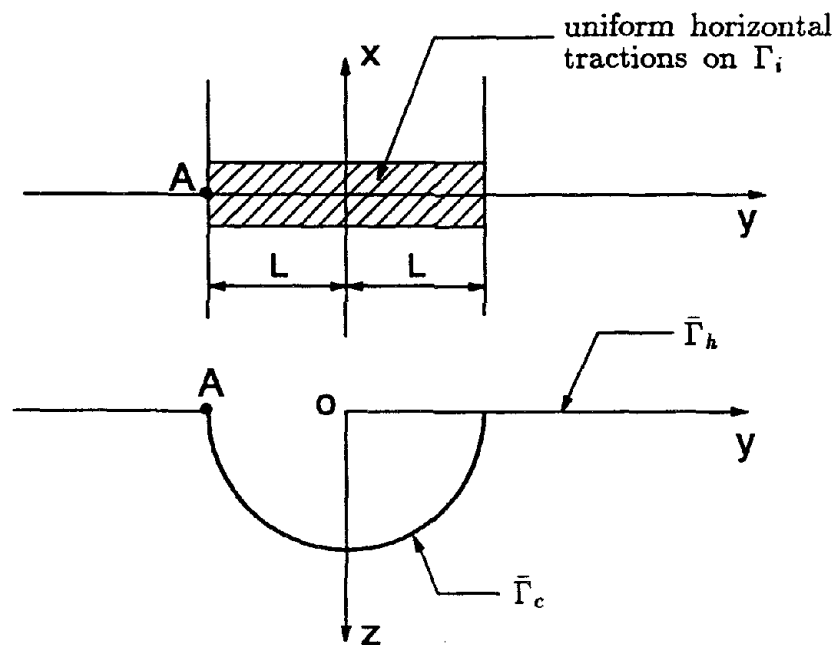


Fig.5 Variation of displacements $\{\bar{u}(\vec{x}_o, k)\}$ at A with wavenumber k ; $\alpha_o = \omega L/\bar{c}_s = 1$ and 4 , $\nu = 1/3$, $\eta_p = \eta_s = 0.02$.

to be repeated for a new set of wavenumbers.

Alternately, more complicated adaptive integration schemes may be employed to permit automatic control of errors and reuse of results from previous calculation. Since the actual integrand for the present problem is not one function but a matrix function with many entries (equation 37), direct implementation of an adaptive procedure may be inconvenient because large computer storage or input-output operation is needed to save the previously computed results. Therefore, the discrete set of wavenumber sampling points, k_q , are determined from a simple test function, which has the main features of the integrand.

From equation (31) and Appendix B, the nodal displacements on the boundary $\bar{\Gamma}_c \cup \bar{\Gamma}_h$ can be expressed as

$$\{\bar{U}(k)\} = [A(k)]^{-1}[B_G(k)][B_H(k)]\{T\} \quad (47)$$

where $[B_G(k)]$ consists of the transformed displacement Green's functions, $[G]$, and $[B_H(k)]$ consists of the Fourier transforms of the two-dimensional interpolation functions (equations 19 and 21), $[\bar{H}(\bar{x}_o, k)]$. The simple test function may be obtained by analyzing the main feature of each of the three matrices, i.e. $[A(k)]^{-1}$, $[B_G(k)]$ and $[B_H(k)]$, in equation (47). First, the entries in $[A(k)]^{-1}$ have peaks of different amplitudes near the Rayleigh wavenumber. Thus, the wavenumber dependence of $[A(k)]^{-1}$ may be characterized by $1/g(k)$ where $g(k)$ is the Rayleigh function given by [33]

$$g(k) = (2k^2 - k_s^2)^2 - 4k^2(k^2 - k_p^2)^{1/2}(k^2 - k_s^2)^{1/2} \quad (48)$$

Secondly, as k becomes greater than k_r and further increases, the nodal displacements $\{\bar{U}\}$ decrease which, as will be seen in the next subsection, is primarily controlled by the asymptotic behavior of the modified Bessel functions $K_0(a_s \bar{d})$ and $K_1(a_s \bar{d})$ in $[B_G(k)]$. The slowest decay among all elements in $[B_G(k)]$ with respect to k may be controlled by $K_1(a_s \bar{d}_{min})$ where \bar{d}_{min} is the shortest of all distances between a source point, \bar{x}_{os} , and all the integration points on $\bar{\Gamma}_c \cup \bar{\Gamma}_h$ used to evaluate equation (26).

Finally, the high frequency content in the variation of the nodal displacements $\{\bar{U}\}$ with respect to k is mostly due to the exponential terms in the matrix $[B_H(k)]$. This variation should be no faster than $e^{ik|x|_{max}}$ where $|x|_{max}$ is the maximum absolute value of the x -coordinate for the nodes on the dam-foundation rock interface (Appendix A). Combining the main features of the three matrices in equation (47), a test function may be chosen as

$$\phi(k) = \frac{K_1(a_s \bar{d}_{min})}{g(k)} e^{ik|x|_{max}} \quad (49)$$

It should be pointed out that the $\phi(k)$ of equation (49) does not represent any term in the matrix $[A(k)]^{-1}[B_G(k)][B_H(k)]$ but is intended to represent the main variation features of the matrix with respect to k . In particular, for a system with larger \bar{d}_{min} and $|x|_{max}$, equation (49) implies that finer sampling points over the wavenumber range $(0, K)$ should be selected, but the integration also can be truncated at a shorter K .

Based on this test function, any adaptive integration scheme, such as that based on Chebychev approximation [34] or quartic polynomial interpolation [8], may be used to determine the wavenumber sampling points, k_q . In this investigation, a simple adaptive integration scheme based on Simpson's rule was applied to the test function to determine k_q . In this scheme, the integration of the test function over a typical interval, (k_1, k_2) , is first computed by

$$I_1 = \frac{(k_2 - k_1)}{6} \left[\phi(k_1) + 4\phi\left(\frac{k_1 + k_2}{2}\right) + \phi(k_2) \right] \quad (50)$$

Then the integration is computed again by inserting two more sampling points midway between the first three sampling points through

$$I_2 = \frac{(k_2 - k_1)}{12} \left[\phi(k_1) + 4\phi\left(\frac{3k_1 + k_2}{4}\right) + 2\phi\left(\frac{k_1 + k_2}{2}\right) + 4\phi\left(\frac{k_1 + 3k_2}{4}\right) + \phi(k_2) \right] \quad (51)$$

If the relative error between I_1 and I_2 is below a specified tolerance, the five sampling points for the interval (k_1, k_2) are saved for later use. Otherwise, the process is repeated for the two intervals $(k_1, (k_1 + k_2)/2)$ and $((k_1 + k_2)/2, k_2)$ by adding more

sampling points. After the sampling points, k_q , for the test function are determined, the computation of the nodal displacements $\{\bar{U}\}$ is repeated for these k_q and the displacements at Γ_i are determined by numerically evaluating the integral of equation (6). The integration is truncated at $k_q = K$ when both $|\phi(k_q)|$ and the maximum amplitudes of the displacements $\{\bar{U}\}$ over the canyon surface are smaller than a prescribed tolerance. Numerical results show that this adaptive scheme associated with the test function of equation (49) works very well for a variety of systems and frequencies.

Truncation and Discretization Errors

As mentioned earlier, the infinite boundary integral on the half-space surface in equation (13) is replaced by an integral over a finite range, L_y (equation 22). Thus, the accuracy in the computation of matrix $[\tilde{A}(\bar{x}_i, k_q)]$ summarized in step 4(b) of the procedure summary is directly related to L_y . It is found that the L_y necessary to achieve a desired accuracy mainly depends on the wavenumber k and the excitation frequency ω , and is related to the decay of the displacements $\{\bar{u}(\bar{x}_o, k)\}$ along $\bar{\Gamma}_h$. Therefore, the variations of displacements on the half-space surface for various wavenumber k_q is examined. For this purpose, a rigid foundation of width $b = 0.2L$ on a semi-circular canyon of radius L (Figure 6a) is considered. The foundation interface is discretized evenly into 12 four node elements along circumference. Since, as mentioned in step 7 of the procedure summary, the displacements are expressed in terms of the nodal tractions $\{T\}$, it is only necessary to show the variation of displacements associated with some of the nodal tractions. The amplitudes of the Fourier transforms of displacements along the canyon and the half-space boundaries, $\bar{\Gamma}_c \cup \bar{\Gamma}_h$, due to horizontal tractions associated with the first node on Γ_i (Figure 6b) are plotted for several wavenumbers in Figures 7 and 8. These displacements are obtained from the second column of the matrix $[A(k_q)]^{-1}[B(k_q)]$ (equation 31), i.e. by specifying $\{T\} = \{0, 1, 0, \dots, 0\}^T$ in the equation. The normalized frequencies for the harmonic tractions are $a_o = \omega L / \bar{c}_s = 1$ and 2 with corresponding Rayleigh wavenumbers

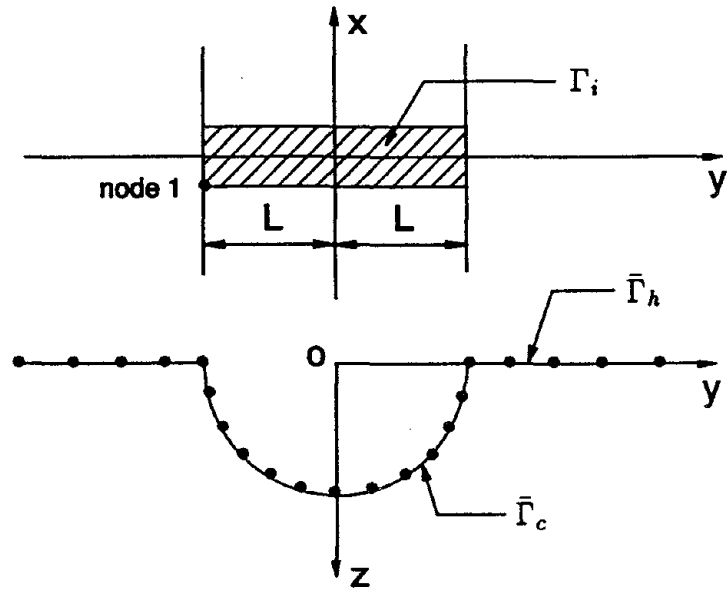


Fig.6a Dam-foundation interface on a semi-circular canyon.

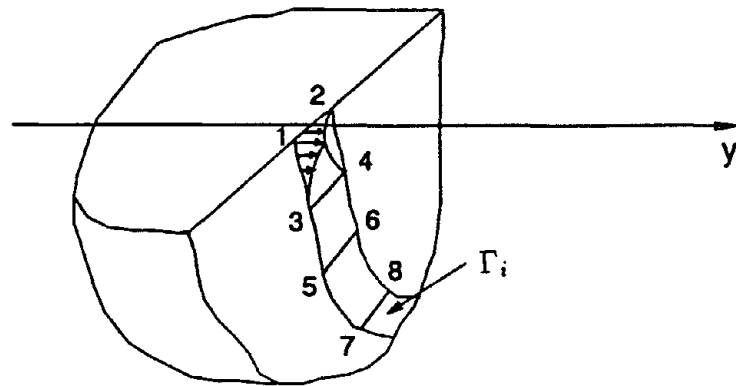


Fig.6b Horizontal tractions associated with node 1.

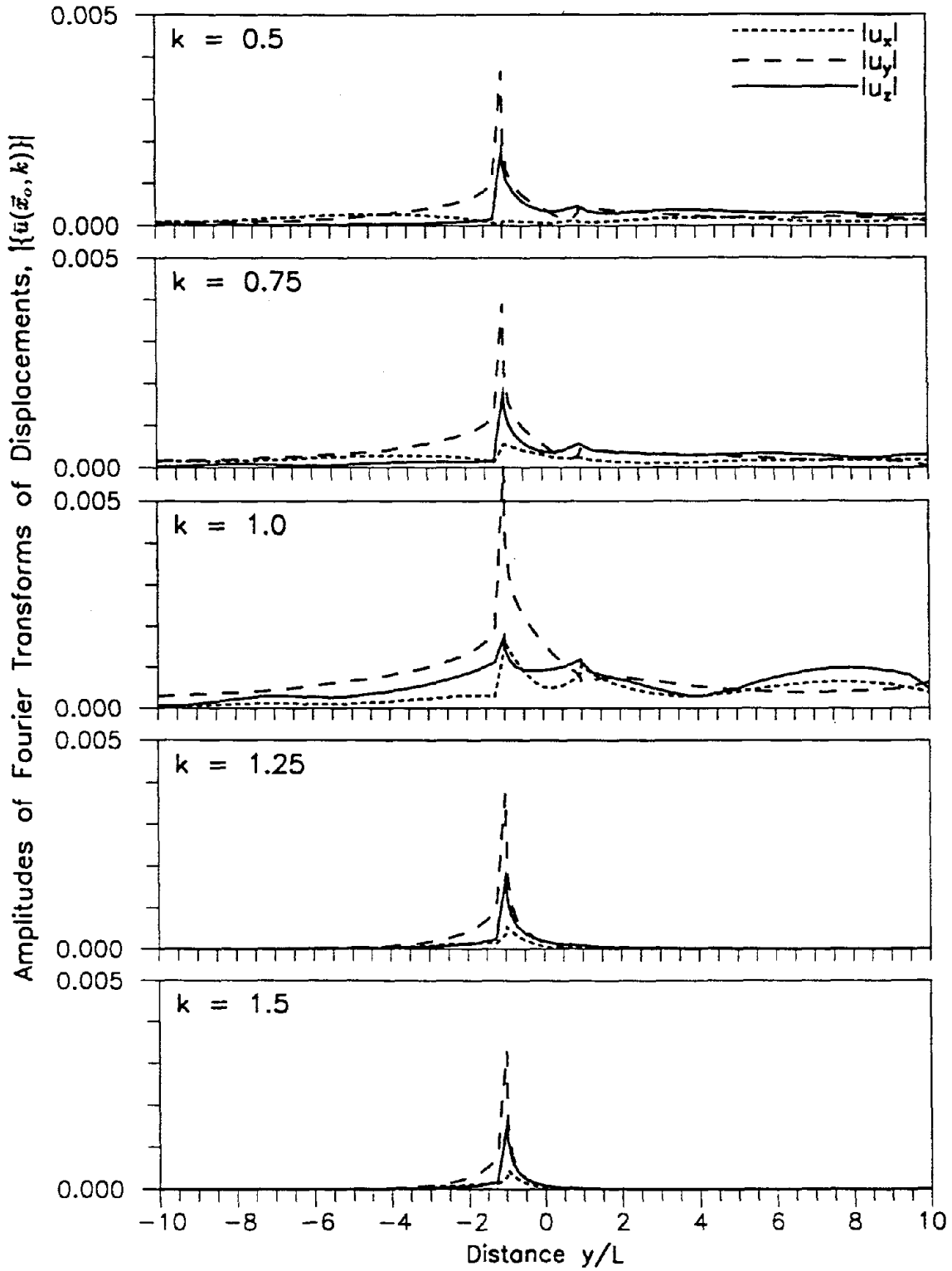


Fig.7 Variation of the amplitudes of Fourier transforms of displacements with distance; $a_0 = 1.0$, $\nu = 1/3$. Displacements are due to horizontal tractions associated with the first node for various values of wavenumber, k .

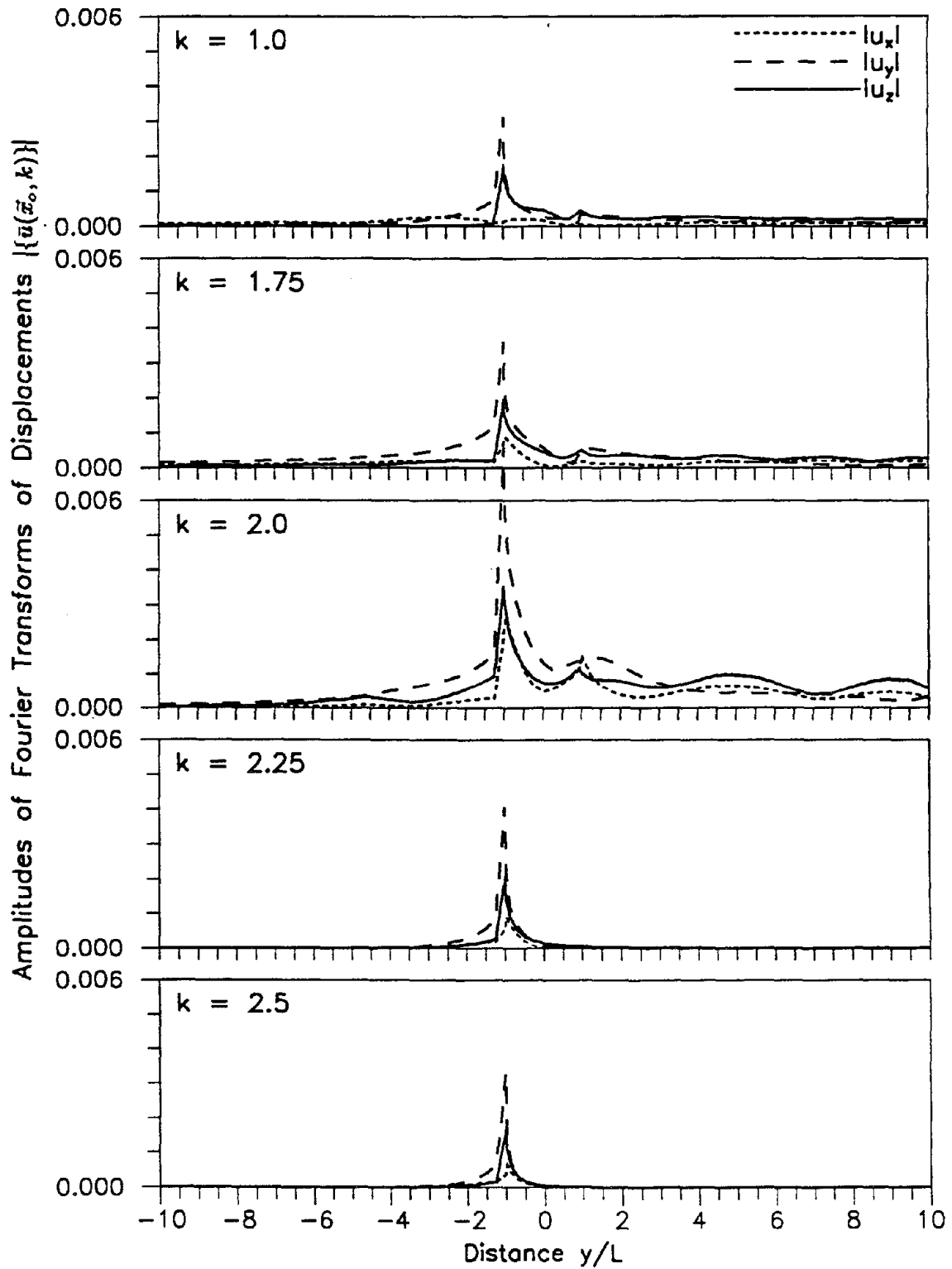


Fig.8 Variation of the amplitudes of Fourier transforms of displacements with distance; $a_0 = 2.0$, $\nu = 1/3$. Displacements are due to horizontal tractions associated with the first node for various values of wavenumber, k .

$k_r = 1.07$ and $k_r = 2.15$.

The displacements decay slowly with distance for wavenumber k_q close to the Rayleigh wavenumber k_r , not as slowly for $k_q < k_r + 0.5$, and very fast for $k_q > k_r + 0.5$ (Figures 7 and 8). An explanation for the dependence of the decay rate of $\{\bar{u}(\bar{x}, k_q)\}$ with distance on k_q can be obtained by examining the asymptotic expressions for the transformed Green's functions where the decaying trend is dominated by the modified Bessel functions $K_0(a_s \bar{d})$ and $K_1(a_s \bar{d})$ with $a_s = \sqrt{k_q^2 - k_s^2}$ and \bar{d} being the distance between source and receiver points (Appendix C of Part I). It should be noted that k_r is larger than, but very close to k_s . Thus, when $k_q > k_r + \delta$ where δ is a small positive number depending on the size of the system, a_s is a complex number with positive real part which increases with k_q . For large arguments, the asymptotic expressions for $K_0(a_s \bar{d})$ and $K_1(a_s \bar{d})$ are given by

$$K_0(a_s \bar{d}) \approx \sqrt{\frac{\pi}{2a_s \bar{d}}} e^{-a_s \bar{d}} \left(1 - \frac{1}{8a_s \bar{d}}\right) \quad (52a)$$

$$K_1(a_s \bar{d}) \approx \sqrt{\frac{\pi}{2a_s \bar{d}}} e^{-a_s \bar{d}} \left(1 + \frac{3}{8a_s \bar{d}}\right) \quad (52b)$$

respectively. As a result, K_0 and K_1 decay exponentially with respect to \bar{d} which leads to rapid decay of $\{\bar{u}(\bar{x}_o, k_q)\}$ along $\bar{\Gamma}_h$. When $k_q \leq k_r + \delta$, the real part of a_s is still positive, but it is very small (for zero damping, e.g., $Re(a_s) = 0$ for $k_s < k_s$) which makes the decay much slower.

Comparing Figures 7 and 8, it can be observed that the displacements decay more rapidly along the half-space surface for high frequency excitation. Therefore, for computational efficiency, the discretization range L_y should vary with wavenumber k_q and frequency ω .

For the rigid banded foundation shown in Figure 6, the impedance matrix with respect to the mid-bottom point O' of the foundation can be obtained from equation

(46) and expressed as

$$[S_r(\omega)] = \mu L \begin{pmatrix} S_{xx} & 0 & 0 & 0 & LS_{xm} & 0 \\ 0 & S_{yy} & 0 & LS_{yr} & 0 & 0 \\ 0 & 0 & S_{zz} & 0 & 0 & 0 \\ 0 & LS_{yr} & 0 & L^2 S_{rr} & 0 & 0 \\ LS_{xm} & 0 & 0 & 0 & L^2 S_{mm} & 0 \\ 0 & 0 & 0 & 0 & 0 & L^2 S_{tt} \end{pmatrix} \quad (53)$$

where μ is the shear modulus for the half-space, S_{xx} , S_{yy} and S_{zz} are the translational impedance coefficients, S_{rr} and S_{mm} are the rocking impedance coefficients, S_{tt} is the torsional impedance coefficient, and S_{yr} and S_{xm} are the coupling terms. All the coefficients are in a non-dimensional form. The variation of impedance coefficients with L_y is shown in Figures 9 to 12 where the smooth curves are obtained by connecting the results at $L_y/\lambda_s = 0.0, 0.5, 1.0, 1.5, 2.0, 2.5, 3.0, 3.5$ and 4.0 through a cubic spline approximation and the impedance coefficients are normalized by their "exact" values which are obtained by using $L_y = 5\lambda_s$. In this example, different L_y are selected for $k_q \leq k_r + 0.5$ and $k_q > k_r + 0.5$, and the L_y appearing in the figures refers to the discretization range used for $k_q \leq k_r + 0.5$. The relative errors decrease faster with respect to L_y for higher frequency and, for most coefficients, they become less than two percent if $L_y > 2\lambda_s$. For $a_o = 2$, the relative errors for the imaginary parts of the vertical impedance function S_{zz} and the coupling term S_{yr} are relatively large, but they are within $\pm 4\%$. Thus, for $k_q \leq k_r + \delta$, L_y should be at least $2\lambda_s$. Since the shear wavelength for low frequency is larger than that for high frequency, larger discretization range is required for low frequency in general. However, because k_r decreases with frequency and coarse discretization is adequate for low frequency, the total computational cost due to large L_y for low frequency case does not necessarily increase.

For $k_q > k_r + \delta$, a shorter discretization range L_y is adequate because of the rapid exponential decay of the transformed Green's functions. In this investigation, L_y for $k_q > k_r + \delta$ is chosen according to

$$\frac{L_y}{\lambda_s} = 2 \sqrt{\frac{(k_r + \delta)^2 - k_s^2}{k_q^2 - k_s^2}} \quad (54)$$

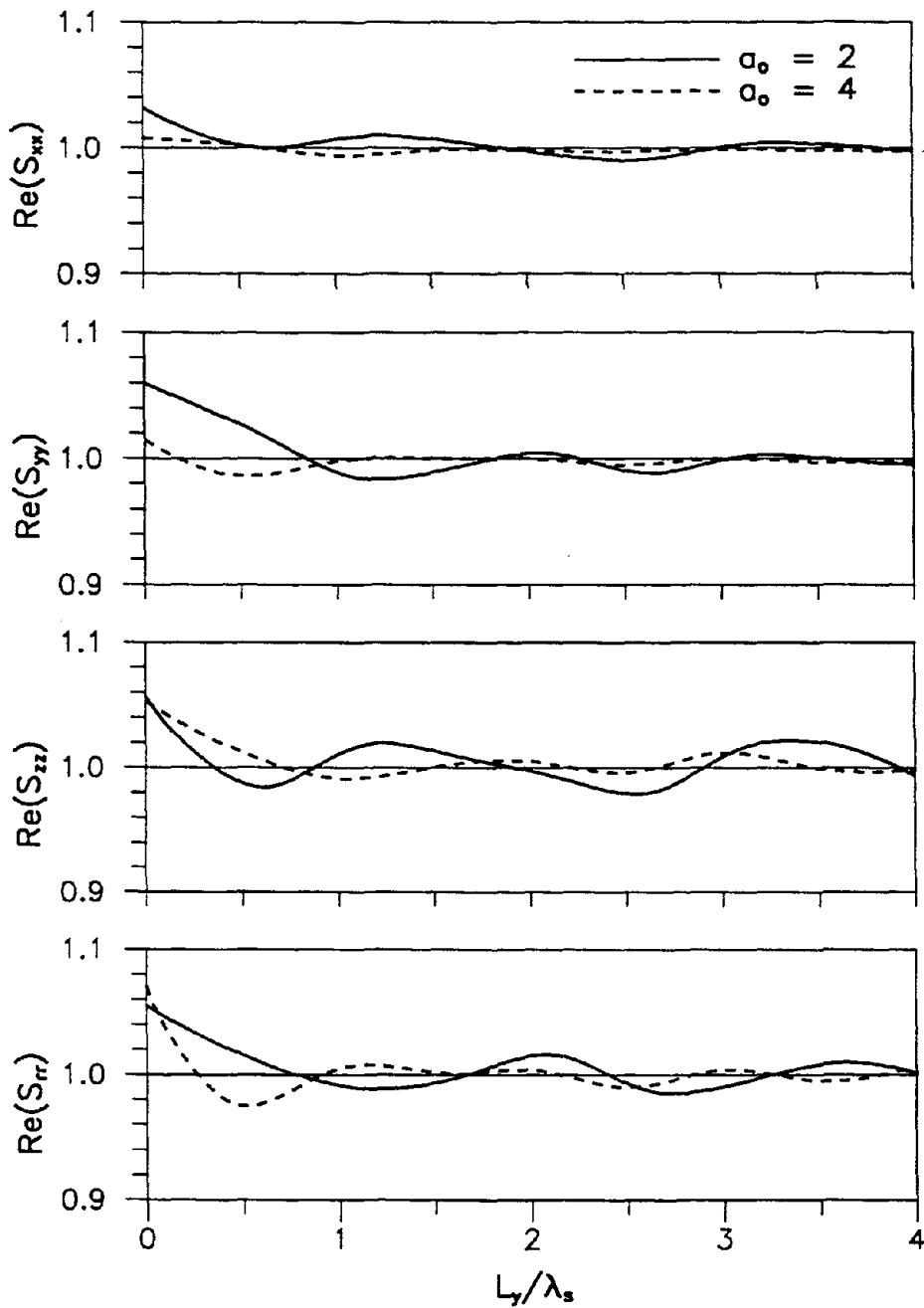


Fig.9 Real parts of the impedance coefficients determined with various values of L_y , defining the discretization range on the half-space surface. The impedance coefficients are normalized by their "exact" values. Results are presented for $a_0=2$ and 4.

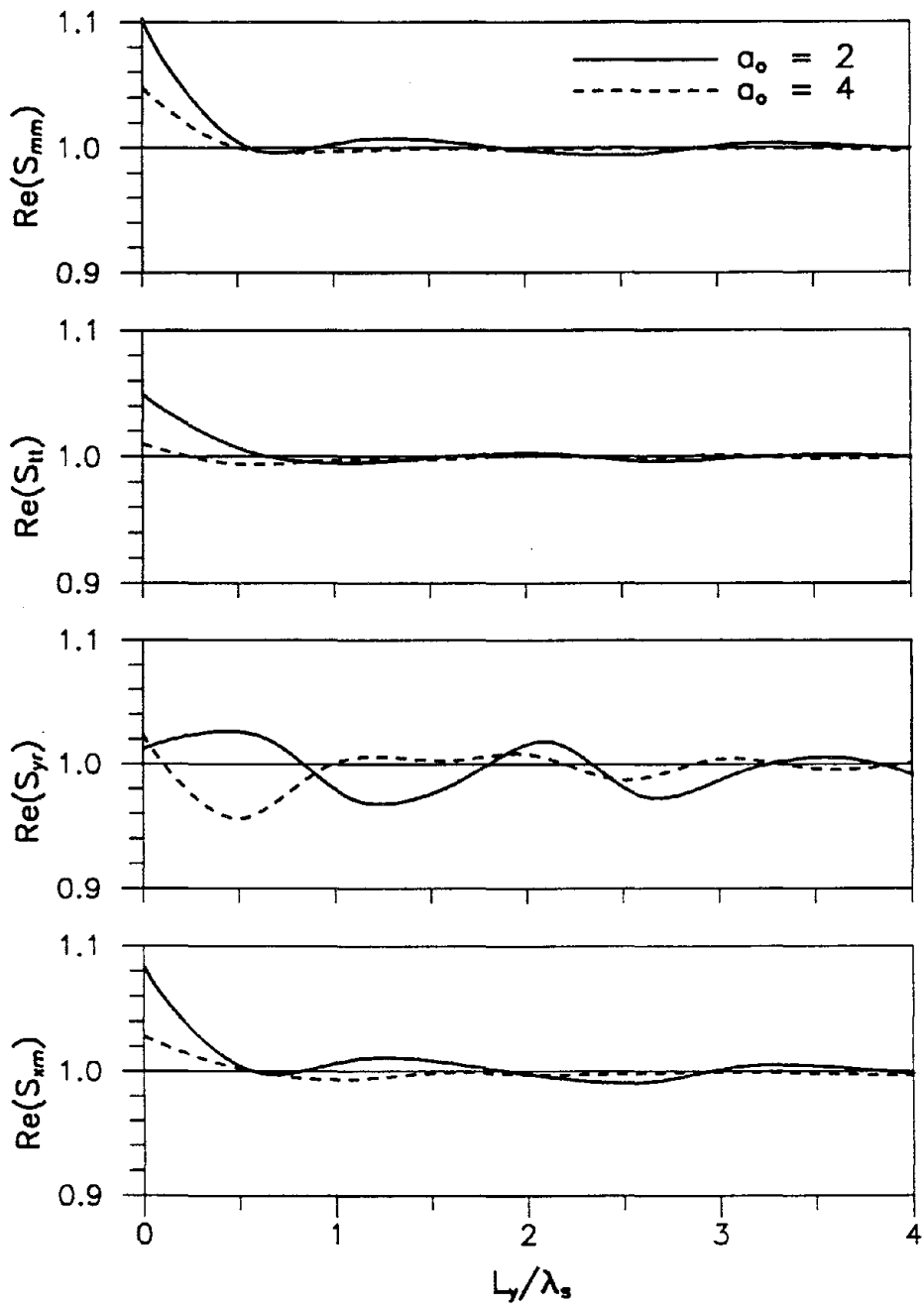


Fig.10 Real parts of the impedance coefficients determined with various values of L_y , defining the discretization range on the half-space surface. The impedance coefficients are normalized by their "exact" values. Results are presented for $a_o=2$ and 4.

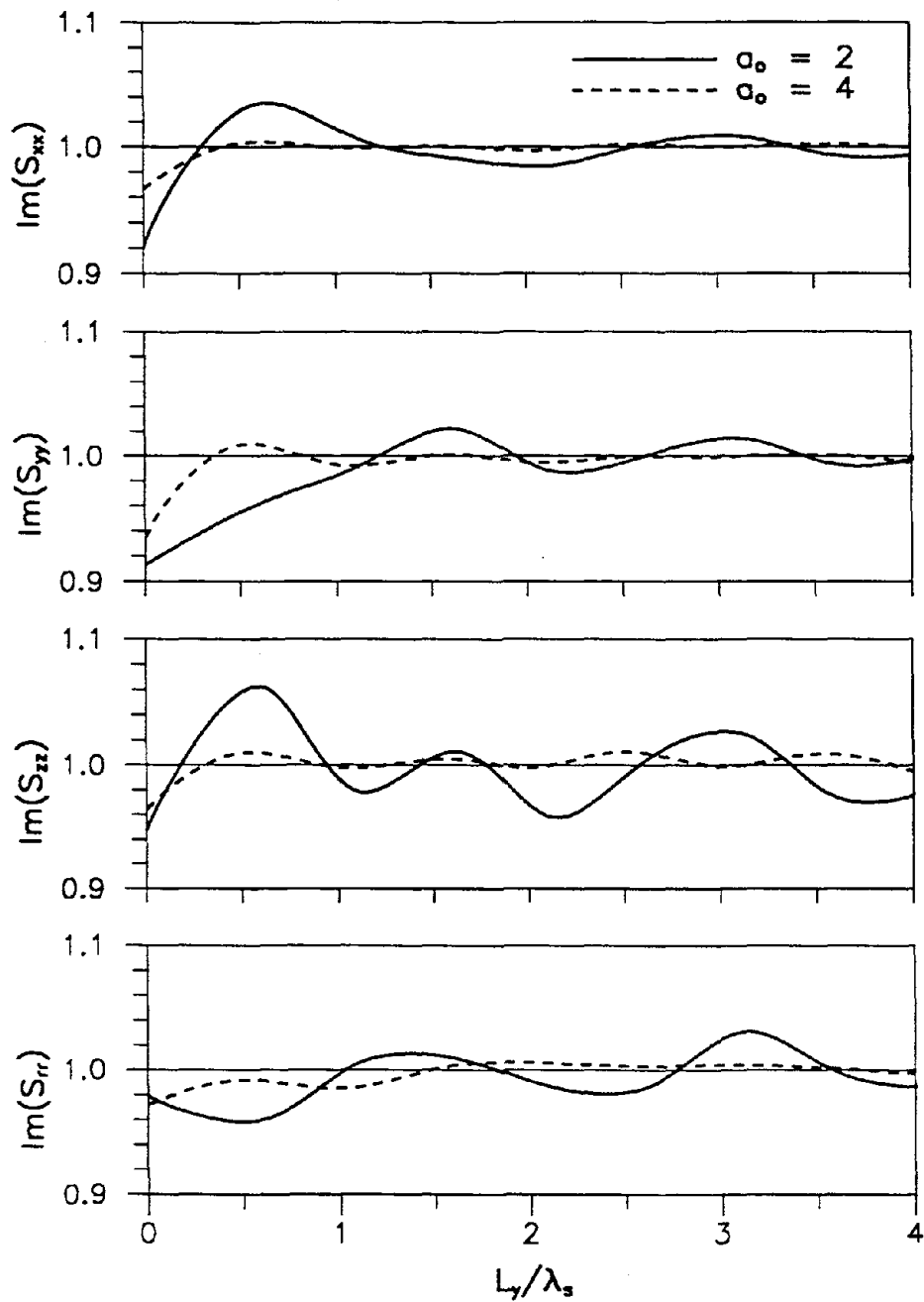


Fig.11 Imaginary parts of the impedance coefficients determined with various values of L_y , defining the discretization range on the half-space surface. The impedance coefficients are normalized by their "exact" values. Results are presented for $\alpha_o=2$ and 4.

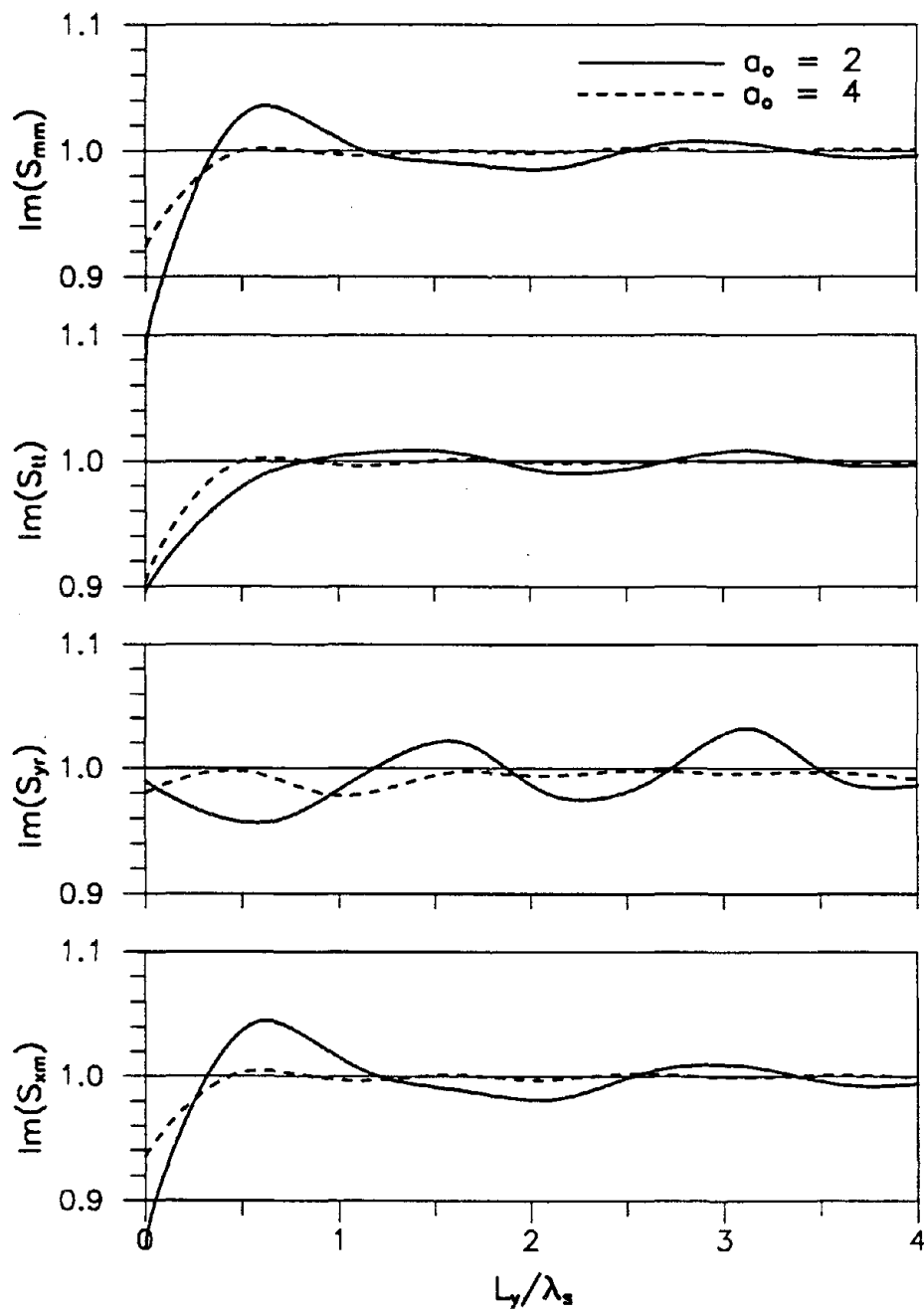


Fig.12 Imaginary parts of the impedance coefficients determined with various values of L_y , defining the discretization range on the half-space surface. The impedance coefficients are normalized by their "exact" values. Results are presented for $a_0=2$ and 4.

which decreases with increasing k_q . To ensure the accuracy of the results on $\bar{\Gamma}_c$, however, L_y should not decrease without limit. Since the errors in the computed displacements near the end of the discretization on $\bar{\Gamma}_h$ are relatively large, it is recommended that L_y should be greater than the smaller one of λ_s and the half width of the canyon.

The size of elements on the half-space boundary $\bar{\Gamma}_h$ may vary depending on their distances from the canyon. In this study, element sizes on $\bar{\Gamma}_h$ are chosen according to an arithmetic series ($l, l + \Delta l, l + 2\Delta l, \dots$) where the elements adjacent to the canyon have the same size as their neighbors on $\bar{\Gamma}_c$ and the elements farthest away have the size $\lambda_s/4$. Furthermore, in order to avoid ill-conditioning or singularity in the flexibility influence matrix $[f]$ (equation 39), there are some restrictions on location of nodes on the canyon boundary $\bar{\Gamma}_c$ relative to the locations of nodes on Γ_i . Detailed description and theoretical background for this restriction are given in Appendix C.

In summary, the following guidelines for selection of k_q , K , L_y and the element sizes are recommended:

1. The sampling points, k_q , in the wavenumber domain should be chosen unevenly with finely-spaced sampling points near the Rayleigh wavenumber and coarsely-spaced sampling points elsewhere. Either piecewise Gauss integration scheme or an adaptive integration procedure can be used to determine k_q . The adaptive procedure may be combined with a test function which characterizes the main features of the Fourier transforms of the displacements and the integral in equation (6) may be truncated when the magnitudes of the test function and the nodal displacements $\{\bar{U}\}$ on canyon boundary are smaller than a prescribed tolerance.

2. The choice of the integration range, L_y , on the half-space surface should depend on k_q . For $k_q \leq k_r + \delta$, where δ is a small positive number depending on the size of the system, $L_y > 2\lambda_s$ where λ_s is the shear wavelength. For $k_q > k_r + \delta$, L_y may be chosen according to equation (54) with the restriction that L_y is greater than the

smaller of two values: λ_s and the half width of the canyon.

3. The element size on both the dam-foundation rock interface, Γ_i , and the boundary $\bar{\Gamma}_c$ should be kept smaller than $\lambda_s/5$.

VERIFICATION AND COMPUTATIONAL COSTS

A computer program was developed to implement the step by step procedure summarized earlier to determine the impedance matrix of the foundation rock region shown in Figure 1 with reference to the degrees of freedom on the dam-foundation rock interface Γ_i . Results for two systems are presented to demonstrate verification of the present procedure.

The first system analyzed is a rigid square footing on the surface of a half-space for which the impedances or compliances are available [10,18]. Figure 13 shows some of the compliance functions determined by various methods for different non-dimensional frequency $a_o = \omega b/\bar{c}_s$ where b is the half-width of the footing. The hysteretic damping factors used in the present analysis are $\eta_p = \eta_s = 0.001$. In applying the present method, the interface between the footing and the half-space is discretized into thirty six 8-node, square elements, the line segment $(-b,b)$, which is equivalent to $\bar{\Gamma}_c$, is discretized into 12 elements, and the boundary $\bar{\Gamma}_h$ on the half-space surface is discretized up to $L_y = 2\lambda_s$ for $k_q \leq k_r + 0.5$ where λ_s is the corresponding shear wavelength. The agreement between various results shown in Figure 13 is satisfactory. The differences may be, in part, due to the finite discretization range, L_y , on the half-space surface, which leads to a stiffer system in the present method, and the slight difference in damping used in the various analyses.

The second system analyzed is an infinitely-long canyon of semi-circular cross-section of radius L with a dam-foundation rock interface of width $b = 0.2L$ (Figure 14). The impedance functions are determined for the interface Γ_i assumed to be rigid with six degrees of freedom. In implementing the present procedure, the interface is discretized evenly into 12 elements along the circumferential direction and 2 elements

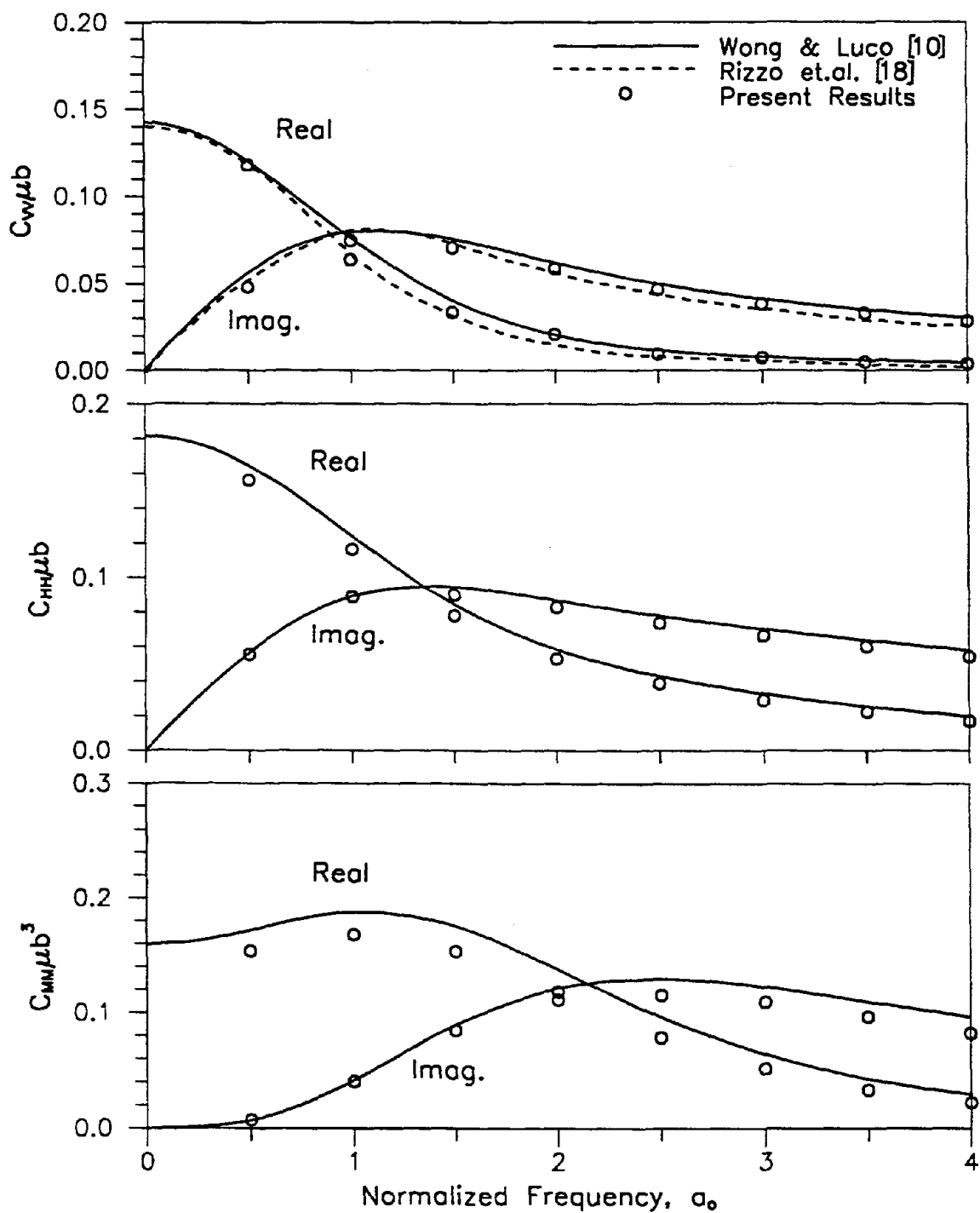
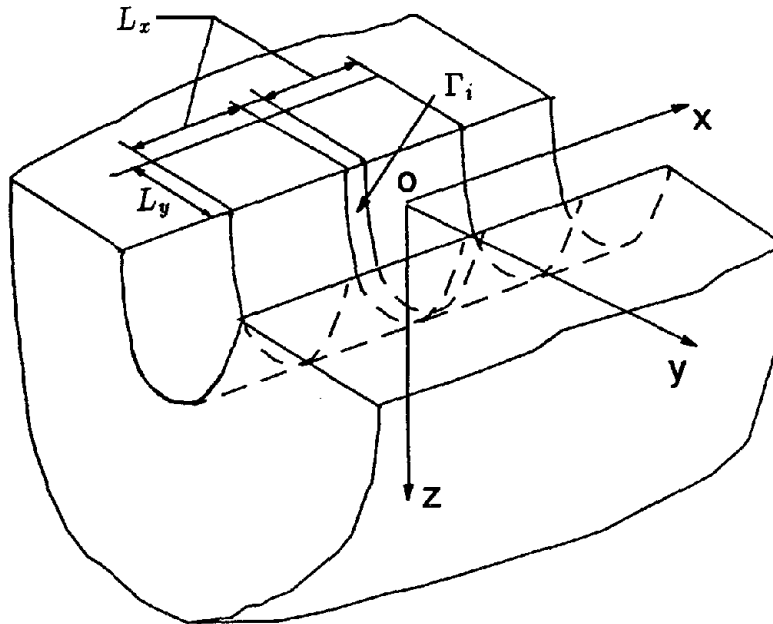
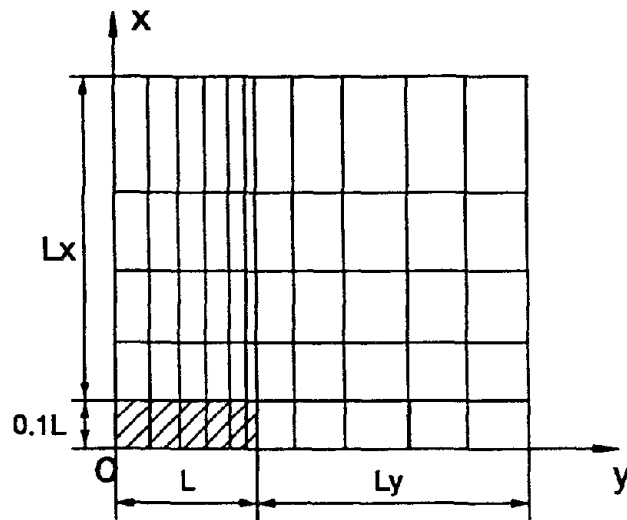


Fig.13 Comparison of compliances obtained by present method with previous results for vertical (C_{VV}), horizontal (C_{HH}) and rocking (C_{MM}) compliances of square footing supported on the surface of a viscoelastic half-space ($\nu = 1/3$).



(a) Dam-foundation interface



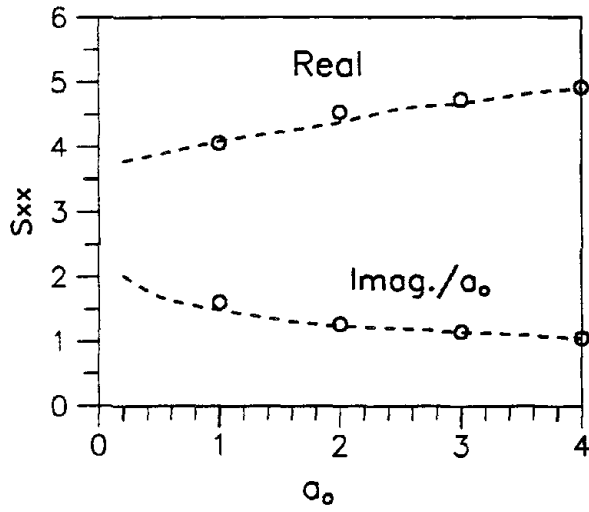
(b) Plan view of a quarter of an illustrative (not actual) three-dimensional boundary element discretization

Fig.14 Dam-foundation interface on a semi-circular canyon of radius L .

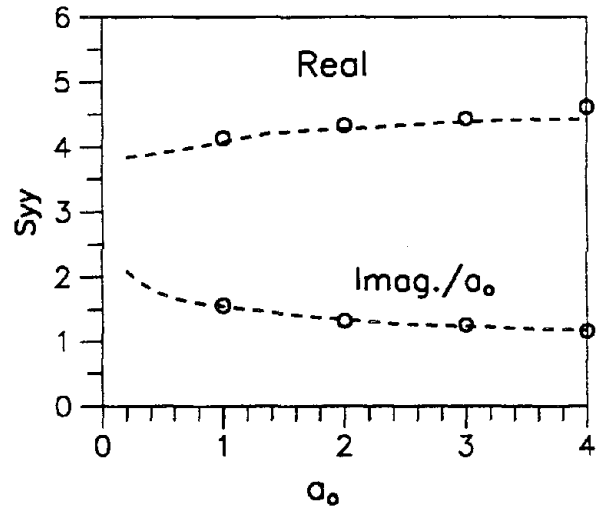
along the canyon axis. The boundary $\bar{\Gamma}_c$ is discretized evenly into 12 line elements and $L_y = 2\lambda_s$ for $k_q < k_r + 0.5$. The impedances are presented in Figures 15 and 16 as a function of the normalized frequency $a_o = \omega L/\bar{c}_s$. These impedance functions result from cubic spline functions connecting computed impedance values for $a_o = 0.2, 0.5, 1.0, 1.5, 2.0, 2.5, 3.0, 3.5$ and 4.0. Because previous results are apparently not available for this system, the impedances were also obtained by analyzing the same system by a three-dimensional boundary element method (equation 8). The interface Γ_i , a finite length $L_x = L$ of the canyon, and the half-space surface up to $L_y = L$ are discretized by two-dimensional boundary elements (Figure 14). The agreement is satisfactory between the results obtained by the 3-D boundary element method and by the procedure presented in this report.

Compared with the general 3-D boundary element approach, the present method is more accurate since the boundary integration in the direction of canyon axis is evaluated analytically. If highly-accurate results are desired, the present method is also more efficient. This is illustrated in Table 1 where the relative errors in the impedance coefficients for the second problem described above are listed. The system was analyzed by the 3-D boundary element method with $L_y = L$ and various values of L_x , and by the present method with $L_y = L$. Lacking an exact solution for this problem, the comparison is performed against the solutions by the present method with the discretization range $L_y = 2\lambda_s$. Clearly, the performance of the present method is superior to that of the 3-D boundary element methods in accuracy and computational time if results with errors less than 5% are desired.

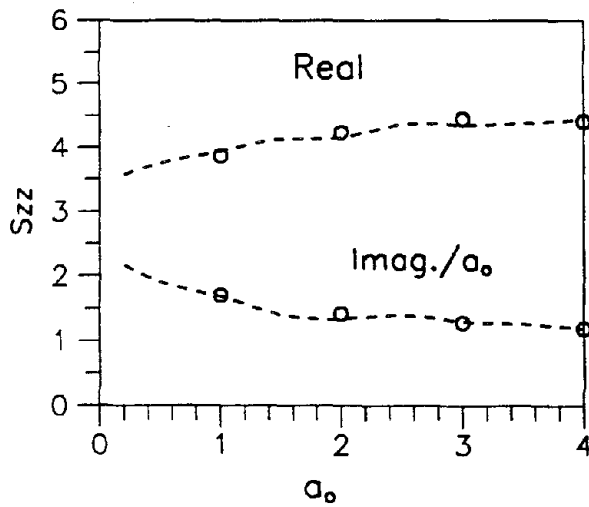
The present method is especially efficient when the number of DOF along the canyon axis is relatively large (Appendix B). Since the computer program implementing the 3-D boundary method was not written with blockwise storage and, hence, is limited by the computer storage capacity, relatively short discretization ranges L_y and L_x were used (Table 1). In general, however, such short discretization range are not expected to lead to accurate results because the results are likely to oscillate with L_y



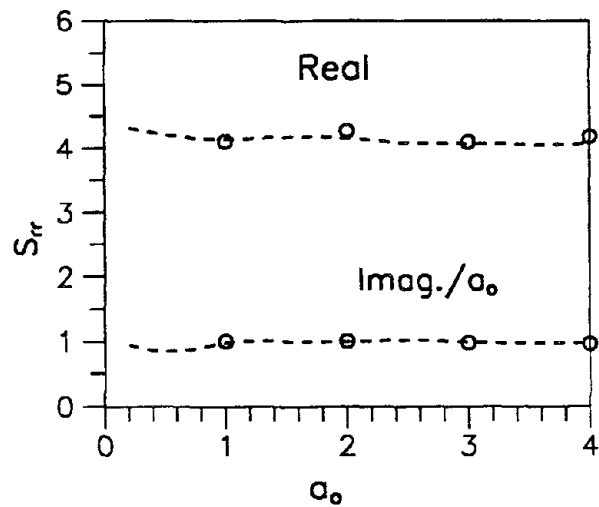
(a) Translational Impedance S_{xx}



(b) Translational Impedance S_{yy}

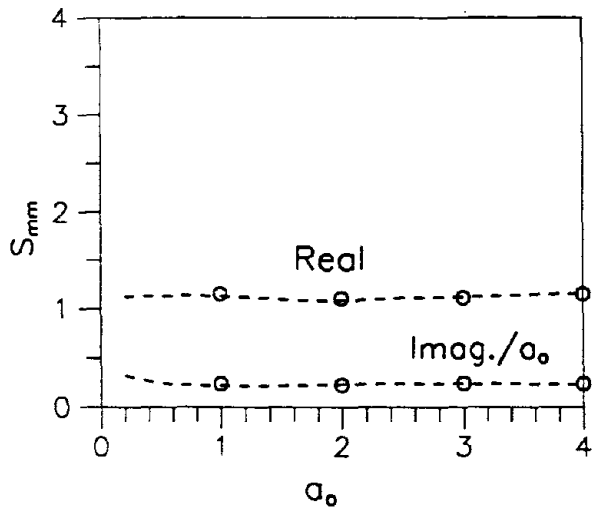


(c) Translational Impedance S_{zz}

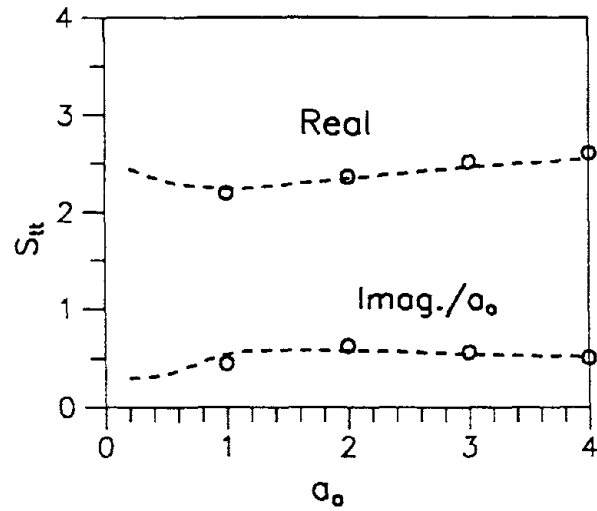


(d) Rocking Impedance S_{rr}

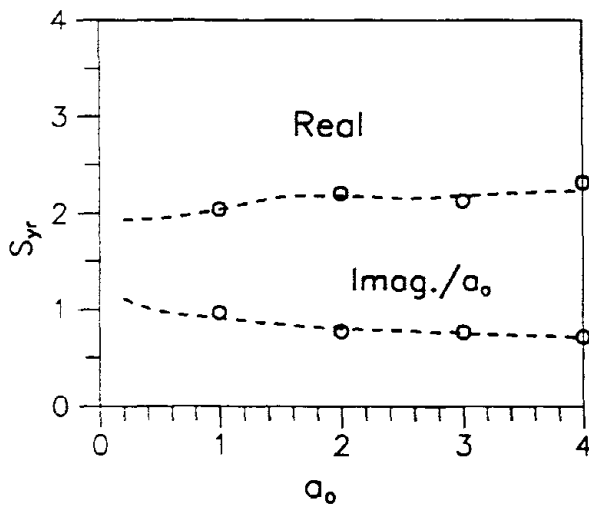
Fig.15 Comparison of foundation impedances obtained by the present method (dashed lines) with the 3-D boundary element method with $L_x = L$ (symbols). The system analyzed is a rigid foundation of width $0.2L$ on a semi-circular canyon of radius L ($\nu = 1/3$, $\eta_p = \eta_s = 0.02$).



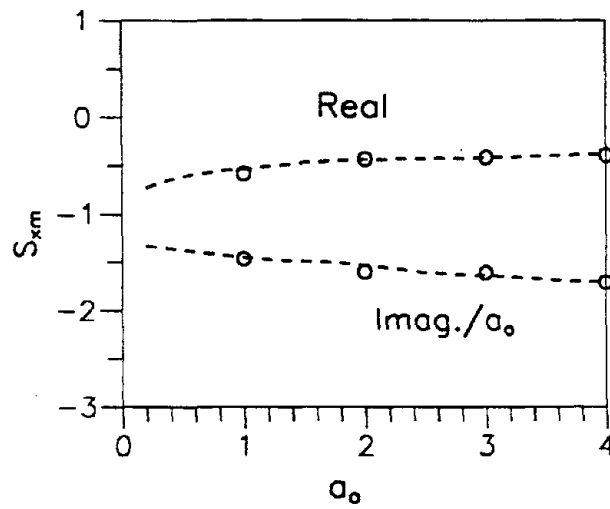
(a) Rocking Impedance S_{mm}



(b) Torsional Impedance S_{tt}



(c) Coupling Impedance S_{yr}



(d) Coupling Impedance S_{xm}

Fig.16 Comparison of foundation impedances obtained by the present method (dashed lines) with the 3-D boundary element method with $L_x = L$ (symbols). The system analyzed is a rigid foundation of width $0.2L$ on a semi-circular canyon of radius L ($\nu = 1/3$, $\eta_p = \eta_s = 0.02$).

Table 1 Percentage Errors in Impedances and Computation Time for Two Methods

Impedances		3-D Boundary Element Method with $L_x =$					Present Method with $L_x = L$
		0.0	0.25L	0.5L	0.75L	1.0L	
$a_o = 2$	Re(S_{xx})	7.0	4.2	4.1	4.1	3.7	0.6
	Im(S_{xx})	18.4	10.5	7.3	4.7	2.1	-1.3
	Re(S_{yy})	-7.9	3.6	4.0	2.6	1.3	0.2
	Im(S_{yy})	15.3	8.7	1.6	-1.0	-1.5	2.6
	Re(S_{zz})	1.8	3.2	2.2	1.9	1.9	2.0
	Im(S_{zz})	10.4	6.3	5.0	5.3	5.4	-3.8
	Re(S_{rr})	-5.5	-1.1	1.1	2.6	2.9	0.8
	Im(S_{rr})	7.8	8.2	6.9	4.5	1.1	3.0
	Re(S_{mm})	13.9	7.8	4.2	2.7	2.1	0.5
	Im(S_{mm})	-3.1	-8.4	-6.3	-3.7	-2.2	-1.0
	Re(S_{tt})	-3.5	-6.6	-4.9	-1.8	0.8	0.0
	Im(S_{tt})	-9.8	-1.7	5.7	9.7	8.3	1.2
	Re(S_{yr})	-1.2	1.3	2.6	2.3	1.3	0.8
	Im(S_{yr})	13.6	7.6	2.3	-1.1	-3.4	2.7
	Re(S_{zm})	14.7	9.8	6.9	5.5	4.4	0.8
	Im(S_{zm})	13.2	3.2	1.1	-0.02	-1.6	-1.7
$a_o = 4$	Re(S_{xx})	0.02	-2.9	2.1	3.2	0.3	0.5
	Im(S_{xx})	-4.1	3.8	5.9	2.3	0.8	-0.1
	Re(S_{yy})	4.8	4.2	2.8	3.8	4.3	0.2
	Im(S_{yy})	4.4	-1.3	0.3	1.5	-0.4	1.3
	Re(S_{zz})	-1.3	-1.3	1.8	2.4	-0.8	1.0
	Im(S_{zz})	-1.3	2.3	2.9	0.6	0.04	0.1
	Re(S_{rr})	9.9	3.2	0.5	1.5	5.1	-1.9
	Im(S_{rr})	2.3	-3.6	-1.2	1.7	-0.8	1.7
	Re(S_{mm})	-9.4	-4.8	1.5	1.6	0.0	-0.1
	Im(S_{mm})	-0.6	7.6	7.6	4.1	4.5	-0.03
	Re(S_{tt})	18.7	5.8	3.6	3.8	2.6	-0.3
	Im(S_{tt})	3.6	-1.7	0.2	0.7	-2.0	0.6
	Re(S_{yr})	14.5	2.0	0.9	2.3	3.8	-1.7
	Im(S_{yr})	0.1	-0.8	1.6	3.8	0.7	2.8
	Re(S_{zm})	-8.0	-6.5	0.2	1.9	-0.3	0.5
	Im(S_{zm})	-7.2	4.2	7.0	4.0	3.5	-0.1
Compt. Time* (sec.)		3.1	7.9	15.6	26.6	41.4	24.0

* on Cray X-MP/14

and L_x (Table 1) until both discretization ranges extend two times the shear wavelength.

The present method has the advantage that it requires much less storage compared to the 3-D boundary method. Thus the accuracy of the present method can be improved at extra computational cost by increasing the discretization range and making the discretization finer. However, the accuracy of the 3-D boundary method is likely to be limited by the available computer storage.

CONCLUSIONS

A direct boundary element procedure is presented to determine the impedance matrix, i.e. the frequency-dependent stiffness matrix, associated with the nodal points at the base of a structure supported on a canyon cut in a homogeneous viscoelastic half-space. The canyon is infinitely-long and may be of arbitrary but uniform cross-section. The uniform cross-section of the canyon permits analytical integration along the canyon axis of the three-dimensional boundary integral equation. Thus the original three-dimensional problem is reduced to an infinite series of two-dimensional boundary problems, each of which corresponds to a particular wavenumber and involves Fourier transforms of full-space Green's functions. Appropriate superposition of the solutions of these two-dimensional boundary problems leads to a dynamic flexibility influence matrix which is inverted to determine the impedance matrix.

A step-by-step summary of the procedure is presented and numerical aspects of the method have been investigated. In particular, guidelines are presented for selection of the sampling points in the wavenumber domain, the finite discretization range on the half-space surface necessary to approximate the infinite range, and the element size on the dam-foundation rock interface.

The accuracy of the procedure and implementing computer program has been verified by comparison with previous results for a surface-supported, square foundation and solutions for a foundation of finite-width on a infinitely-long canyon by a three-

dimensional boundary element method (BEM). Compared with the three-dimensional BEM, the present method requires less computer storage and is more accurate and efficient. Computation of the foundation impedance matrix by this method would enable earthquake analysis of arch dams including dam-foundation rock interaction effects.

REFERENCES

1. G. Fenves and A.K. Chopra, "Earthquake Analysis of Concrete Gravity Dams Including Reservoir Bottom Absorption and Dam-Water-Foundation Rock Interactions," *Earthquake Engineering and Structural Dynamics*, **12**, pp.663-680, 1984.
2. K.-L. Fok and A.K. Chopra, "Earthquake Analysis of Arch Dams Including Dam-Water Interaction, Reservoir Boundary Absorption and Foundation Flexibility," *Earthquake Engineering and Structural Dynamics*, **14**, pp.155-184, 1986.
3. P.S. Nowak, "Effect of Nonuniform Seismic Input on Arch Dams," *Report No. EERL 88-03*, California Institute of Technology, Pasadena, California, 1988.
4. Y. Ghanaat and R.W. Clough, "EADAP Enhanced Arch Dam Analysis Program, User's Manual," *Report No. UCB/EERC-89/07*, Earthquake Engineering Research Center, University of California, Berkeley, Nov. 1989.
5. J.P. Wolf and G.R. Darbre, "Dynamic-stiffness Matrix of Soil by The Boundary Element Method: Embedded Foundation," *Earthquake Engineering and Structural Dynamics*, **12**, pp.401-416, 1984.
6. E. Alarcon, J. Dominguez and F.del Cano, "Dynamic Stiffness of Foundations," *New Developments in Boundary Element Methods, Proc. 2nd int. seminar recent advances boundary element methods*, (ed. C.A. Brebbia), pp.264-280, 1980.
7. T-J. Tzong and J. Penzien, "Hybrid Modeling of a Single-Layer Half-Space System in Soil-Structure Interaction," *Earthquake Engineering and Structural Dynamics*, **14**, pp.517-530, 1986.
8. R.J. Apsel, "Dynamic Green's Functions for Layered Media And Applications to Boundary-value Problems," *Ph.D. Dissertation*, University of California, San Diego, CA, 1979.
9. R.J. Apsel and J.E. Luco, "Impedance Functions for Foundations Embedded in a Layered Medium," *Earthquake Engineering and Structural Dynamics*, **15**, pp.213-231, 1987.
10. H.L. Wong and J.E. Luco, "Impedance Functions for Rectangular Foundations on a Uniform Viscoelastic Half-space," *J. Geotechnical Engineering, ASCE*, submitted for publication.
11. J.E. Luco and H.L. Wong, "Response of Hemispherical Foundation Embedded in Half-Space," *J. Engineering Mechanics, ASCE*, **112**, No. 12, pp.1363-1374, Dec. 1986.
12. H.L. Wong and J.E. Luco, "Tables of Impedance Functions for Square Foundations on Layered Media," *Soil Dynamics and Earthquake Engineering*, **4**, No.2, pp.64-81, 1985.
13. C-H. Chen and J. Penzien, "Dynamic Modelling of Axisymmetric Foundations," *Earthquake Engineering and Structural Dynamics*, **14**), pp.823-840, 1986.
14. J. Dominguez, "Dynamic Stiffness of Rectangular Foundations," *Research Report R78-20*, Dept. of Civil Engineering, MIT, Cambridge, MA, 1978.
15. J.M. Emperador and J. Dominguez, "Dynamic Response of Axisymmetric Embedded Foundations," *Earthquake Engineering and Structural Dynamics*, **18**, pp.1105-1117, 1989.
16. A.P. Gaitanaros and D.L. Karabalis, "Dynamic Analysis of 3-D Flexible Embedded Foundations by a Frequency Domain BEM-FEM," *Earthquake Engineering and Structural Dynamics*, **16**, pp.653-674, 1988.

17. F.J. Rizzo, D.J. Shippy and M. Rezayat, "A Boundary Integral Equation Method for Time-harmonic Radiation and Scattering in an Elastic Half-space," *Advanced Topics in Boundary Element Analysis*, ASME, AMD, 72, pp.83-90, 1985.
18. F.J. Rizzo, D.J. Shippy and M. Rezayat, "Boundary Integral Equation Analysis for a Class of Earth-Structure Interaction Problems," *Final Report*, Dept. Eng. Mechanics, Univ. of Kentucky, Lexington, Kentucky, 1985.
19. D.L. Karabalis and D.E. Beskos, "Dynamic Response of 3-D Embedded Foundations by The Boundary Element Method," *Computer Methods in Applied Mechanics and Engineering*, 56, pp.91-119, 1986.
20. M.J. Kaldjian, "Torsional Stiffness of Embedded Footings," *Soil Mech. Found. Div., ASCE*, 95, No.SM1, pp.969-980, 1969.
21. C.M. Ulrich and R.L. Kuhlemeyer, "Coupled Rocking and Lateral Vibrations of Embedded Footings," *Can. Geotech.*, 10, 2, pp.145-160, 1973.
22. E. Kausel, J.M. Roesset and G. Waas, "Dynamic Analysis of Footings on Layered Media," *J. Engineering Mechanics, ASCE*, 101, No.EM5, pp.679-693, 1975.
23. E. Kausel and J.M. Roesset, "Dynamic Stiffness of Circular Foundations," *J. Engineering Mechanics, ASCE*, 101, No.EM6, pp.771-785, 1975.
24. S.M. Day, "Finite Element Analysis of Seismic Scattering Problems," *Ph.D. Dissertation*, University of California, San Diego, CA, 1977.
25. V.W-S. Lee, "Investigation of Three-Dimensional Soil-Structure Interaction," *Report CE 79-11*, Dept. of Civil Engineering, University of Southern California, Los Angeles, CA, 1979.
26. Y.K. Chow and I.M. Smith, "Infinite Elements for Dynamic Foundation Analysis," *Numerical Methods in Geomechanics*, (Ed. Z. Eisenstein), 1, pp.15-22, 1982.
27. F. Medina and J. Penzien, "Infinite Elements for Elastodynamics," *Earthquake Engineering and Structural Dynamics*, 10, pp.699-709, 1982.
28. S. Gupta, J. Penzien, T.W. Lin and C.S. Yeh, "Three-Dimensional Hybrid Modelling of Soil-Structure Interaction," *Earthquake Engineering and Structural Dynamics*, 10, pp.69-87, 1982.
29. A. Mita and W. Takanashi, "Dynamic Soil-Structure Interaction Analysis by Hybrid Method," *Boundary Elements*, C.A. Brebbia, T. Futagami and M. Tanaka, Eds., pp.785-794, 1983.
30. J.E. Luco, "Linear Soil-structure Interaction: A Review," *Earthquake Ground Motion And Its Effects on Structures*, AMD-Vol. 53, S.K. Datta (Ed.). American Society of Mechanical Engineers, New York, pp.41-57, 1982.
31. D.E. Beskos, "Boundary Element Methods in Dynamic Analysis," *Applied Mechanics Reviews*, 40, 1, pp.1-23, 1987.
32. F. Hartmann, "Computing the C-matrix in non-smooth boundary points," *New Developments in Boundary Element Methods*, (Ed. by C.A. Brebbia), CML Publications, pp.367-379, 1980.
33. K.F. Graff, *Wave Motion in Elastic Solids*, Ohio State University Press, 1975.
34. Pei-cheng Xu and A.K. Mal, "An Adaptive Integration Scheme for Irregularly Oscillatory Functions," *Wave Motion*, 7, pp.235-243, 1985.

NOTATION.

a_o	non-dimensional frequency defined by $a_o = \omega L / \bar{c}_s$
a_p	$= \sqrt{k^2 - k_p^2}$
a_s	$= \sqrt{k^2 - k_s^2}$
[A]	square coefficient matrix for the boundary element system (equation 29)
[\tilde{A}]	$3 \times 3M_n$ matrix assembled from the integrals of the products of $[F]^T$ and $[N]$ associated with a single source point (equation 25)
b	width of a foundation or half-width of a footing
[B]	matrix assembled from $[\tilde{B}]$ (equation 30)
[\tilde{B}]	$3 \times 3M_i$ matrix assembled from the integrals of the products of $[G]^T$ and $[\tilde{H}]$ associated with a single source point (equation 26)
[B_G], [B_H]	matrices for the decomposed expression of matrix [B]
c	$= \omega / k$
c_p	P wave velocity including damping
\bar{c}_p	P wave velocity without damping
c_r	Rayleigh wave velocity including damping
\bar{c}_r	Rayleigh wave velocity without damping
c_s	shear wave velocity including damping
\bar{c}_s	shear wave velocity without damping
[$C(\vec{x})$]	3×3 matrix related to the geometric shape of the boundary at \vec{x} (equation 14)
\bar{d}	$= \sqrt{(y - y_o)^2 + (z - z_o)^2}$, distance between source and receiver points projected on plane $x = 0$
[\tilde{D}]	3×3 diagonal matrix defined by $[\tilde{D}] = \text{diag}(1, -1, -1)$
[D], [D_1]	diagonal matrices consisting of $[\tilde{D}]$ (Appendix B)
[E]	$3 \times 3M_i$ matrix relating the Fourier transform of the displacements to the nodal tractions at Γ_i (equation 35)
[f]	flexibility influence matrix
[\tilde{f}]	$3 \times 3M_i$ matrix through which nodal displacements on Γ_i are expressed in terms of $\{T\}$

$[F]$	transformed Green's traction functions (equation 11b)
$[F^*]$	full-space Green's traction functions
$g(k)$	$= (2k^2 - k_s^2)^2 - 4k^2(k^2 - k_p^2)^{1/2}(k^2 - k_s^2)^{1/2}$, Rayleigh function
$[G]$	transformed Green's displacement functions (equation 11a)
$[G^*]$	full-space Green's displacement functions
$[h()]$	matrix of interpolation functions for two-dimensional elements on Γ_i
$[\bar{h}()]$	Fourier transform of the two-dimensional interpolation functions
$[h_1], [h_2]$	matrices enlarged from matrices $\{\bar{\psi}\}$ and $[\Psi]^{-1}$ (Appendix A)
$[\bar{H}()]$	matrix assembled from $[\bar{h}()]$
i	$= \sqrt{-1}$
I_1, I_2	integration of the test function $\phi(k)$ over an interval
k	wavenumber in x -direction
k_q	q th sampling point in the k wavenumber domain
k_r	Rayleigh wavenumber
k_s	shear wavenumber
k_1, k_2	values in the wavenumber domain
K	integration limit in the k wavenumber domain at which the infinite integral of equation (6) is truncated
$K_0(), K_1()$	modified Bessel functions of second kind of order zero and order one
l	length of an element on $\bar{\Gamma}_c \cup \bar{\Gamma}_h$
L	half width of a two dimensional canyon
L_x	discretization range along the direction of canyon axis for three dimensional boundary element approach
L_y	discretization range on the half-space surface
M	number of one-dimensional elements on the boundaries $\bar{\Gamma}_c \cup \bar{\Gamma}_h$
\bar{M}	number of nodes on an element
M_g	number of Gauss integration points on $\bar{\Gamma}_c$
M_i	number of nodes on the dam-foundation rock interface Γ_i

M_n	number of nodes on the boundaries $\bar{\Gamma}_c \cup \bar{\Gamma}_h$
M_1, M_2	element number for the first and the last one-dimensional elements on boundary $\bar{\Gamma}_c$
n, n_1, n_2, n_3	outgoing normal to the boundary and its components
$[N]; N_j$	shape function matrix for the one-dimensional element on $\bar{\Gamma}_c \cup \bar{\Gamma}_h$; j th shape function
$\{P\}, P_x, P_y, P_z$	vector and components of concentrated forces associated with the second elastodynamic state
$\{\bar{r}\}$	vector of nodal displacements at the dam-foundation rock interface
$\{\bar{r}_o\}$	6×1 vector containing the six degrees of freedom for a rigid foundation
r_s	radius of the circular contour around a source point in plane $x = 0$
$\{\bar{R}\}$	vector of nodal forces at the dam-foundation rock interface Γ_i
$\{\hat{S}\}$	unsymmetric impedance matrix resulted from boundary element approximations
$[S_j]$	impedance matrix
$[S_r]$	impedance matrix for a rigid foundation
$S_{xx}, S_{yy}, S_{zz}, S_{rr}$	
$S_{tt}, S_{mm}, S_{xm}, S_{yr}$	non-dimensional impedance coefficients for rigid foundation
t	time
$\{t\}; t_x, t_y, t_z$	traction vector and its components
$\{\bar{t}\}; \bar{t}_x, \bar{t}_y, \bar{t}_z$	vector of Fourier transform of the surface tractions and its components
$\{T\}$	vector of nodal tractions
$\{T_x\}, \{T_y\}, \{T_z\}$	vector containing the x -, y -, and z -components of nodal tractions
$\{u\}$	displacement vector
$\{\bar{u}\}$	Fourier transform of the displacement vector $\{u\}$
$\{\bar{U}\}, \bar{U}_{xj}, \bar{U}_{yj}, \bar{U}_{zj}$	vector containing nodal displacements at plane $x = 0$ and its components at the j th node
W_q	weighting coefficients associated with the integration scheme used in k wavenumber domain
x, y, z	spatial coordinates

x', y', z'	spatial coordinates in $x'y'z'$ -coordinate system
x_c, y_c, z_c	coordinates of a point inside an element on Γ_i
x_s, y_s, z_s	spatial coordinates of source point
\bar{x}	$= (x, y, z)$, an arbitrary point
\bar{x}'	a point in $x'y'z'$ -coordinate system
\bar{x}_0	$= (0, y, z)$, an arbitrary point at plane $x = 0$
\bar{x}_{0s}	$= (0, y_s, z_s)$, source point at plane $x = 0$
$[\alpha]$	$3M_i \times 6$ matrix relating nodal displacements on Γ_i with the six rigid-body degrees of freedom of a rigid foundation
Γ_c	canyon surface
$\bar{\Gamma}_c$	cross-section of the canyon at plane $x = 0$
Γ_h	half-space surface
$\bar{\Gamma}_h$	cross-section of the half-space surface at plane $x = 0$
Γ_i	dam-foundation rock interface
$\bar{\Gamma}_j$	extent of the j th element
$\bar{\Gamma}_s$	small contour of radius r_s around the source point at plane $x = 0$
δ	positive number
δ_{nj}	Kronecker delta function
ζ	natural coordinate
η_p	constant hysteretic damping factor for P wave
η_r	constant hysteretic damping factor for Rayleigh wave
η_s	constant hysteretic damping factor for shear wave
λ_s	shear wavelength
μ	shear modulus for the half-space medium
ν	Poisson's ratio for the half-space medium
$\phi()$	test function defined in equation (49)
$[\Phi]$	matrix that transforms distributing tractions into concentrated nodal forces (equation 41)
$\{\psi\}$	row matrix defined in equation (A.3)

$\{\bar{\psi}\}; \bar{\psi}_j$ Fourier transform of $\{\psi\}$ and its j th component
 $[\Psi]$ square matrix defined in equation (A.4)
 ω frequency in rad/sec.

APPENDIX A: FOURIER TRANSFORMS OF TWO-DIMENSIONAL SHAPE FUNCTIONS

First, consider a two-dimensional curved 8 node element at the dam-foundation rock interface Γ_i (Figure A.1) where any point, \bar{x} , on the element can be uniquely represented by two local coordinates $\bar{x}' = (x', y')$ (or (x', z') if the element is on a vertical plane). The local and the global coordinate systems are related through

$$x = x_c + x' \quad (A.1a)$$

$$y = y_c + y' \quad (A.1b)$$

where (x_c, y_c) are the global coordinates of a point inside the element.

As described in the main text, the prescribed traction, $\{t(\bar{x})\}$, contains the x , y and z components. For the purpose of illustration, consider the x component, $t_x(\bar{x})$, first. At any point \bar{x}' on the element, the traction $t_x(\bar{x}')$ can be expressed in terms of tractions at all the nodal points, \bar{x}'_i , $i=1, \dots, 8$:

$$t_x(\bar{x}') = \{\psi(\bar{x}')\}[\Psi]^{-1}\{T_x\} \quad (A.2)$$

where

$$\{\psi(\bar{x}')\} = \{1, x', y', x'^2, x'y', y'^2, x'^2y', x'y'^2\} \quad (A.3)$$

$$[\Psi] = \begin{pmatrix} \{\psi(\bar{x}'_1)\} \\ \vdots \\ \{\psi(\bar{x}'_8)\} \end{pmatrix} \quad (A.4)$$

and $\{T_x\} = \{T_{x1}, \dots, T_{x8}\}^T$ is a vector containing the x -components of the nodal tractions at \bar{x}'_i , $i=1, \dots, 8$.

Utilizing equations (A.1) and (A.2), the Fourier transform of $t_x(\bar{x})$ can be found to be

$$\bar{t}_x(\bar{x}_o, k) = \frac{1}{2\pi} \int_{-\infty}^{\infty} t_x(\bar{x}) e^{ikx} dx$$

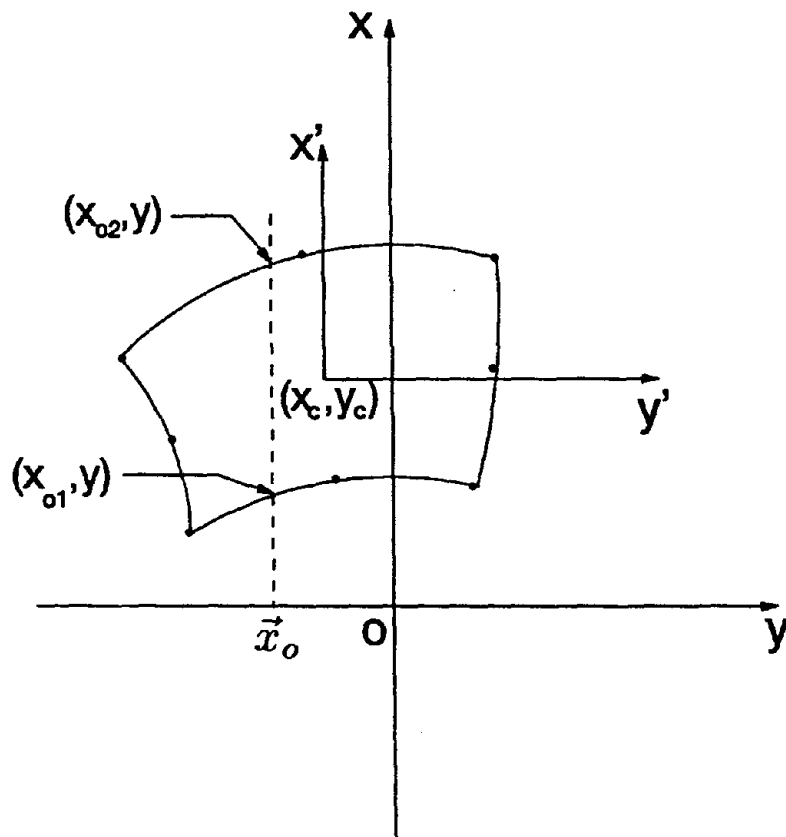


Fig.A.1 Top view of an arbitrary element on dam-foundation interface.

$$\begin{aligned}
&= \frac{1}{2\pi} \int_{x_{o1}}^{x_{o2}} t_x(\vec{x}) e^{ikx} dx \\
&= \frac{1}{2\pi} e^{ikx_c} \int_{x_{o1}-x_c}^{x_{o2}-x_c} \{\psi(\vec{x}')\} e^{ikx'} dx' [\Psi]^{-1} \{T_x\} \\
&= \{\bar{\psi}\} [\Psi]^{-1} \{T_x\}
\end{aligned} \tag{A.5}$$

where x_{o1} and x_{o2} are the global x -coordinates of the points (Figure A.1) at the element boundary intersected by a line parallel to the x -axis passing through $\vec{x}' = (0, y')$. In equation (A.5), $\{\bar{\psi}\}$ is a 1×8 matrix containing the Fourier transforms of $\{\psi(\vec{x}')\}$

$$\begin{aligned}
\{\bar{\psi}\} &= \frac{1}{2\pi} e^{ikx_c} \int_{x_{o1}-x_c}^{x_{o2}-x_c} \{\psi(\vec{x}')\} e^{ikx'} dx' \\
&= \{\bar{\psi}_1, \bar{\psi}_2, \bar{\psi}_3, \bar{\psi}_4, \bar{\psi}_5, \bar{\psi}_6, \bar{\psi}_7, \bar{\psi}_8\}
\end{aligned} \tag{A.6}$$

where

$$\begin{aligned}
\bar{\psi}_1 &= -\frac{1}{2\pi} \frac{i}{k} (e^{ikx_{o2}} - e^{ikx_{o1}}) \\
\bar{\psi}_2 &= \frac{1}{2\pi} \left[-\frac{i}{k} (x_{o2} - x_c) + \frac{1}{k^2} \right] e^{ikx_{o2}} + \frac{1}{2\pi} \left[\frac{i}{k} (x_{o1} - x_c) - \frac{1}{k^2} \right] e^{ikx_{o1}} \\
\bar{\psi}_3 &= \bar{\psi}_1 y' \\
\bar{\psi}_4 &= \frac{1}{2\pi} e^{ikx_{o2}} \left[\frac{1}{ik} (x_{o2} - x_c)^2 + \frac{2}{k^2} (x_{o2} - x_c) + \frac{2i}{k^3} \right] \\
&\quad - \frac{1}{2\pi} e^{ikx_{o1}} \left[\frac{1}{ik} (x_{o1} - x_c)^2 + \frac{2}{k^2} (x_{o1} - x_c) + \frac{2i}{k^3} \right] \\
\bar{\psi}_5 &= \bar{\psi}_2 y' \\
\bar{\psi}_6 &= \bar{\psi}_1 y'^2 \\
\bar{\psi}_7 &= \bar{\psi}_4 y' \\
\bar{\psi}_8 &= \bar{\psi}_2 y'^2
\end{aligned}$$

Similarly, the Fourier transforms of the prescribed tractions in the y and z directions can be expressed as

$$\bar{i}_y(\vec{x}_o, k) = \{\bar{\psi}\} [\Psi]^{-1} \{T_y\} \tag{A.7}$$

$$\bar{t}_z(\bar{x}_o, k) = \{\bar{\psi}\}[\Psi]^{-1}\{T_z\} \quad (A.8)$$

where $\{T_y\}$ and $\{T_z\}$ are the y and z components of the nodal tractions, respectively.

Combining equations (A.5), (A.7) and (A.8) leads to the expression for the 3×24 matrix $[\bar{h}(\bar{x}_o, k)]$ (equation 19) for the 8 node element

$$[\bar{h}(\bar{x}_o, k)] = [h_1][h_2] \quad (A.9)$$

where $[h_1]$ is a 3×24 matrix enlarged from matrix $\{\bar{\psi}\}$ by replacing each entry in $\{\bar{\psi}\}$ by a 3×3 diagonal matrix $diag[\bar{\psi}_i, \bar{\psi}_i, \bar{\psi}_i]$, $i = 1, \dots, 8$; and $[h_2]$ is a 24×24 matrix enlarged from matrix $[\Psi]^{-1}$ in a similar manner.

For 4 and 6 node elements, the solution procedure is the same except that $\{\psi(\bar{x}')\}$ in equation (A.3) is replaced by $\{\psi(\bar{x}')\} = \{1, x', y', x'y'\}$ for 4 node element, and by $\{\psi(\bar{x}')\} = \{1, x', y', x'^2, x'y', y'^2\}$ for 6 node element.

APPENDIX B: RELATION BETWEEN $\{\bar{U}\}_k$ AND $\{\bar{U}\}_{-k}$

As mentioned in the procedure summary, the computations to determine the nodal displacements $\{\bar{U}\}$ are repeated for a discrete set of wavenumbers over a truncated wavenumber range $(-K, K)$. Due to a special property of the integrands with respect to k , however, $\{\bar{U}\}$ for negative wavenumbers can be obtained indirectly from $\{\bar{U}\}$ corresponding to positive wavenumbers. From Appendix C in Part I, the transformed Green's functions $[G]$ and $[\bar{F}]$ corresponding to negative wavenumber $-k$ can be expressed as

$$[G(\bar{x}_o, \bar{x}_{os}, -k)] = [\tilde{D}][G(\bar{x}_o, \bar{x}_{os}, k)][\tilde{D}] \quad (B.1a)$$

$$[\bar{F}(\bar{x}_o, \bar{x}_{os}, -k)] = [\tilde{D}][\bar{F}(\bar{x}_o, \bar{x}_{os}, k)][\tilde{D}] \quad (B.1b)$$

where $[\tilde{D}]$ is a 3×3 diagonal matrix given by

$$[\tilde{D}] = \text{diag}(1, -1, -1) \quad (B.2)$$

Thus, the coefficient matrix $[A(k)]$ in equation (28), which consists of the integrals of the products of the transformed traction Green's functions $[\bar{F}]$ and the one-dimensional interpolation functions, has the property that

$$[A(-k)] = [D][A(k)][D] \quad (B.3)$$

where $[D]$ is a diagonal matrix of order $3M_n$

$$[D] = \text{diag}(1, -1, -1, 1, -1, -1, \dots, 1, -1, -1) \quad (B.4)$$

From equation (B.3), it is apparent that

$$[A(-k)]^{-1} = [D][A(k)]^{-1}[D] \quad (B.5)$$

since $[D]^{-1} = [D]$.

The matrix $[B(k)]$ in equation (28) consists of the integrals of the products of $[G]$, the transformed displacement Green's functions, and $[\bar{H}(\bar{x}_o, k)]$, the Fourier transforms

of the two-dimensional interpolation functions on the dam-foundation rock interface Γ ; (equations 26 and 30). These integrals are evaluated numerically over each elements on $\bar{\Gamma}_c$ through Gauss integration scheme. Since $[\bar{H}(\bar{x}_o, k)]$ does not depend on the source point \bar{x}_{os} , matrix $[B(k)]$ can be decomposed as

$$[B(k)] = [B_G(k)][B_H(k)] \quad (B.6)$$

where matrix $[B_G(k)]$ consists of the transformed displacement Green's functions associated with different source points \bar{x}_{os} and receiver points \bar{x}_o , i.e. the Gauss integration points; and matrix $[B_H(k)]$ consists of $[\bar{H}(\bar{x}_o, k)]$ for various receiver points. The sizes of $[B_G(k)]$ and $[B_H(k)]$ depend on the total number of Gauss integration points on $\bar{\Gamma}_c$. If the total number of Gauss integration points on $\bar{\Gamma}_c$ is M_g , the sizes for $[B_G(k)]$ and $[B_H(k)]$ are $3M_n \times 3M_g$ and $3M_g \times 3M_i$, respectively. Due to the relation given in equation (B.1a) and the fact that $[\bar{H}(\bar{x}_o, -k)]$ is complex conjugate of $[\bar{H}(\bar{x}_o, k)]$, matrix $[B(k)]$ apparently has the property that

$$[B(-k)] = [D][B_G(k)][D_1]conjg([B_H(k)]) \quad (B.7)$$

where $[D_1]$ is a square diagonal matrix of dimension $3M_g$ having similar form as $[D]$ in equation (B.4).

Thus, from equation (31), the nodal displacements on the boundary $\bar{\Gamma}_c \cup \bar{\Gamma}_h$ are given by

$$\{\bar{U}\}_k = [A(k)]^{-1}[B_G(k)][B_H(k)]\{T\} \quad (B.8)$$

for positive wavenumber k and

$$\{\bar{U}\}_{-k} = [D][A(k)]^{-1}[B_G(k)][D_1]conjg([B_H(k)])\{T\} \quad (B.9)$$

for negative wavenumber $-k$. Once $[A(k)]^{-1}[B_G(k)]$ is found, both $\{\bar{U}\}_k$ and $\{\bar{U}\}_{-k}$ can be determined easily.

In general, it is more computationally efficient to use equations (B.8) and (B.9), instead of equation (31), to solve for the nodal displacements $\{\bar{U}\}$ on the boundaries

$\bar{\Gamma}_c \cup \bar{\Gamma}_h$ for both k and $-k$, especially when the total number of nodes on Γ_i is greater than the total number of Gauss integration points on $\bar{\Gamma}_c$, i.e. $M_i > M_g$. Since the computation of $[A(k)]^{-1}[B_G(k)]$ does not depend on the nodal distribution at Γ_i along the x -direction, the computational cost for the present method does not increase much when the number of nodes at Γ_i increases along the x -direction. Therefore, the present method is especially efficient when the number of DOF along the canyon axis is relatively large.

APPENDIX C: RESTRICTIONS ON MESH LAYOUT ON $\bar{\Gamma}_c$

Two types of discretization are involved in the present method. One is the discretization of $\bar{\Gamma}_c \cup \bar{\Gamma}_h$, the system cross-section at $x = 0$, into one-dimensional line elements and the other is the discretization of the dam-foundation rock interface, Γ_i , into two-dimensional surface elements. In order to avoid singularity problem in the flexibility matrix, there is a certain restriction on the relative relation between the two types of discretization.

In order to illustrate the restriction, consider a simple example shown in Figure C.1 where a banded foundation of constant width is resting on a semi-circular canyon. In this example, $\bar{\Gamma}_c$ is discretized evenly into 4 line elements with the left most node being the m th node and Γ_i is discretized evenly into 8 elements along the circumferential direction. From equation (33), the nodal displacements, $\{\bar{r}\}$, on Γ_i is determined by superposing the Fourier transforms $\{\bar{u}(\bar{x}_{oj}, k_q)\}$ at $\bar{\Gamma}_c$, where $\{\bar{u}(\bar{x}_{oj}, k_q)\}$ is determined from their nodal values through equation (34). Thus, for this particular example, the displacements at the first three nodes on Γ_i are given by

$$\{\bar{r}\}_1 = \sum_q W_q [N_1(\zeta_1)\{\bar{U}_q\}_m + N_2(\zeta_1)\{\bar{U}_q\}_{m+1}]e^{-ik_q x_1} \quad (C.1)$$

$$\{\bar{r}\}_2 = \sum_q W_q [N_1(\zeta_2)\{\bar{U}_q\}_m + N_2(\zeta_2)\{\bar{U}_q\}_{m+1}]e^{-ik_q x_2} \quad (C.2)$$

$$\{\bar{r}\}_3 = \sum_q W_q [N_1(\zeta_3)\{\bar{U}_q\}_m + N_2(\zeta_3)\{\bar{U}_q\}_{m+1}]e^{-ik_q x_3} \quad (C.3)$$

where ζ_1 , ζ_2 and ζ_3 are the corresponding natural coordinates for the three nodes.

Since $x_1 = x_2 = x_3$, it is clear that these nodal displacements can be expressed in matrix form as

$$\begin{pmatrix} \{\bar{r}\}_1 \\ \{\bar{r}\}_2 \\ \{\bar{r}\}_3 \end{pmatrix} = \begin{pmatrix} N_1(\zeta_1) & N_2(\zeta_1) \\ N_1(\zeta_2) & N_2(\zeta_2) \\ N_1(\zeta_3) & N_2(\zeta_3) \end{pmatrix} \begin{pmatrix} \sum_q W_q \{\bar{U}_q\}_m e^{-ik_q x_1} \\ \sum_q W_q \{\bar{U}_q\}_{m+1} e^{-ik_q x_1} \end{pmatrix} \quad (C.4)$$

Because the second matrix on the right hand side of equation (C.4) is a linear combination of the nodal tractions, $\{T\}$ (see equation 35), equation (C.4) implies that

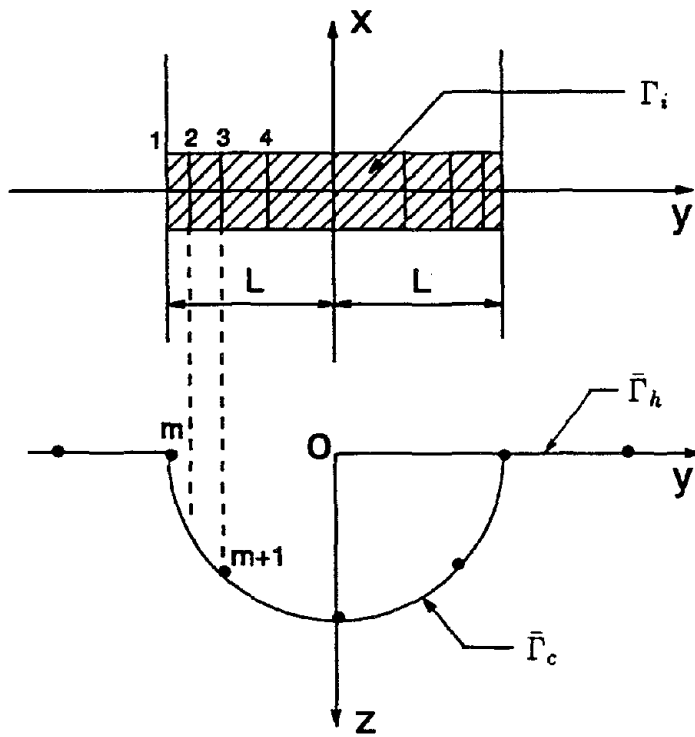


Fig.C.1 Illustration of inappropriate mesh that will lead to singular flexibility influence matrix.

the first three rows in the flexibility influence matrix $[f]$ (equations 38 and 39) is a linear combination of two rows. Thus the rank of the first three rows is less than 3 which means that the resulting flexibility influence matrix is singular.

From this example, it is clear that, in order to avoid singularity or ill-condition problem in the flexibility influence matrix, the size of the elements on $\bar{\Gamma}_c$ should be smaller than or about the same as that of elements on Γ_i . More specifically, situations similar to the example just illustrated, where three or more nodes having the same x -coordinates on Γ_i fall in one element on $\bar{\Gamma}_c$, should be avoided.

EARTHQUAKE ENGINEERING RESEARCH CENTER REPORT SERIES

EERC reports are available from the National Information Service for Earthquake Engineering(NISEE) and from the National Technical Information Service(NTIS). Numbers in parentheses are Accession Numbers assigned by the National Technical Information Service; these are followed by a price code. Contact NTIS, 5285 Port Royal Road, Springfield Virginia, 22161 for more information. Reports without Accession Numbers were not available from NTIS at the time of printing. For a current complete list of EERC reports (from EERC 67-1) and availability information, please contact University of California, EERC, NISEE, 1301 South 46th Street, Richmond, California 94804.

- UCB/EERC-81/01 "Control of Seismic Response of Piping Systems and Other Structures by Base Isolation," by Kelly, J.M., January 1981, (PB81 200 735)A05.
- UCB/EERC-81/02 "OPTNSR- An Interactive Software System for Optimal Design of Statically and Dynamically Loaded Structures with Nonlinear Response," by Bhatti, M.A., Ciampi, V. and Pister, K.S., January 1981, (PB81 218 851)A09.
- UCB/EERC-81/03 "Analysis of Local Variations in Free Field Seismic Ground Motions," by Chen, J.-C., Lysmer, J. and Seed, H.B., January 1981, (AD-A099508)A13.
- UCB/EERC-81/04 "Inelastic Structural Modeling of Braced Offshore Platforms for Seismic Loading," by Zayas, V.A., Shing, P.-S.B., Mahin, S.A. and Popov, E.P., January 1981, INEL4, (PB82 138 777)A07.
- UCB/EERC-81/05 "Dynamic Response of Light Equipment in Structures," by Der Kiureghian, A., Sackman, J.L. and Nour-Omid, B., April 1981, (PB81 218 497)A04.
- UCB/EERC-81/06 "Preliminary Experimental Investigation of a Broad Base Liquid Storage Tank," by Bouwkamp, J.G., Kollegger, J.P. and Stephen, R.M., May 1981, (PB82 140 385)A03.
- UCB/EERC-81/07 "The Seismic Resistant Design of Reinforced Concrete Coupled Structural Walls," by Aktan, A.E. and Bertero, V.V., June 1981, (PB82 113 358)A11.
- UCB/EERC-81/08 "Unassigned," by Unassigned, 1981.
- UCB/EERC-81/09 "Experimental Behavior of a Spatial Piping System with Steel Energy Absorbers Subjected to a Simulated Differential Seismic Input," by Stiemeier, S.F., Godden, W.G. and Kelly, J.M., July 1981, (PB82 201 898)A04.
- UCB/EERC-81/10 "Evaluation of Seismic Design Provisions for Masonry in the United States," by Sveinsson, B.I., Mayes, R.L. and McNiven, H.D., August 1981, (PB82 166 075)A08.
- UCB/EERC-81/11 "Two-Dimensional Hybrid Modelling of Soil-Structure Interaction," by Tzong, T.-J., Gupta, S. and Penzien, J., August 1981, (PB82 142 118)A04.
- UCB/EERC-81/12 "Studies on Effects of Infills in Seismic Resistant R/C Construction," by Brokken, S. and Bertero, V.V., October 1981, (PB82 166 190)A09.
- UCB/EERC-81/13 "Linear Models to Predict the Nonlinear Seismic Behavior of a One-Story Steel Frame," by Valdimarsson, H., Shah, A.H. and McNiven, H.D., September 1981, (PB82 138 793)A07.
- UCB/EERC-81/14 "TLUSH: A Computer Program for the Three-Dimensional Dynamic Analysis of Earth Dams," by Kagawa, T., Mejia, L.H., Seed, H.B. and Lysmer, J., September 1981, (PB82 139 940)A06.
- UCB/EERC-81/15 "Three Dimensional Dynamic Response Analysis of Earth Dams," by Mejia, L.H. and Seed, H.B., September 1981, (PB82 137 274)A12.
- UCB/EERC-81/16 "Experimental Study of Lead and Elastomeric Dampers for Base Isolation Systems," by Kelly, J.M. and Hodder, S.B., October 1981, (PB82 166 182)A05.
- UCB/EERC-81/17 "The Influence of Base Isolation on the Seismic Response of Light Secondary Equipment," by Kelly, J.M., April 1981, (PB82 255 266)A04.
- UCB/EERC-81/18 "Studies on Evaluation of Shaking Table Response Analysis Procedures," by Blondet, J. M., November 1981, (PB82 197 278)A10.
- UCB/EERC-81/19 "DELIGHT.STRUCT: A Computer-Aided Design Environment for Structural Engineering," by Balling, R.J., Pister, K.S. and Polak, E., December 1981, (PB82 218 496)A07.
- UCB/EERC-81/20 "Optimal Design of Seismic-Resistant Planar Steel Frames," by Balling, R.J., Ciampi, V. and Pister, K.S., December 1981, (PB82 220 179)A07.
- UCB/EERC-82/01 "Dynamic Behavior of Ground for Seismic Analysis of Lifeline Systems," by Sato, T. and Der Kiureghian, A., January 1982, (PB82 218 926)A05.
- UCB/EERC-82/02 "Shaking Table Tests of a Tubular Steel Frame Model," by Ghanaat, Y. and Clough, R.W., January 1982, (PB82 220 161)A07.
- UCB/EERC-82/03 "Behavior of a Piping System under Seismic Excitation: Experimental Investigations of a Spatial Piping System supported by Mechanical Shock Arrestors," by Schneider, S., Lee, H.-M. and Godden, W. G., May 1982, (PB83 172 544)A09.
- UCB/EERC-82/04 "New Approaches for the Dynamic Analysis of Large Structural Systems," by Wilson, E.L., June 1982, (PB83 148 080)A05.
- UCB/EERC-82/05 "Model Study of Effects of Damage on the Vibration Properties of Steel Offshore Platforms," by Shahrivar, F. and Bouwkamp, J.G., June 1982, (PB83 148 742)A10.
- UCB/EERC-82/06 "States of the Art and Practice in the Optimum Seismic Design and Analytical Response Prediction of R/C Frame Wall Structures," by Aktan, A.E. and Bertero, V.V., July 1982, (PB83 147 736)A05.
- UCB/EERC-82/07 "Further Study of the Earthquake Response of a Broad Cylindrical Liquid-Storage Tank Model," by Manos, G.C. and Clough, R.W., July 1982, (PB83 147 744)A11.
- UCB/EERC-82/08 "An Evaluation of the Design and Analytical Seismic Response of a Seven Story Reinforced Concrete Frame," by Charney, F.A. and Bertero, V.V., July 1982, (PB83 157 628)A09.
- UCB/EERC-82/09 "Fluid-Structure Interactions: Added Mass Computations for Incompressible Fluid," by Kuo, J.S.-H., August 1982, (PB83 156 281)A07.
- UCB/EERC-82/10 "Joint-Opening Nonlinear Mechanism: Interface Smeared Crack Model," by Kuo, J.S.-H., August 1982, (PB83 149 195)A05.

- UCB/EERC-82/11 "Dynamic Response Analysis of Techi Dam," by Clough, R.W., Stephen, R.M. and Kuo, J.S.-H., August 1982, (PB83 147 496)A06.
- UCB/EERC-82/12 "Prediction of the Seismic Response of R/C Frame-Coupled Wall Structures," by Aktan, A.E., Bertero, V.V. and Piazza, M., August 1982, (PB83 149 203)A09.
- UCB/EERC-82/13 "Preliminary Report on the Smart 1 Strong Motion Array in Taiwan," by Bolt, B.A., Loh, C.H., Penzien, J. and Tsai, Y.B., August 1982, (PB83 159 400)A10.
- UCB/EERC-82/14 "Seismic Behavior of an Eccentrically X-Braced Steel Structure," by Yang, M.S., September 1982, (PB83 260 778)A12.
- UCB/EERC-82/15 "The Performance of Stairways in Earthquakes," by Roha, C., Axley, J.W. and Bertero, V.V., September 1982, (PB83 157 693)A07.
- UCB/EERC-82/16 "The Behavior of Submerged Multiple Bodies in Earthquakes," by Liao, W.-G., September 1982, (PB83 158 709)A07.
- UCB/EERC-82/17 "Effects of Concrete Types and Loading Conditions on Local Bond-Slip Relationships," by Cowell, A.D., Popov, E.P. and Bertero, V.V., September 1982, (PB83 153 577)A04.
- UCB/EERC-82/18 "Mechanical Behavior of Shear Wall Vertical Boundary Members: An Experimental Investigation," by Wagner, M.T. and Bertero, V.V., October 1982, (PB83 159 764)A05.
- UCB/EERC-82/19 "Experimental Studies of Multi-support Seismic Loading on Piping Systems," by Kelly, J.M. and Cowell, A.D., November 1982, (PB90 262 684)A07.
- UCB/EERC-82/20 "Generalized Plastic Hinge Concepts for 3D Beam-Column Elements," by Chen, P. F.-S. and Powell, G.H., November 1982, (PB83 247 981)A13.
- UCB/EERC-82/21 "ANSR-II: General Computer Program for Nonlinear Structural Analysis," by Oughourlian, C.V. and Powell, G.H., November 1982, (PB83 251 330)A12.
- UCB/EERC-82/22 "Solution Strategies for Statically Loaded Nonlinear Structures," by Simons, J.W. and Powell, G.H., November 1982, (PB83 197 970)A06.
- UCB/EERC-82/23 "Analytical Model of Deformed Bar Anchorages under Generalized Excitations," by Ciampi, V., Eligehausen, R., Bertero, V.V. and Popov, E.P., November 1982, (PB83 169 532)A06.
- UCB/EERC-82/24 "A Mathematical Model for the Response of Masonry Walls to Dynamic Excitations," by Sucuoglu, H., Mengi, Y. and McNiven, H.D., November 1982, (PB83 169 011)A07.
- UCB/EERC-82/25 "Earthquake Response Considerations of Broad Liquid Storage Tanks," by Cambra, F.J., November 1982, (PB83 251 215)A09.
- UCB/EERC-82/26 "Computational Models for Cyclic Plasticity, Rate Dependence and Creep," by Mosaddad, B. and Powell, G.H., November 1982, (PB83 245 829)A08.
- UCB/EERC-82/27 "Inelastic Analysis of Piping and Tubular Structures," by Mahasuverachai, M. and Powell, G.H., November 1982, (PB83 249 987)A07.
- UCB/EERC-83/01 "The Economic Feasibility of Seismic Rehabilitation of Buildings by Base Isolation," by Kelly, J.M., January 1983, (PB83 197 988)A05.
- UCB/EERC-83/02 "Seismic Moment Connections for Moment-Resisting Steel Frames," by Popov, E.P., January 1983, (PB83 195 412)A04.
- UCB/EERC-83/03 "Design of Links and Beam-to-Column Connections for Eccentrically Braced Steel Frames," by Popov, E.P. and Malley, J.O., January 1983, (PB83 194 811)A04.
- UCB/EERC-83/04 "Numerical Techniques for the Evaluation of Soil-Structure Interaction Effects in the Time Domain," by Bayo, E. and Wilson, E.L., February 1983, (PB83 245 605)A09.
- UCB/EERC-83/05 "A Transducer for Measuring the Internal Forces in the Columns of a Frame-Wall Reinforced Concrete Structure," by Sause, R. and Bertero, V.V., May 1983, (PB84 119 494)A06.
- UCB/EERC-83/06 "Dynamic Interactions Between Floating Ice and Offshore Structures," by Croteau, P., May 1983, (PB84 119 486)A16.
- UCB/EERC-83/07 "Dynamic Analysis of Multiply Tuned and Arbitrarily Supported Secondary Systems," by Igusa, T. and Der Kiureghian, A., July 1983, (PB84 118 272)A11.
- UCB/EERC-83/08 "A Laboratory Study of Submerged Multi-body Systems in Earthquakes," by Ansari, G.R., June 1983, (PB83 261 842)A17.
- UCB/EERC-83/09 "Effects of Transient Foundation Uplift on Earthquake Response of Structures," by Yim, C.-S. and Chopra, A.K., June 1983, (PB83 261 396)A07.
- UCB/EERC-83/10 "Optimal Design of Friction-Braced Frames under Seismic Loading," by Austin, M.A. and Pister, K.S., June 1983, (PB84 119 288)A06.
- UCB/EERC-83/11 "Shaking Table Study of Single-Story Masonry Houses: Dynamic Performance under Three Component Seismic Input and Recommendations," by Manos, G.C., Clough, R.W. and Mayes, R.L., July 1983, (UCB/EERC-83/11)A08.
- UCB/EERC-83/12 "Experimental Error Propagation in Pseudodynamic Testing," by Shiing, P.B. and Mahin, S.A., June 1983, (PB84 119 270)A09.
- UCB/EERC-83/13 "Experimental and Analytical Predictions of the Mechanical Characteristics of a 1/5-scale Model of a 7-story R/C Frame-Wall Building Structure," by Aktan, A.E., Bertero, V.V., Chowdhury, A.A. and Nagashima, T., June 1983, (PB84 119 213)A07.
- UCB/EERC-83/14 "Shaking Table Tests of Large-Panel Precast Concrete Building System Assemblages," by Oliva, M.G. and Clough, R.W., June 1983, (PB86 110 210/AS)A11.
- UCB/EERC-83/15 "Seismic Behavior of Active Beam Links in Eccentrically Braced Frames," by Hjelmstad, K.D. and Popov, E.P., July 1983, (PB84 119 676)A09.
- UCB/EERC-83/16 "System Identification of Structures with Joint Rotation," by Dimsdale, J.S., July 1983, (PB84 192 210)A06.
- UCB/EERC-83/17 "Construction of Inelastic Response Spectra for Single-Degree-of-Freedom Systems," by Mahin, S. and Lin, J., June 1983, (PB84 208 834)A05.
- UCB/EERC-83/18 "Interactive Computer Analysis Methods for Predicting the Inelastic Cyclic Behaviour of Structural Sections," by Kaba, S. and Mahin, S., July 1983, (PB84 192 012)A06.
- UCB/EERC-83/19 "Effects of Bond Deterioration on Hysteretic Behavior of Reinforced Concrete Joints," by Filippou, F.C., Popov, E.P. and Bertero, V.V., August 1983, (PB84 192 020)A10.

- UCB/EERC-83/20 "Correlation of Analytical and Experimental Responses of Large-Panel Precast Building Systems," by Oliva, M.G., Clough, R.W., Velkov, M. and Gavrilovic, P., May 1988, (PB90 262 692)A06.
- UCB/EERC-83/21 "Mechanical Characteristics of Materials Used in a 1/5 Scale Model of a 7-Story Reinforced Concrete Test Structure," by Bertero, V.V., Aktan, A.E., Harris, H.G. and Chowdhury, A.A., October 1983, (PB84 193 697)A05.
- UCB/EERC-83/22 "Hybrid Modelling of Soil-Structure Interaction in Layered Media," by Tzong, T.-J. and Penzien, J., October 1983, (PB84 192 178)A08.
- UCB/EERC-83/23 "Local Bond Stress-Slip Relationships of Deformed Bars under Generalized Excitations," by Eligehausen, R., Popov, E.P. and Bertero, V.V., October 1983, (PB84 192 848)A09.
- UCB/EERC-83/24 "Design Considerations for Shear Links in Eccentrically Braced Frames," by Malley, J.O. and Popov, E.P., November 1983, (PB84 192 186)A07.
- UCB/EERC-84/01 "Pseudodynamic Test Method for Seismic Performance Evaluation: Theory and Implementation," by Shing, P.-S.B. and Mahin, S.A., January 1984, (PB84 190 644)A08.
- UCB/EERC-84/02 "Dynamic Response Behavior of Kiang Hong Dian Dam," by Clough, R.W., Chang, K.-T., Chen, H.-Q. and Stephen, R.M., April 1984, (PB84 209 402)A08.
- UCB/EERC-84/03 "Refined Modelling of Reinforced Concrete Columns for Seismic Analysis," by Kaba, S.A. and Mahin, S.A., April 1984, (PB84 234 384)A06.
- UCB/EERC-84/04 "A New Floor Response Spectrum Method for Seismic Analysis of Multiply Supported Secondary Systems," by Asfura, A. and Der Kiureghian, A., June 1984, (PB84 239 417)A06.
- UCB/EERC-84/05 "Earthquake Simulation Tests and Associated Studies of a 1/5th-scale Model of a 7-Story R/C Frame-Wall Test Structure," by Bertero, V.V., Aktan, A.E., Charney, F.A. and Sause, R., June 1984, (PB84 239 409)A09.
- UCB/EERC-84/06 "R/C Structural Walls: Seismic Design for Shear," by Aktan, A.E. and Bertero, V.V., 1984.
- UCB/EERC-84/07 "Behavior of Interior and Exterior Flat-Plate Connections subjected to Inelastic Load Reversals," by Zee, H.L. and Moehle, J.P., August 1984, (PB86 117 629/AS)A07.
- UCB/EERC-84/08 "Experimental Study of the Seismic Behavior of a Two-Story Flat-Plate Structure," by Moehle, J.P. and Diebold, J.W., August 1984, (PB86 122 553/AS)A12.
- UCB/EERC-84/09 "Phenomenological Modeling of Steel Braces under Cyclic Loading," by Ikeda, K., Mahin, S.A. and Dermitzakis, S.N., May 1984, (PB86 132 198/AS)A08.
- UCB/EERC-84/10 "Earthquake Analysis and Response of Concrete Gravity Dams," by Fenves, G. and Chopra, A.K., August 1984, (PB85 193 902/AS)A11.
- UCB/EERC-84/11 "EAGD-84: A Computer Program for Earthquake Analysis of Concrete Gravity Dams," by Fenves, G. and Chopra, A.K., August 1984, (PB85 193 613/AS)A05.
- UCB/EERC-84/12 "A Refined Physical Theory Model for Predicting the Seismic Behavior of Braced Steel Frames," by Ikeda, K. and Mahin, S.A., July 1984, (PB85 191 450/AS)A09.
- UCB/EERC-84/13 "Earthquake Engineering Research at Berkeley - 1984," by , August 1984, (PB85 197 341/AS)A10.
- UCB/EERC-84/14 "Moduli and Damping Factors for Dynamic Analyses of Cohesionless Soils," by Seed, H.B., Wong, R.T., Idriss, I.M. and Tokimatsu, K., September 1984, (PB85 191 468/AS)A04.
- UCB/EERC-84/15 "The Influence of SPT Procedures in Soil Liquefaction Resistance Evaluations," by Seed, H.B., Tokimatsu, K., Harder, L.F. and Chung, R.M., October 1984, (PB85 191 732/AS)A04.
- UCB/EERC-84/16 "Simplified Procedures for the Evaluation of Settlements in Sands Due to Earthquake Shaking," by Tokimatsu, K. and Seed, H.B., October 1984, (PB85 197 887/AS)A03.
- UCB/EERC-84/17 "Evaluation of Energy Absorption Characteristics of Highway Bridges Under Seismic Conditions - Volume I (PB90 262 627)A16 and Volume II (Appendices) (PB90 262 635)A13," by Imbsen, R.A. and Penzien, J., September 1986.
- UCB/EERC-84/18 "Structure-Foundation Interactions under Dynamic Loads," by Liu, W.D. and Penzien, J., November 1984, (PB87 124 889/AS)A11.
- UCB/EERC-84/19 "Seismic Modelling of Deep Foundations," by Chen, C.-H. and Penzien, J., November 1984, (PB87 124 798/AS)A07.
- UCB/EERC-84/20 "Dynamic Response Behavior of Quan Shui Dam," by Clough, R.W., Chang, K.-T., Chen, H.-Q., Stephen, R.M., Ghanaat, Y. and Qi, J.-H., November 1984, (PB86 115177/AS)A07.
- UCB/EERC-85/01 "Simplified Methods of Analysis for Earthquake Resistant Design of Buildings," by Cruz, E.F. and Chopra, A.K., February 1985, (PB86 112299/AS)A12.
- UCB/EERC-85/02 "Estimation of Seismic Wave Coherency and Rupture Velocity using the SMART I Strong-Motion Array Recordings," by Abrahamson, N.A., March 1985, (PB86 214 343)A07.
- UCB/EERC-85/03 "Dynamic Properties of a Thirty Story Condominium Tower Building," by Stephen, R.M., Wilson, E.L. and Stander, N., April 1985, (PB86 118965/AS)A06.
- UCB/EERC-85/04 "Development of Substructuring Techniques for On-Line Computer Controlled Seismic Performance Testing," by Dermitzakis, S. and Mahin, S., February 1985, (PB86 132941/AS)A08.
- UCB/EERC-85/05 "A Simple Model for Reinforcing Bar Anchorages under Cyclic Excitations," by Filippou, F.C., March 1985, (PB86 112 919/AS)A05.
- UCB/EERC-85/06 "Racking Behavior of Wood-framed Gypsum Panels under Dynamic Load," by Oliva, M.G., June 1985, (PB90 262 643)A04.
- UCB/EERC-85/07 "Earthquake Analysis and Response of Concrete Arch Dams," by Fok, K.-L. and Chopra, A.K., June 1985, (PB86 139672/AS)A10.
- UCB/EERC-85/08 "Effect of Inelastic Behavior on the Analysis and Design of Earthquake Resistant Structures," by Lin, J.P. and Mahin, S.A., June 1985, (PB86 135340/AS)A08.
- UCB/EERC-85/09 "Earthquake Simulator Testing of a Base-Isolated Bridge Deck," by Kelly, J.M., Buckle, I.G. and Tsai, H.-C., January 1986, (PB87 124 152/AS)A06.

- UCB/EERC-85/10 "Simplified Analysis for Earthquake Resistant Design of Concrete Gravity Dams," by Fenves, G. and Chopra, A.K., June 1986, (PB87 124 160/AS)A08.
- UCB/EERC-85/11 "Dynamic Interaction Effects in Arch Dams," by Clough, R.W., Chang, K.-T., Chen, H.-Q. and Ghanaat, Y., October 1985, (PB86 135027/AS)A05.
- UCB/EERC-85/12 "Dynamic Response of Long Valley Dam in the Mammoth Lake Earthquake Series of May 25-27, 1980," by Lai, S. and Seed, H.B., November 1985, (PB86 142304/AS)A05.
- UCB/EERC-85/13 "A Methodology for Computer-Aided Design of Earthquake-Resistant Steel Structures," by Austin, M.A., Pister, K.S. and Mahin, S.A., December 1985, (PB86 159480/AS)A10.
- UCB/EERC-85/14 "Response of Tension-Leg Platforms to Vertical Seismic Excitations," by Liou, G.-S., Penzien, J. and Yeung, R.W., December 1985, (PB87 124 871/AS)A08.
- UCB/EERC-85/15 "Cyclic Loading Tests of Masonry Single Piers: Volume 4 - Additional Tests with Height to Width Ratio of 1," by Sveinsson, B., McNiven, H.D. and Sucuoglu, H., December 1985.
- UCB/EERC-85/16 "An Experimental Program for Studying the Dynamic Response of a Steel Frame with a Variety of Infill Partitions," by Yanev, B. and McNiven, H.D., December 1985, (PB90 262 676)A05.
- UCB/EERC-86/01 "A Study of Seismically Resistant Eccentrically Braced Steel Frame Systems," by Kasai, K. and Popov, E.P., January 1986, (PB87 124 178/AS)A14.
- UCB/EERC-86/02 "Design Problems in Soil Liquefaction," by Seed, H.B., February 1986, (PB87 124 186/AS)A03.
- UCB/EERC-86/03 "Implications of Recent Earthquakes and Research on Earthquake-Resistant Design and Construction of Buildings," by Bertero, V.V., March 1986, (PB87 124 194/AS)A05.
- UCB/EERC-86/04 "The Use of Load Dependent Vectors for Dynamic and Earthquake Analyses," by Leger, P., Wilson, E.L. and Clough, R.W., March 1986, (PB87 124 202/AS)A12.
- UCB/EERC-86/05 "Two Beam-To-Column Web Connections," by Tsai, K.-C. and Popov, E.P., April 1986, (PB87 124 301/AS)A04.
- UCB/EERC-86/06 "Determination of Penetration Resistance for Coarse-Grained Soils using the Becker Hammer Drill," by Harder, L.F. and Seed, H.B., May 1986, (PB87 124 210/AS)A07.
- UCB/EERC-86/07 "A Mathematical Model for Predicting the Nonlinear Response of Unreinforced Masonry Walls to In-Plane Earthquake Excitations," by Mengi, Y. and McNiven, H.D., May 1986, (PB87 124 780/AS)A06.
- UCB/EERC-86/08 "The 19 September 1985 Mexico Earthquake: Building Behavior," by Bertero, V.V., July 1986.
- UCB/EERC-86/09 "EACD-3D: A Computer Program for Three-Dimensional Earthquake Analysis of Concrete Dams," by Fok, K.-L., Hall, J.F. and Chopra, A.K., July 1986, (PB87 124 228/AS)A08.
- UCB/EERC-86/10 "Earthquake Simulation Tests and Associated Studies of a 0.3-Scale Model of a Six-Story Concentrically Braced Steel Structure," by Uang, C.-M. and Bertero, V.V., December 1986, (PB87 163 564/AS)A17.
- UCB/EERC-86/11 "Mechanical Characteristics of Base Isolation Bearings for a Bridge Deck Model Test," by Kelly, J.M., Buckle, I.G. and Koh, C.-G., November 1987, (PB90 262 668)A04.
- UCB/EERC-86/12 "Effects of Axial Load on Elastomeric Isolation Bearings," by Koh, C.-G. and Kelly, J.M., November 1987.
- UCB/EERC-87/01 "The FPS Earthquake Resisting System: Experimental Report," by Zayas, V.A., Low, S.S. and Mahin, S.A., June 1987.
- UCB/EERC-87/02 "Earthquake Simulator Tests and Associated Studies of a 0.3-Scale Model of a Six-Story Eccentrically Braced Steel Structure," by Whittaker, A., Uang, C.-M. and Bertero, V.V., July 1987.
- UCB/EERC-87/03 "A Displacement Control and Uplift Restraint Device for Base-Isolated Structures," by Kelly, J.M., Griffith, M.C. and Aiken, I.D., April 1987.
- UCB/EERC-87/04 "Earthquake Simulator Testing of a Combined Sliding Bearing and Rubber Bearing Isolation System," by Kelly, J.M. and Chalhoub, M.S., 1987.
- UCB/EERC-87/05 "Three-Dimensional Inelastic Analysis of Reinforced Concrete Frame-Wall Structures," by Moazzami, S. and Bertero, V.V., May 1987.
- UCB/EERC-87/06 "Experiments on Eccentrically Braced Frames with Composite Floors," by Ricles, J. and Popov, E., June 1987.
- UCB/EERC-87/07 "Dynamic Analysis of Seismically Resistant Eccentrically Braced Frames," by Ricles, J. and Popov, E., June 1987.
- UCB/EERC-87/08 "Undrained Cyclic Triaxial Testing of Gravels-The Effect of Membrane Compliance," by Evans, M.D. and Seed, H.B., July 1987.
- UCB/EERC-87/09 "Hybrid Solution Techniques for Generalized Pseudo-Dynamic Testing," by Thewalt, C. and Mahin, S.A., July 1987.
- UCB/EERC-87/10 "Ultimate Behavior of Butt Welded Splices in Heavy Rolled Steel Sections," by Bruneau, M., Mahin, S.A. and Popov, E.P., September 1987.
- UCB/EERC-87/11 "Residual Strength of Sand from Dam Failures in the Chilean Earthquake of March 3, 1985," by De Alba, P., Seed, H.B., Retamal, E. and Seed, R.B., September 1987.
- UCB/EERC-87/12 "Inelastic Seismic Response of Structures with Mass or Stiffness Eccentricities in Plan," by Bruneau, M. and Mahin, S.A., September 1987, (PB90 262 650)A14.
- UCB/EERC-87/13 "CSTRUCT: An Interactive Computer Environment for the Design and Analysis of Earthquake Resistant Steel Structures," by Austin, M.A., Mahin, S.A. and Pister, K.S., September 1987.
- UCB/EERC-87/14 "Experimental Study of Reinforced Concrete Columns Subjected to Multi-Axial Loading," by Low, S.S. and Moehle, J.P., September 1987.
- UCB/EERC-87/15 "Relationships between Soil Conditions and Earthquake Ground Motions in Mexico City in the Earthquake of Sept. 19, 1985," by Seed, H.B., Romo, M.P., Sun, J., Jaime, A. and Lysmer, J., October 1987.
- UCB/EERC-87/16 "Experimental Study of Seismic Response of R. C. Setback Buildings," by Shahrooz, B.M. and Moehle, J.P., October 1987.

- UCB/EERC-87/17 "The Effect of Slabs on the Flexural Behavior of Beams," by Pantazopoulou, S.J. and Moehle, J.P., October 1987, (PB90 262 700)A07.
- UCB/EERC-87/18 "Design Procedure for R-FBI Bearings," by Mostaghel, N. and Kelly, J.M., November 1987, (PB90 262 718)A04.
- UCB/EERC-87/19 "Analytical Models for Predicting the Lateral Response of R C Shear Walls: Evaluation of their Reliability," by Vulcano, A. and Bertero, V.V., November 1987.
- UCB/EERC-87/20 "Earthquake Response of Torsionally-Coupled Buildings," by Hejal, R. and Chopra, A.K., December 1987.
- UCB/EERC-87/21 "Dynamic Reservoir Interaction with Monticello Dam," by Clough, R.W., Ghanaat, Y. and Qiu, X-F., December 1987.
- UCB/EERC-87/22 "Strength Evaluation of Coarse-Grained Soils," by Siddiqi, F.H., Seed, R.B., Chan, C.K., Seed, H.B. and Pyke, R.M., December 1987.
- UCB/EERC-88/01 "Seismic Behavior of Concentrically Braced Steel Frames," by Khatib, I., Mahin, S.A. and Pister, K.S., January 1988.
- UCB/EERC-88/02 "Experimental Evaluation of Seismic Isolation of Medium-Rise Structures Subject to Uplift," by Griffith, M.C., Kelly, J.M., Coveney, V.A. and Koh, C.G., January 1988.
- UCB/EERC-88/03 "Cyclic Behavior of Steel Double Angle Connections," by Astaneh-Asl, A. and Nader, M.N., January 1988.
- UCB/EERC-88/04 "Re-evaluation of the Slide in the Lower San Fernando Dam in the Earthquake of Feb. 9, 1971," by Seed, H.B., Seed, R.B., Harder, L.F. and Jong, H.-L., April 1988.
- UCB/EERC-88/05 "Experimental Evaluation of Seismic Isolation of a Nine-Story Braced Steel Frame Subject to Uplift," by Griffith, M.C., Kelly, J.M. and Aiken, I.D., May 1988.
- UCB/EERC-88/06 "DRAIN-2DX User Guide," by Allahabadi, R. and Powell, G.H., March 1988.
- UCB/EERC-88/07 "Cylindrical Fluid Containers in Base-Isolated Structures," by Chalhoub, M.S. and Kelly, J.M., April 1988.
- UCB/EERC-88/08 "Analysis of Near-Source Waves: Separation of Wave Types using Strong Motion Array Recordings," by Darragh, R.B., June 1988.
- UCB/EERC-88/09 "Alternatives to Standard Mode Superposition for Analysis of Non-Classically Damped Systems," by Kusainov, A.A. and Clough, R.W., June 1988.
- UCB/EERC-88/10 "The Landslide at the Port of Nice on October 16, 1979," by Seed, H.B., Seed, R.B., Schlosser, F., Blondeau, F. and Juran, I., June 1988.
- UCB/EERC-88/11 "Liquefaction Potential of Sand Deposits Under Low Levels of Excitation," by Carter, D.P. and Seed, H.B., August 1988.
- UCB/EERC-88/12 "Nonlinear Analysis of Reinforced Concrete Frames Under Cyclic Load Reversals," by Filippou, F.C. and Issa, A., September 1988.
- UCB/EERC-88/13 "Implications of Recorded Earthquake Ground Motions on Seismic Design of Building Structures," by Uang, C.-M. and Bertero, V.V., November 1988.
- UCB/EERC-88/14 "An Experimental Study of the Behavior of Dual Steel Systems," by Whittaker, A.S., Uang, C.-M. and Bertero, V.V., September 1988.
- UCB/EERC-88/15 "Dynamic Moduli and Damping Ratios for Cohesive Soils," by Sun, J.I., Golesorkhi, R. and Seed, H.B., August 1988.
- UCB/EERC-88/16 "Reinforced Concrete Flat Plates Under Lateral Load: An Experimental Study Including Biaxial Effects," by Pan, A. and Moehle, J., October 1988.
- UCB/EERC-88/17 "Earthquake Engineering Research at Berkeley - 1988," by EERC, November 1988.
- UCB/EERC-88/18 "Use of Energy as a Design Criterion in Earthquake-Resistant Design," by Uang, C.-M. and Bertero, V.V., November 1988.
- UCB/EERC-88/19 "Steel Beam-Column Joints in Seismic Moment Resisting Frames," by Tsai, K.-C. and Popov, E.P., November 1988.
- UCB/EERC-88/20 "Base Isolation in Japan, 1988," by Kelly, J.M., December 1988.
- UCB/EERC-89/01 "Behavior of Long Links in Eccentrically Braced Frames," by Engelhardt, M.D. and Popov, E.P., January 1989.
- UCB/EERC-89/02 "Earthquake Simulator Testing of Steel Plate Added Damping and Stiffness Elements," by Whittaker, A., Bertero, V.V., Alonso, J. and Thompson, C., January 1989.
- UCB/EERC-89/03 "Implications of Site Effects in the Mexico City Earthquake of Sept. 19, 1985 for Earthquake-Resistant Design Criteria in the San Francisco Bay Area of California," by Seed, H.B. and Sun, J.I., March 1989.
- UCB/EERC-89/04 "Earthquake Analysis and Response of Intake-Outlet Towers," by Goyal, A. and Chopra, A.K., July 1989.
- UCB/EERC-89/05 "The 1985 Chile Earthquake: An Evaluation of Structural Requirements for Bearing Wall Buildings," by Wallace, J.W. and Moehle, J.P., July 1989.
- UCB/EERC-89/06 "Effects of Spatial Variation of Ground Motions on Large Multiply-Supported Structures," by Hao, H., July 1989.
- UCB/EERC-89/07 "EADAP - Enhanced Arch Dam Analysis Program: Users's Manual," by Ghanaat, Y. and Clough, R.W., August 1989.
- UCB/EERC-89/08 "Seismic Performance of Steel Moment Frames Plastically Designed by Least Squares Stress Fields," by Ohi, K. and Mahin, S.A., August 1989.
- UCB/EERC-89/09 "Feasibility and Performance Studies on Improving the Earthquake Resistance of New and Existing Buildings Using the Friction Pendulum System," by Zayas, V., Low, S., Mahin, S.A. and Bozzo, L., July 1989.
- UCB/EERC-89/10 "Measurement and Elimination of Membrane Compliance Effects in Undrained Triaxial Testing," by Nicholson, P.G., Seed, R.B. and Anwar, H., September 1989.
- UCB/EERC-89/11 "Static Tilt Behavior of Unanchored Cylindrical Tanks," by Lau, D.T. and Clough, R.W., September 1989.
- UCB/EERC-89/12 "ADAP-88: A Computer Program for Nonlinear Earthquake Analysis of Concrete Arch Dams," by Fenves, G.L., Mojtahedi, S. and Reimer, R.B., September 1989.
- UCB/EERC-89/13 "Mechanics of Low Shape Factor Elastomeric Seismic Isolation Bearings," by Aiken, I.D., Kelly, J.M. and Tajirian, F., December 1989.
- UCB/EERC-89/14 "Preliminary Report on the Seismological and Engineering Aspects of the October 17, 1989 Santa Cruz (Loma Prieta) Earthquake," by EERC, October 1989.
- UCB/EERC-89/15 "Experimental Studies of a Single Story Steel Structure Tested with Fixed, Semi-Rigid and Flexible Connections," by Nader, M.N. and Astaneh-Asl, A., August 1989.

- UCB/EERC-89/16 "Collapse of the Cypress Street Viaduct as a Result of the Loma Prieta Earthquake," by Nims, D.K., Miranda, E., Aiken, I.D., Whitaker, A.S. and Bertero, V.V., November 1989.
- UCB/EERC-90/01 "Mechanics of High-Shape Factor Elastomeric Seismic Isolation Bearings," by Kelly, J.M., Aiken, I.D. and Tajirian, F.F., March 1990.
- UCB/EERC-90/02 "Javid's Paradox: The Influence of Preform on the Modes of Vibrating Beams," by Kelly, J.M., Sackman, J.L. and Javid, A., May 1990.
- UCB/EERC-90/03 "Earthquake Simulator Testing and Analytical Studies of Two Energy-Absorbing Systems for Multistory Structures," by Aiken, I.D. and Kelly, J.M., October 1990.
- UCB/EERC-90/04 "Damage to the San Francisco-Oakland Bay Bridge During the October 17, 1989 Earthquake," by Astaneh, A., June 1990.
- UCB/EERC-90/05 "Preliminary Report on the Principal Geotechnical Aspects of the October 17, 1989 Loma Prieta Earthquake," by Seed, R.B., Dickenson, S.E., Riemer, M.F., Bray, J.D., Sitar, N., Mitchell, J.K., Idriss, I.M., Kayen, R.E., Kropp, A., Harder, L.F., Jr. and Power, M.S., April 1990.
- UCB/EERC-90/06 "Models of Critical Regions in Reinforced Concrete Frames Under Seismic Excitations," by Zulfiqar, N. and Filippou, F., May 1990.
- UCB/EERC-90/07 "A Unified Earthquake-Resistant Design Method for Steel Frames Using ARMA Models," by Takewaki, I., Conte, J.P., Mahin, S.A. and Pister, K.S., June 1990.
- UCB/EERC-90/08 "Soil Conditions and Earthquake Hazard Mitigation in the Marina District of San Francisco," by Mitchell, J.K., Masood, T., Kayen, R.E. and Seed, R.B., May 1990.
- UCB/EERC-90/09 "Influence of the Earthquake Ground Motion Process and Structural Properties on Response Characteristics of Simple Structures," by Conte, J.P., Pister, K.S. and Mahin, S.A., July 1990.
- UCB/EERC-90/10 "Experimental Testing of the Resilient-Friction Base Isolation System," by Clark, P.W. and Kelly, J.M., July 1990.
- UCB/EERC-90/11 "Seismic Hazard Analysis: Improved Models, Uncertainties and Sensitivities," by Araya, R. and Der Kiureghian, A., March 1988.
- UCB/EERC-90/12 "Effects of Torsion on the Linear and Nonlinear Seismic Response of Structures," by Sedarat, H. and Bertero, V.V., September 1989.
- UCB/EERC-90/13 "The Effects of Tectonic Movements on Stresses and Deformations in Earth Embankments," by Bray, J. D., Seed, R. B. and Seed, H. B., September 1989.
- UCB/EERC-90/14 "Inelastic Seismic Response of One-Story, Asymmetric-Plan Systems," by Goel, R.K. and Chopra, A.K., October 1990.
- UCB/EERC-90/15 "Dynamic Crack Propagation: A Model for Near-Field Ground Motion," by Seyyedian, H. and Kelly, J.M., 1990.
- UCB/EERC-90/16 "Sensitivity of Long-Period Response Spectra to System Initial Conditions," by Blasquez, R., Ventura, C. and Kelly, J.M., 1990.
- UCB/EERC-90/17 "Behavior of Peak Values and Spectral Ordinates of Near-Source Strong Ground-Motion over a Dense Array," by Niazi, M., June 1990.
- UCB/EERC-90/18 "Material Characterization of Elastomers used in Earthquake Base Isolation," by Papoulia, K.D. and Kelly, J.M., 1990.
- UCB/EERC-90/19 "Cyclic Behavior of Steel Top-and-Bottom Plate Moment Connections," by Harriott, J.D. and Astaneh, A., August 1990.
- UCB/EERC-90/20 "Seismic Response Evaluation of an Instrumented Six Story Steel Building," by Shen, J.-H. and Astaneh, A., December 1990.
- UCB/EERC-90/21 "Observations and Implications of Tests on the Cypress Street Viaduct Test Structure," by Mahin, S.A., Moehle, J.P., Stephen, R.M., Bollo, M. and Qi, X., December 1990.
- UCB/EERC-91/01 "Experimental Evaluation of Nitinol for Energy Dissipation in Structures," by Nims, D.K., Sasaki, K.K. and Kelly, J.M., 1991.
- UCB/EERC-91/02 "Displacement Design Approach for Reinforced Concrete Structures Subjected to Earthquakes," by Qi, X. and Moehle, J.P., January 1991.
- UCB/EERC-91/03 "Shake Table Tests of Long Period Isolation System for Nuclear Facilities at Soft Soil Sites," by Kelly, J.M., March 1991.
- UCB/EERC-91/04 "Dynamic and Failure Characteristics of Bridgestone Isolation Bearings," by Kelly, J.M., April 1991.
- UCB/EERC-91/05 "Base Sliding Response of Concrete Gravity Dams to Earthquakes," by Chopra, A.K. and Zhang, L., May 1991.
- UCB/EERC-91/06 "Computation of Spatially Varying Ground Motion and Foundation-Rock Impedance Matrices for Seismic Analysis of Arch Dams," by Zhang, L. and Chopra, A.K., May 1991.